UNIVERSITÉ DE MONTRÉAL

GAS-PHASE CARBON COATING OF $LiFePO_4$ NANO PARTICLES AS A CATHODE BUILDING BLOCK FOR Li-ION BATTERIES

SAMIRA AGHAEE SARBARZE

DÉPARTEMENT DE GÉNIE CHIMIQUE

ÉCOLE POLYTECHNIQUE DE MONTRÉAL

MÉMOIRE PRÉSENTÉ EN VUE DE L'OBTENTION

DU DIPLÔME DE MAÎTRISE ÈS SCIENCES APPLIQUÉES

(GÉNIE CHIMIQUE)

AOÛT 2017

UNIVERSITÉ DE MONTRÉAL

ÉCOLE POLYTECHNIQUE DE MONTRÉAL

Ce mémoire intitulé:

GAS-PHASE CARBON COATING OF $LiFePO_4$ NANO PARTICLES AS A CATHODE BUILDING BLOCK FOR Li-ION BATTERIES

présenté par : AGHAEE SARBARZE Samira

en vue de l'obtention du diplôme de : Maîtrise ès sciences appliquées

a été dûment accepté par le jury d'examen constitué de:

M. PERRIER Michel, Ph. D., président

M. CHAOUKI Jamal, Ph. D., membre et directeur de recherche

Mme BOFFITO Daria Camilla, Ph. D., membre

DEDICATION

To my lovely parents, my siblings,

my beloved Mohammad and the light of my eyes, AmirAli

ACKNOWLEDGEMENTS

First and foremost, I am thankful to almighty God without whom nothing is possible.

I would like to thank my honourable academic advisor, Professor Jamal Chaouki for accepting me into his group, his excellent guidance and patience, and giving me the opportunity to experience research in an amazing atmosphere.

The financial support provided by Johnson Matthey, the industrial partner of this research and the Natural Sciences and Engineering Research Council of Canada (NSERC) are greatly appreciated.

I would like to express my deepest appreciation to my colleagues, Dr. Mohammad Latifi, Dr. Pierre Sauriol and Dr. Majid Rasouli, for all their supports, insightful comments and feedbacks in every steps of my work. I have greatly benefited from working with such knowledgeable people.

Special thanks to the technicians in the Department of Chemical Engineering, especially, Mr. Robert Denisle, Mr. Sylvain Simard-fleury and Mr. Gino Robin for their excellent technical assistance.

I am also thankful to Department of Chemical engineering of Ecole Polytechnique de Montreal as well as Ms. Evelyne Roussau, Ms. Carmen Elena Membreno Aguilar, Ms. Valerie Baudart and Ms. Helen Chatillion for their kind administration services during my study.

A special gratitude goes to members of process engineering advanced research lab (PEARL), particularly, my friend and officemate El Mahdi Lakhdissi for translating the abstract to French.

Many thanks to Dr. Steeve Rassolt, Dr. Majid Talebi, and Dr. Patrice Chartrand. My research wouldn't have been possible without their helps.

Lastly, I wish to thank my family for all their supports and constant love. I owe my profound gratitude to my lovely parents and my siblings, who are my sole mates, for providing me with unfailing supports and their encouragements during my whole life. Special thanks to my mom who took care of my dearest son for every hour I spent for writing. Above all, my loving, supportive, encouraging and patient husband, Mohammad whose wise counsel and supports during years of research are greatly appreciated. Thanks to my all, AmirAli, who has given me much happiness and keeps me being hopeful. To them, I dedicate this thesis.

Samira

RÉSUMÉ

Les véhicules électriques représentent une solution envisagée dans le secteur des transports pour atténuer les défis relatifs au réchauffement climatique et qui relèvent principalement des émissions du dioxyde de carbone vers l'atmosphère. Les batteries aux ions lithium constituent la partie la plus importante des véhicules électriques et ainsi elles contrôlent le prix ultime de ce genre de véhicules. Par conséquent, il est crucial de développer les batteries les plus légères possibles et qui ont la performance électrochimique la plus proéminente.

Le coût majeur des batteries aux ions lithium revient à leur électrode cathodique. Les poudres de phosphate de fer lithié (PFL) constituent le matériau composant le plus prometteur de l'électrode cathodique de ces batteries. Les PFL ont reçu l'intérêt du secteur industriel ainsi qu'académique vu leurs avantages clés comme la stabilité thermique, le respect de l'environnement, la sécurité et relativement le coût économique.

Or, hormis tous ces avantages, les PFL sont confrontés aux limitations de la faible conductivité et la faible diffusivité ionique. La fabrication des particules à petit diamètre et l'application d'une couche de revêtement appropriée comme le graphite de carbone sur la surface des PFL permettent fréquemment de contrecarrer ces limitations. Le revêtement offre aussi un cycle de vie plus long pour les batteries rechargeables. Toutefois, les procédés conventionnels de revêtement en carbone utilisent soit un liquide comme le sucre dissout soit un solide comme un copolymère ou un précurseur de carbone ce qui fait surgir des problèmes comme le coût élevé, un excès de carbone (poids mort), une couche non uniforme et des types indésirables des revêtements en carbone.

Tirant profit de la diffusivité beaucoup plus élevée du précurseur de carbone gazeux sur la surface des poudres de PFL, nous avons développé un procédé de revêtement en carbone en phase gazeuse qui comprend un réacteur à lit fluidisé pour le dépôt chimique en phase vapeur (FB-CVD) pour déposer une couche mince de carbone à températures élevées inférieures à la température de frittage à savoir 750 °C sur des poudres PFL de taille nano qui ont été synthétisées par la méthode hydrothermique.

A cause de la présence sévère des forces inter particulaires, les nanoparticules PFL tel que reçues avec une distribution de taille primaire de 50 à 400 nm ont été agglomérées et donc ils ont eu une distribution de taille secondaire de de 5 à 850 μm. L'effet des conditions opératoires telles que le

type et la concentration du précurseur de carbone, la température, le temps de réaction, le temps de séjour du gaz, la distribution de tailles des poudres PFL secondaires sur la qualité du carbone déposé en terme de l'épaisseur du revêtement, du type de carbone et de la performance électrochimique des poudres C-PFL produites a été optimisé dans ce travail de recherche.

Parmi plusieurs candidats pour le précurseur, le propylène a été considéré comme le plus approprié. Un réacteur à lit fluidisé utilisant le chauffage par induction et fabriqué à l'échelle laboratoire a été modifié et adapté pour effectuer les tests du FB-CVD et une procédure opératoire standard a été développée. Les poudres PFL revêtues ont été caractérisées par les analyses XRD, SEM, TEM, XPS, la spectroscopie Raman, la mesure de conductivité, LECO et l'analyse électrochimique.

Les premières séries d'investigation concernaient la production de C-PFL à partir des poudres PFL secondaires avec une distribution des tailles de 125 à 250 μm et représentant poudres du groupe de Geldart A et ceci dans l'équipement FB-CVD développé afin d'examiner scientifiquement la faisabilité du procédé du revêtement en carbone en phase gazeuse quant à savoir ou pas si le carbone a été déposé uniformément sur la surface des poudres PFL dans un réacteur à lit fluidisé et de sorte que les propriétés électrochimiques soient supérieurement améliorées. Les résultats ont montré que le carbone a été avec succès déposé uniformément sur la surface des poudres PFL à des conditions opératoires optimales de sorte que le carbone de graphite constitue à peu près le double du carbone de type diamant et la capacité de décharge des PFL a été significativement élevée de 40 à 130 mA.h/g.

Suite aux résultats prometteurs des poudres PFL du groupe Geldart **A** , le travail de recherche a mis l'accent sur l'application du procédé de FB-CVD optimal pour les poudres PFL secondaires très cohésives de taille inférieure à 90 μm. L'originalité de ce travail de recherche se résume dans le développement d'un réacteur FB-CVD assisté par impulsions en utilisant une électrovanne à l'entrée du réacteur avec fonctionnement intermittent pour surpasser les forces inter particulaires et par conséquent fluidiser tout le lit des PFL. Par la suite, des poudres C-LFP avec un carbone revêtu beaucoup plus uniforme comparé aux poudres PFL qui sont plus grandes de taille ont été obtenus et la capacité de décharge de plus de 140 mA.h/g a été atteinte.

L'analyse XPS a révélé qu'une liaison très forte a été formée entre le carbone déposé et le phosphate de PFL. Les analogies entre les échantillons C-PFL dérivées des procédés basés sur le

FB-CVD et le FB-CVD assisté par impulsions révèlent que le PFL avec une distribution de tailles plus petite possède une électro-conductivité supérieure et une meilleure performance comme matériel cathodique d'une cellule de batterie.

ABSTRACT

Electric vehicles are through to be a solution in transportation sector to mitigate the global warming challenges due to release of carbon dioxide to the atmosphere. Lithium ion batteries constitute the most important part of electric vehicles, and consequently govern the ultimate price of such vehicles. Therefore, it is crucial to develop batteries with the lightest possible weight and the most prominent electrochemical performance.

Major cost of the lithium ion batteries belongs to their cathode electrode. Lithium iron phosphate (LFP) powders are one of the promising building block materials of the cathode electrode of such batteries. LFP has received a lot of interest in research from both academia and industry due to its key advantages such as thermal stability, environmental friendly, safety and relatively economical cost.

Despite all these advantages, LFP suffers from low electrical conductivity and low ion diffusivity. Achieving small size particles and applying an appropriate conductive-coated layer, such as graphite carbon, on the surface of LFP powders commonly address these limitations. The coating also affords longer cycle life to the rechargeable batteries. However, conventional LFP carbon coating processes include either a liquid, e.g. dissolved sugar, or a solid, e.g. co-polymer, carbon precursor where it has been led to issues such as high cost, excess carbon (dead weight), non uniform layer and undesired type of the coated carbon.

Taking advantage of enhanced diffusivity of a gaseous carbon precursor onto surface of LFP powders, we developed a gas-phase carbon coating process that includes a fluidized bed chemical vapor deposition reactor (FB-CVD) to deposit a thin layer of carbon at elevated temperatures below sintering temperature, namely 750 °C, of nano size LFP powders that were synthesized by a hydrothermal method.

Due to severe presence of interparticle forces, the as-received LFP nanoparticles with a primary size distribution of 50 to 400 nm were agglomerated, so they had a secondary size distribution from 5 to 850 μm. Effect of operating conditions such as type and concentration of the gaseous carbon precursor, temperature, reaction time, gas residence time, and size distribution of LFP secondary powders on quality of deposited carbon, in terms of coating thickness and type of

carbon, as well as electrochemical performance of the produced C-LFP powders were optimized in this research.

Among several candidate precursors, propylene was selected as the most suitable one. A bench-scale induction heating fluidized bed reactor was modified and commissioned to run the FB-CVD tests, and a standard operating procedure was developed. The coated LFP powders were characterized by XRD, SEM, TEM, XPS, Raman spectroscopy, conductivity-meter, LECO and electrochemical analyses.

First series of investigation was about C-LFP production from secondary LFP powders with a size distribution of 125 to 250 μm, representing Geldart's group A powders, in the developed FB-CVD setup to scientifically investigate feasibility of the gas-phase carbon coating process as to where or not carbon can be deposited uniformly on the surface of LFP powders in a fluidized be reactor so that electrochemical properties of LFP are superiorly enhanced. Results revealed that carbon successfully deposited uniformly onto surface of LFP powders at optimum operating conditions so that graphite carbon was almost twice the diamond carbon, and discharge capacity of LFP significantly improved from 40 to about 130 mA.h/g.

Following the very promising results from the Geldart's group A LFP powders, the research focused on applying the optimum FB-CVD process to the very cohesive secondary LFP powders with a size less than 90 μm. As a novelty of this research, we developed a pulse-assisted FB-CVD setup, employing a solenoid valve in the reactor inlet with an intermittent operation, to overcome interparticle forces, and consequently, to fluidize the whole LFP bed. Subsequently, C-LFP powders with much more uniform coated carbon, as opposed to the coarser secondary LFP powders, were obtained and the discharged capacity of more than 140 mA.h/g was obtained.

XPS analysis revealed that a strong bond was formed between the deposited carbon and the phosphate of LFP. Analogies between the C-LFP samples derived from FB-CVD and pulse-assisted FB-CVD processes revealed that LFP with smaller secondary particle size possesses higher electro-conductivity and better performance as a cathode material in a battery cell.

TABLE OF CONTENTS

LIST OF TABLES

LIST OF FIGURES

LIST OF APPENDICES

CHAPTER 1 INTRODUCTION

Human beings have been employing various resources of energy looking for ways to facilitate their life with the fastest phenomena, with the lowest cost and the highest performance. Discovery of fossil fuels such as coal and petroleum helped significantly supply the world growing energy demand upon rapid growth of the global population. Technology development and production of various tools and machines are some areas where fossil fuels are primary resources of energy. Particularly, the automobile industry has produced the internal combustion engine (ICE) cars that run only on either gasoline or diesel.

On the other hand, abundance of fossil fuel resources is limited, and their utilization is costly due to several necessary extraction and refining steps to be taken until a final fuel with a desired grade is obtained. In addition, there are serious environmental problems and health issues associated with the emissions resulted from combustion of fossil fuels. For instance, given presence of sulfur in a fossil fuel and its combustion reaction with air, release of gases such as SO_2, SO_3, NO and NO_2 leads in formation of acidic rains as a result of contact with humidity. Concentration of these emissions is usually larger than the permitted limits. As an example, concentration of SO_2 and NO_2 from coal combustors before gas cleaning is 200-2000 ppm and 800 ppm, respectively[1].

In some countries, there are legislations to control concentration of emissions and to keep it below the standard levels. For example, according to the National Ambient Air Quality Standards (NAAQS) set by the Environmental Protection Agency (EPA) in the US, concentration of the released SO_2 and NO_2 must be below 100 ppb and 75 ppb, respectively.

Combustion of fossil fuels in the ICE cars also contributes significantly to the global warming because of large mass of CO_2 emission.

Many solutions have been considered to reduce/eliminate the emissions and to meet environmental regulations. A solution is placement of catalytic converter in the gas outlet pipe of cars where, for instance, CO_2 is converted to CO. Another solution is combustion of hydrogen where the only product gas is vapor.

Generation of electricity from sustainable energy resources in order for electricity propulsion being employed by namely electric vehicles (EV) is another top solution to minimize the emissions. The electrical cars benefit from having batteries where electricity is generated in the absence of any combustion reaction as well as environmental contaminants. Another advantage of the electric cars is less consumption of fossil fuels in transportation section and securing their supply for other sections.

Intensive research and development as well as engineering efforts have been carried out to move forward from the ICE cars towards partially electric propulsion cars, i.e. hybrid electric vehicles (HEV) and plugged-in hybrid electric vehicles (PHEV), and finally fully electric vehicles (EV). Internal combustion engine is the main propulsion source of the HEV cars while their battery is the alternative energy source for short driving ranges.

Lead-acid batteries are the first generation of rechargeable batteries that were used in the ICE cars to ignite the engine. Nickel-cadmium (Ni-Cd) batteries with greater energy density is one of the earliest rechargeable batteries with alkali electrolyte that were initially employed in 1899. However, heavy and bulky Ni-Cd batteries suffered from their memory effect. Also, cadmium is an environmental hazard and highly toxic metal that limited their applications. Ni-Cd batteries were replaced by Ni-MH (Nickel-metal hydride) batteries due to their advantages of high rate, excellent safety and long cycle life.

Electric vehicles (EV) and plugged-in electric vehicles (PIEV), which require only electric power to produce propulsion, are certainly excellent candidates to replace ICE cars to reduce or cut oil dependency, urban air pollution and climate change challenges. They, however, cannot employ Ni-MH batteries due to low energy density of such batteries and their sensitivity to overcharging.

In 1980, Professor John Goodenough introduced a new generation of rechargeable batteries based on lithium ion migration through the battery cell, named Li-ion batteries (LIBs)[2]. Lithium as the lightest metal of the periodic table has a high electrochemical potential. Therefore, it can provide a large voltage in a small volume. In comparison with Ni-Cd and Ni-MH batteries, for a given voltage, LIBs are more compact, i.e. smaller size

and lighter weight. A comparative trend of rechargeable batteries development is presented in Figure 1.1.

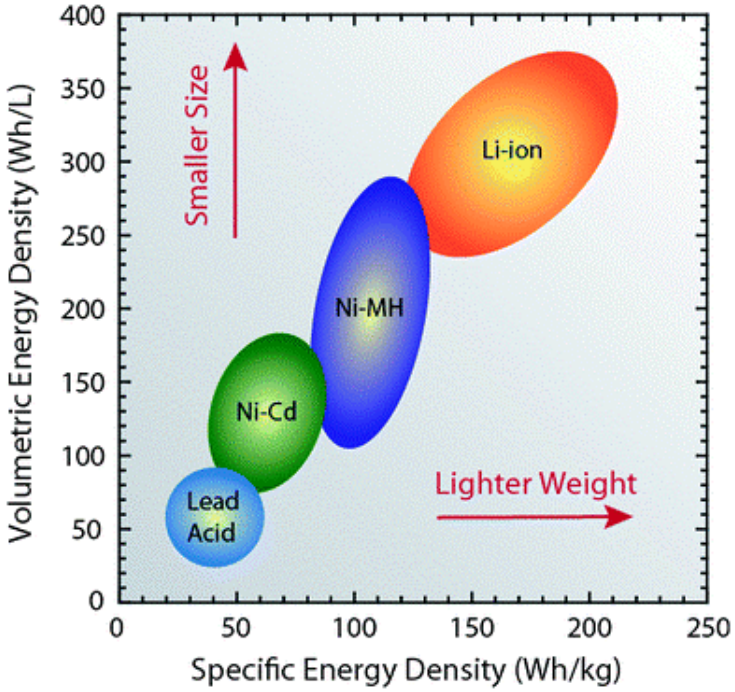

Figure 1.1: Changing in energy density with developments in cell technology [3]

Currently LIBs are widely used in portable electronics, power tools and smart grid storages. Also, due to the high energy and power density as well as long cycle life, LIBs have attracted a keen attention of automotive industry to employ them in electric vehicles. In other words, LIBs have been the main batteries of HEVs, PIEVs and EVs because such cars require batteries with high energy and power density as well as high capability rate unless otherwise they cannot compete with ICE vehicles.

Despite promising features of LIBs, they suffer from being relatively expensive, having weak electric and ion conductivity as well as having some safety concerns[4]. As a result, for instance, current electric cars in the market employ relatively large and heavy batteries so that they require quite frequent charging per 100 km trip. Therefore, substantial improvements must be applied on the building block material of such batteries, i.e. cathode and anode electrodes, to yield high enough electric conductivity and ion diffusivity of lithium ions during charge and discharge operations.

Cathode electrode is the most expensive component of the battery because it is the source of ions. With respect to this motivation, the presented work addresses improvement of both electric and ion conductivity properties of cathode material of LIBs.

1.1 Constituents of a battery

Typically, the main parts of a LIB comprise a cathode (with higher electrochemical potential), an anode (with lower electrochemical potential) and an electrolyte. Electrodes of the batteries consist of active particles, binder and conductive additives coated on the current collectors plus some other components to fabricate a battery cell. Figure 1.2 is a schematic of all the constituent of a LIB cell.

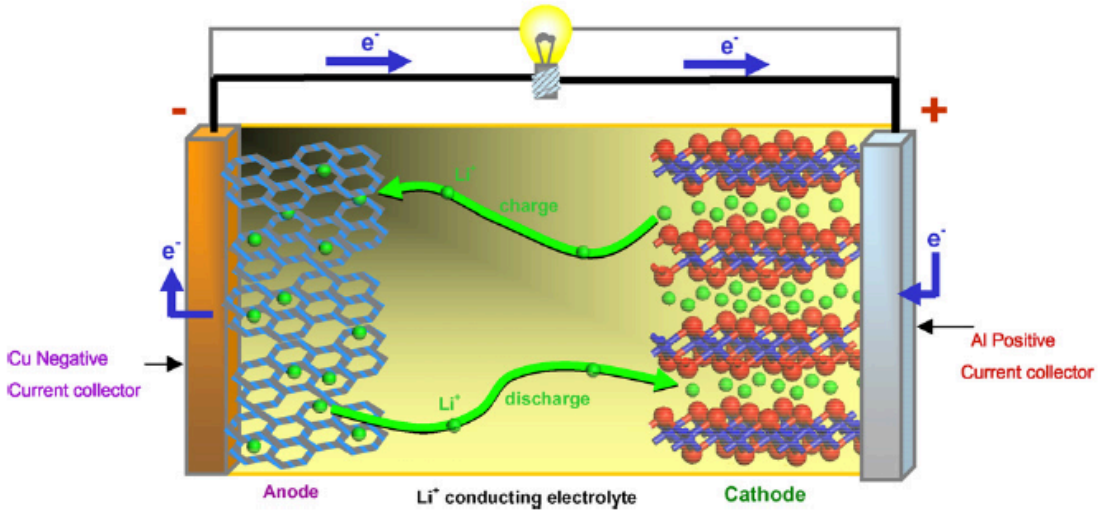

Figure 1.2: Typical Li-ion battery cell[3]

The Charge/discharge mechanism of the LIBs is based on the Li^+ ions transportation from the electrodes through the electrolyte. During a discharge, electrons release from the positive electrode, i.e. cathode, through the outer circuit and reach the negative electrode, i.e. anode. Li^+ ions also travel through the electrolyte from cathode towards the anode during the discharge. Li^+ ions and electrons combine at the anode and make Li^0 metals. A charge operation is about movement of electrons and Li^+ in the opposition direction, i.e. from anode to cathode. Charging and discharging processes are presented Figure 1.3.

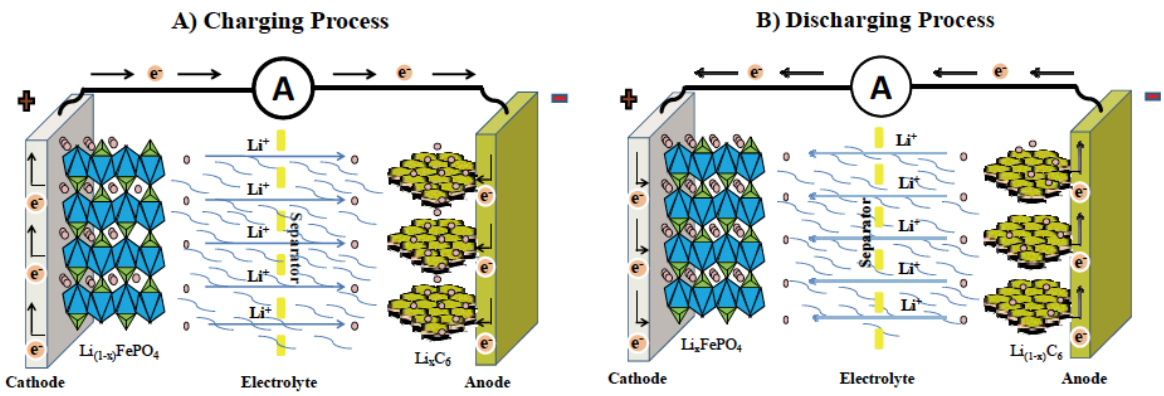

Figure 1.3: Charging/Discharging process in a cell [5]

A variety of materials may be used in fabrication of each single parts of a cell. Carbon-based materials in a variety of consistencies are widely used as the anode building material of LIBs[6]. Graphite due to its low cost, ease of availability and good intercalation/de-intercalation reversibility is the most common material of the negative electrode. Intercalation of lithium ions to form LiC_6 occurs based on Reaction 1-1:

$$\boldsymbol{C_6 + Li^+ + e^- \leftrightarrow LiC_6} \qquad \text{Reaction 1-1}$$

In some cases, lithium titanate oxide (LTO) is used as the anode material due to the safety, durability and improvement of battery performance during fast charging[6]. However, it has a very low capacity. There are some other materials such as transition metal sulfides, nitrides and phosphides that could be considered as the anode building material; however, high volume expansion, poor electron transport and capacity fading limit their application.[7]

Selection of a proper electrolyste is another key factor in a battery cell. Ethylene carbonate-dimethyl carbonate (EC-DMC) and $LiFP_6$ are the most preferred solutions being employed as the electrolyte due to the high ionic conductivity even at temperature down to -15°C. EC-DMC has the highest anodic stability due to the carbonate group existed in the molecule structure.

In the case of cathode material, so many researches have been performed to derive the best option of material that meets all the necessities of a battery application in electric vehicles.

1.2 Cathode materials of Li-ion batteries

Type and properties of the cathode building materials significantly influence performance of a battery. The cathode material of a LIB is the source of the lithium ions so that its rate performance is the bottleneck in development of the battery. Rate capability is determined by the kinetics of charge-discharge reactions. During charge/discharge cycles, lithium ions must be able to intercalate and then release from the cathode structure repeatedly and rapidly to provide recharging and high currency, respectively.

Cost is one of the most important concerns to do with synthesizing a large mass of the batteries building materials. Majority of the total cost of a battery is related to the cathode material, hence it is important to develop an optimized process to fabricate a suitable cathode material for large-scale industrial applications.

Therefore, an ideal cathode material has to possess the following important properties[8]:

- It should contain reducible/oxidizable ions similar to function of a transition metal;
- The material should react with Li rapidly with a high free energy of the reaction and in a reversible manner; this leads to a high power density, capacity, voltage and energy storage;
- The material has to be a good electronic conductor which facilitate electron transportation through the electrode, addition and removal from the electrode and allows for reaction at all contact points of electrolyte with cathode particle's surface;
- The material should be stable so that, particularly, its structure does not change and get degraded;
- Low cost and being environmentally friendly are two critical parameters for a mass production scale.

1.2.1 Various types of cathode material

Based on the above-mentioned required properties, several materials have shown potential characteristics for a promising cathode material. Generally, studies on the LIBs cathode materials are focused on three main classes of material based on their crystal structure as depicted in Figure 1.4.

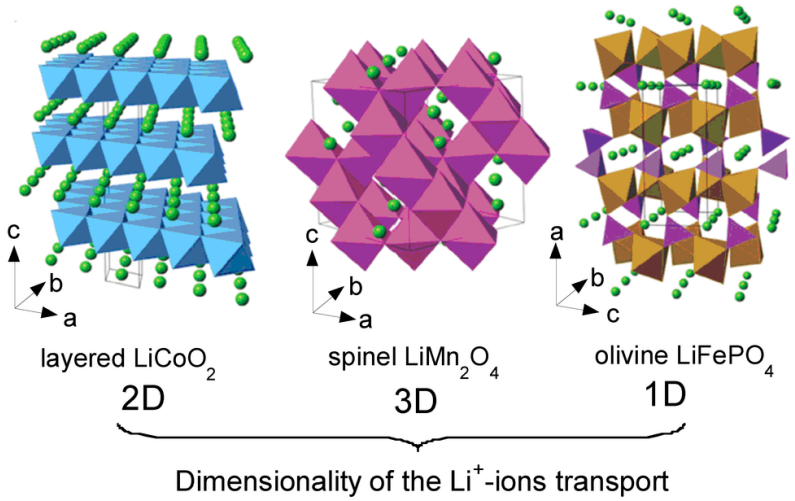

Figure 1.4: Crystal structures of different types of cathode materials [9]

The first group consists of transition metal oxides like $LiCoO_2$ (LCO). They have layered compact lattice structure, which provide high-energy storage per unit volume[10, 11]. $LiNiO_4$ and LiV_3O_8 are the other examples of such materials that belong to this group. Currently, $LiCoO_2$ is used as the cathode material of the LIBs in portable applications like laptops, cellphones and cameras, but this material doesn't meet the requirements for the large applications such as EVs due to its high cost and safety concerns. LCO has the lowest thermal stability of the cathode materials. If the temperature of the battery cell reaches to a certain point, oxygen from the structure of LCO released by an exothermic reaction, which can makes flame in the battery[10].

The second group belongs to materials with spinel structure like $LiMn_2O_4$, which has lower cost and is safer than LCO but has lower capacity. Phase changing is probable during cycling due to the loss of oxygen in charging phase. Moreover, if the battery is

stored untouched for a while, a capacity loss may occur due to either dissolution of Mn in electrolyte or change of the morphology and crystallinity of the material [8, 9].

The third group belongs to polyanion-based olivines such as $LiFePO_4$ that has potential of lower price than the previous groups[12]. Polyanions are a group of material with a large $(XO_4)_3$- group, where X can be S, P, Si, Mo or W, that occupies the lattice position and increases cathode redox potential and also helps stabilize the materials structure. Among this group, olivine phosphates are the most popular one with the orthorhombic Pnma structure. $LiMnPO_4$ (LMP), $LiCoPO_4$ (LCP) and $LiFePO_4$ (LFP) are some examples of such a material. $Li_3V_2(PO_4)_3$ is another cathode material that has monoclinic structure and it has high operating voltage and high rate capability[12]. In comparison with LFP, LMP and LCP have higher circuit voltage of 4.1 and 4.6V, respectively. However, they have lower capacity about 1/3 and 1/6 of LFP[11]. In addition, $Mn_2P_4O_7$ and $Co_2P_4O_7$ have been observed in the delithiated form of LMP and LCP, which degrade the lifetime of the cell. Also, due to the oxygen evolving in the decomposition reaction, they have safety concerns. Table 1.1 summarizes the comparisons between these three groups.

As it could be observed in Figure 1.4 lithium ions intercalate/de-intercalate in 2 and 3 dimensions in layered and spinel structure, respectively. Unlikely, LFP has olivine orthorhombic structure in which phosphate occupies tetrahedral, lithium and iron metals occupy octahedral in 4c and 4a sites. As a result, olivine delithiate in one dimension. Thus, LFP introduced in 1990s [4, 12-14], demonstrates naturally a very low performance. However, in recent years, LFP has attracted a lot of attention of research and industry due to its high theoretical capacity (170 $mAhg^{-1}$), stable voltage plateau of 3.5 vs. Li/Li^+, good thermal stability at both low and high temperature, excellent cycle performance, stable structure during charging/discharging, high safety, abundant raw material with low cost and environmentally friendly synthesis processing.

This work focuses on development of a gas phase chemical vapor deposition method as a secondary step to improve conductive properties of the primary synthesized LFP by proper deposition of a layer of carbon on the surface of LFP.

Table 1.1: Prospective cathode materials based on the structure

Group	Material	Advantages	Disadvantages
Layered oxide	$LiCoO_2$	High energy density	High cost Safety concerns
	LiV_3O_8	High energy density	High cost Safety concerns
	$LiNiO_2$	High capacity Low cost, High energy density	Low voltage Less stable and Less ordered
Spinel	$LiMn_2O_4$	Low cost Safer than layered oxide group	Low capacity
Olivine	$LiFePO_4$	High stability, low cost, high capacity	Poor intrinsic transport properties
	$Li_3V_2(PO_4)_3$	High operating voltage and high capability	Safety concern Low capacity
	$LiCoPO_4$ $LiMnPO_4$	High open circuit voltage	

1.3 LFP synthesis methods

A $LiFePO_4$ synthesis method influences structure and performance of the material[5]. There are three main fabrication routes to synthesis LFP: Solid-states, solution and melt casting base. [5]

1.3.1 Solid-state:

The most common and traditional method to prepare LFP is high temperature solid-state. i.e. solid-solid reaction, which requires an inert or reductive atmosphere to prevent oxidization of iron(II). Normally this method consists of several steps of mixing raw materials, ball-milling, particles dispersing (e.g. by ball-milling) and sintering at high temperature. The main lithium precursors are LiF, Li_2CO_3, $LiOH.2H_2O$ and CH_3COOLi. $FeC_2O_4.2H_2O$, $FePO_4(H_2O)_2$ and $Fe(CH_3COO)_2$ are iron precursors and $NH_4H_2PO_4$ is a phosphorus precursor [15-17].

In this method, sintering temperature plays an important role in the properties of final LFP material in terms of not only formation of impurities, but most importantly of the material capacity and its electrochemical performance. Electrochemical properties vary with the raw materials that are used for LFP synthesis. Although it is an easy and simple method of LFP synthesis, impurities are detected in the final material, particle sizes are large and also the process consist of several steps, including grinding and calcination at high temperatures, causing it to be lengthy and time consuming. Another disadvantage of this method is small surface area caused by uncontrollable particle growth and agglomeration which is not desired for the ionic conductivity.

The are three categories of the solid-state method:

- *Mechanochemical activation*: during mechanical activation, particles undergo welding, fracturing and re-welding in a dry high-energy ball-milling vessel. The intimate mixing results in pulverized particles and a new phase of solid-state reaction [18].
- *Carbothermal reduction*: Glucose or carbon black as a reducing agent is mixed with the precursors. Then the mixture is grinded by ball milling with ethyl alcohol as the

liquid medium. Subsequently drying with air is applied at 80 °C to evaporate ethyl alcohol followed by heating under a flow of argon in a furnace at elevated temperature (about 700°C)[19].

- *Microwave heating*: precursors are prepared by solid-state mixing and then calcined in microwave under inert atmosphere. Iron source acts as the microwave susceptor which is the limitation of this method. However, since the reaction occurs after adding iron metal, carbon is a suitable alternative to act as both microwave absorber and a source of reducing reagent in order to inhibit iron oxidation [20-22]. Compared to other solid-state methods, microwave technology is the most facile and economic one which can be expected to shorten the reaction time to a few minutes with significant energy savings. However, this process has a poor reproducibility.

1.3.2 Solution based method

Hydrothermal, sol-gel, ultrasonic spray drying and co-precipitation are three solution methods for LFP synthesis.

Hydrothermal: it is a useful method for preparation of fine particles among the various synthesis methods that offers high performance LFP. There are some other advantages such as simple synthesis and energy-efficient process. Also, it is quick and easy to operate [18, 23-30]. However, it is difficult to accurately control the chemical compositions of the as-prepared materials.

Sol-gel: Sol is defined as the dispersion of colloidal particles in liquid. Gel is the interconnected-rigid network with pores of sub micrometer dimensions and polymeric chains. In this method, precursors are dissolved in ethanol and then get mixed with an acid such as citric acid [31], lauric acid [32] and adipic acid[25] as both chelating agent and carbon precursor. Then the solution is heated to evaporate ethanol. The resulting material is a transparent sol. After that, sol is dried at vacuum to obtain the gel precursor. Gel powder is grounded and calcined under inert atmosphere mostly in a tubular furnace.

The sol–gel process is characterized by a high purity and small particle size, but its main drawback is the great volume shrinkage characteristics during drying process.

Ultrasonic spray drying: After ion precursors are dissolved in distilled water, ultrasonic spray is applied to conduct pyrolysis at 500°C followed by heat treatment at sintering temperature (600 to 800 °C) under inert atmosphere.[33]-[34, 35]

Co-precipitation: This method includes heating the aqueous solution containing Li^{+}, Fe^{2+} and P^{5+} above 105 °C in a pH range of 6 to10 in order to get pure LFP instead of Li_3PO_4 and $Fe_3(PO_4)_2$. After temperature increased more than the solvent boiling point, LFP stars to precipitate. In the next step, LFP must be calcined at 500 °C under a slightly reducing agent [36, 37].

1.3.3 Melt casting

Melt casting is another approach of LFP fabrication in which all the precursors are mixed and melted within an airtight box furnace at a temperature between 950 and 1050 °C under a flow of argon or nitrogen in a graphite or alumina crucible. Then this melt is poured into a cast and cooled down in the atmosphere followed by crushing and grounding to make the particles in nano scale. Daheron et al (2011) showed that by this method pure LFP could be obtained through the stoichiometric combination of Li, Fe and phosphorous precursors[38] . They proved that melt synthesis has the advantage of ideal liquid-phase rapid reaction kinetics to provide a product with high density. Talebi et al (2016) claim that this technic, due to the simplicity of the process, short reaction time and its economy cost, is going to become a competitive LFP synthesis route for large-scale production [38-40].

Optimization of this process is still under investigation in all aspects to reach in order for an industrial scale.

Nevertheless traditional solid-state technique with all its benefits (easy processing) and limitations (large particle size and long process) is the most common method of LFP fabrication[12]. However, research in both industry and academia is still extensively continued to develop a new economic and efficient synthesis route to produce an optimized LFP material in terms of cost and maximum possible performance in the automotive industry.

In Table 1.2, a brief summary of various methods of LFP fabrication with some examples of the most common precursors is presented.

Table 1.2: Various LFP synthesis methods

Method of synthesis	Raw material	Ref	Advantage	Disadvantage
Mechanochemical activation	Li_3PO_4+$Fe_3(PO_4)$	[41]	Easy processing Low cost of equipment C-LFP possible in 1 step	Time consuming Incomplete reaction and nonreversible side reactions High cost of precursors
Carbothermal reduction	Iron oxalate+ $NH_4H_2PO_4$+Li_2CO_3	[19]	Effective in homogeneity and particle size	
Microwave heating	Iron lactate +$NH_4H_2PO_4$+Li_2CO_3 Li_3PO_4+$Fe_3(PO_4)_2.8H_2O$+C	[20]	Very fast and uniform heating	
Hydrothermal	$FeSO_4$+H_3PO_4+LiOH	[42]	High purity and homogeneity Low temperature process Controllable the structure, morphology and particle size	Waste recycling cost Large scale installations
Sol-gel	Li acetate + Fe acetate+H_3PO_4	[43]		
Co-precipitation	$FePO_4.H_2O$+$FeSO_4.7H_2O$ +$NH_4H_2PO_4$	[36]		
Spray pyrolysis	$LiNO_3$+$Fe(NO_3)_3.9H_2O$+H_3PO	[35]		
Molten state	Fe_2O_3+Fe+LiOH Fe_2O_3+Li_2CO_3+$NH_4H_2PO_4$ FeO+P_2O_5+LiOH	[39]	Easy process No waste water Rapid and complete reaction at liquid phase Low Cost of precursors	Requires sub micrometer powderization to get products for power applications 2 steps of LFP fabrication and C coating

1.4 Feebleness of LFP and its enhancement methods

Despite all the advantages of LFP as a promising cathode material for the Li-ion batteries, it severely suffers from poor ionic (lithium ion diffusion coefficient) and electric conduction whereas many of electrochemical properties are linked with the conductivity of cathode material.

The first step to optimize the conductivity of an electrochemical cell is to discern the main source of resistance. Resistance in the electrode is mainly due to (a) the ionic and electronic resistance of the material and/or (b) the interfacial resistance from the electrode/electrolyte boundaries. It is well known that the ionic conductivity and electrical conductivity of the electrode materials is lower than that of the electrolyte.

High internal resistance leads to heat generation inside the battery cell during charge/discharge process that causes an increase in temperature and accelerates degradation of the battery life[6].

Since emerge of LFP, so many efforts have been performed to minimize the defects of the olivine structure. Basically, all the efforts can be categorized in two main domains:

1. *Improvement on the synthesis of the material* by optimization of particle size, surface and morphology or Ion doping. By modifying the structure of the material, we could overcome the low conductivity weakness. As discussed before, LFP synthesis method directly influence the structure and performance of the material [5].

2. *Adding a conductive network* to the cathode materials including carbon, metal or metal oxides [12]. Low electrical conductivity of $LiFePO_4$ (10^{-9} $S.cm^{-1}$) could be overcome by adding a conductive material to the electrode.

Rate capacity problem in LFP is due to the electrical conductivity limitations. The transport properties of lithium ions are largely determined by the topology of the olivine structure.

It is noteworthy that if the olivine structures did not block the 1D channels and there was no electrical conductivity problems associated with iron, the high intrinsic ionic conductivity of the olivine structure could provide a very good rate capability [44].

Figure 1.5 shows the mechanism of ionic conductivity and the oxidation/reduction reactions occurring during charging in a battery cell.

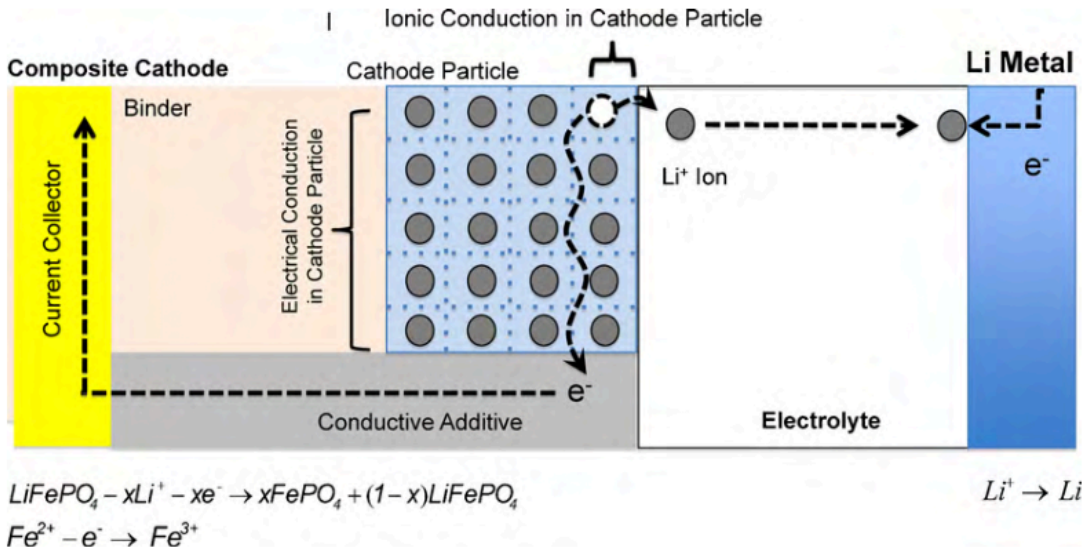

Figure 1.5: Conduction in LFP cathode during charging [45]

1.4.1 Why nano-size LFP?

Physical properties such as morphology, particle size distribution, crystal size and shape of the LFP powders effect on battery performance. Tailoring particle size of the cathode is an effective way to improve ionic conductivity. Large effective surface area, short ion diffusion pathway and fast kinetics of redox reaction are some properties attributed to the fine LFP powders. Therefore, such powders increase dramatically the rate capability of the batteries because many more pathways are supplied in order for Li^+ ions and electrons to transfer under such very fine particle sizes [19, 46]. In addition to the electrochemical properties of the cathode material, the morphology and microstructure effects on cathode performance [11].

The surface free energy of nanomaterial can be calculated by the Reaction 1-2[47]:

$$\mu^\circ(r)=\mu^\circ(r=\infty) + 2(\gamma/r)v \qquad \text{Reaction 1-2}$$

In which μ° is the chemical potential, γ is the effective surface tension, r is the particle radius and v is the partial molar volume. According to this equation, decreasing particle size results in higher surface energy. The large surface free energy, surface defects and surface states critically influence the chemical reactivity of the material and also enhance the phase stability and

structural transformation; therefore, affecting the electrochemical and catalytic activity.

According to the diffusion formula $t = L^2/2D$ (where t, L and D are the diffusion time, diffusion distance and diffusion coefficient, respectively), two strategies should be employed in order to decrease diffusion time[48]. First one is increasing diffusion coefficient (D) by material doping and second one is decreasing diffusion length (L) by using nanostructure material. In other words, the smaller of the particle size, the shorter diffusion time of lithium ions in LFP powders.

Consequently, utilization of LFP nano powders results in a much enhanced electrochemical performances, particularly when high rates of charge-discharge are expected. Nanostructure improves mechanical strength and structure, and it provides more resistance to the mechanical damage. Moreover, electrochemical activity and stability can be improved due to increased number of active reaction sites and facile transport of electro-active species to the reaction sites[49].

Decreasing the particle size, controlling the morphology of LFP powders with porous nanostructures or multi-hollow microstructure to increase the electrode/electrolyte interface has the potential to improve rate performance of such powders. However, there are some adverse effects of nanoparticles including [12, 47, 48]:

- Lowering tap density to about 0.6-1.0 g/cm^{-3} which causes more supporting material to be used in positive electrode, more electrolyte, separator and packaging which result in increasing cell size and cost;
- Higher surface area and less-coordinated surface atoms causes more prone to surface reaction and particle dissolution with the electrolyte. Also, risk of secondary reactions, involving electrolyte decomposition, is high that contributes to low columbic efficiency and cycle life;
- Difficult and costly nanoparticle's processing and holding;
- Safety and health concerns;
- Nanoparticles make agglomeration during synthesis which makes it difficult to uniformly disperse in the electrode;
- There are problems in large-scale production, separation and mixing with carbon.

Currently, materials that are used for Li^- ion batteries manufacturing are in the size range of 1 to

10 micron. Although tailoring particle size to nano size enhances the electrochemical properties intensively, between 50 and 400 nanometers, specific capacity doesn't depend on the particle size, since at this range, insertion/extraction is not diffusion-controlled. Then particle size reduction below 100 nm may not lead to improvement of rate performance as expected. The best and highest rate performance belongs to the size of 30 to 50 nm. Similar results have been obtained, however, with the LFP powders of 200 to 400 nm with carbon coating[47].

1.4.2 Doping

Doping supervalent ions or metal oxides is another way to improve conductivity and electrochemical performance of the cathode materials. This method comprises substitution of trace amount of metal supervalent ions such as Mg^{2+}, Al^{3+}, Na^{+}, Cr, Zn, Ti^{4+} and Zr^{4+} [50, 51] by Li (M_1), Fe (M_2) and O^{2-} sites. Typically, metal doping enhances electrode performance by stabilizing crystal structure as well as increasing lattice parameters, which facilitate Li^{+} ion transportation. Stability of the crystal structure results in cycle performance enhancement. [52]. The advantage of doping method is that there is no more process step required and metal dopant could be added to the material during the synthesis process. Also, dopant increases the intrinsic conductivity of the material while surface coating improves the conductivity of the bulk [53].

However, microstructure of the crystal is changed by the dopants. Therefore, interpretation of the doping effect and morphology change on the electrode performance is complicated. Also, sometimes doping has negative effects on the cathode performance and the amount of the dopant has to be controlled precisely. For instance, Al which is a commonly used dopant, decreases capacity because it occupies Fe sites even though Al cannot be oxidized completely and the transition metal iron replaced with aluminum represents one less oxidizable ion. Nevertheless, doped materials do not show significant enhancement in electrochemical properties and also due to the negative impact on the cost of the cell, it is not effective for large applications [11, 45].

1.4.3 Carbon Coating

One of the effective ways to slow down the rate of the side reactions is to provide a protective passivation film for the cathode by surface coating. Many literatures showed that surface coating could improve capacity retention, rate capability and thermal stability [6, 54-57]. This results in either changing the surface chemistry or providing a physical protection layer. Therefore, the

coated film impedes the side reactions between the cathode material and the electrolyte. Also, the coated film provides an electron conducting media to facilitate charge transfer at the surface of the particles [58].

Generally, two surface coating methods are:

1. Mechanical mixing of material with the coating precursor [59];
2. Heat treatment of mixture at an elevated enough temperature.

In the first method, coating layer is very rough; in other words, coating material is accumulated in some spots of the surface while some other surface spots are either uncoated or coated by a very thin layer.

Various candidate materials have been employed for surface coating such as carbon, metal powders, e.g. Ag^{+}, metal oxides, e.g. ZnO, CuO and TiO_2, metal fluoride, glass composite [58] as well as metal phosphates (Fe_2P) [60] and some others [61]. Among these coating candidates, carbon is the most common and promising material due to its multi-functional advantages arising from its unique physical and chemical properties such as high electrical conductivity, superior chemical and electrochemical stability, abundantly precursors and its low price [6, 58]. Carbon coating plays the main role to enhance surface conductivity in which active material can be fully utilized at high current rate. In addition, carbon coating leads to improvement of the specific capacity, rate performance and cycling life.

To achieve carbon coated LFP powders with high performance in a battery cell, the carbon coating step should be optimized based on carbon content and thickness, carbon nature, e.g. graphite or diamond, morphology and distribution, surface and porosity, precursor and the coating process of the coating [62].

1.4.3.1 Carbon content and thickness

Although carbon is used to enhance the electric conductivity of the material, its content must be optimized on the LFP surface due to the prohibition effect of the coated layer for lithium ion transportation. By increasing mass of carbon in the precursor per mass of LFP, coating layer will become thicker. Accordingly, this will result in decreasing the tap density and also the reversible capacity due to the hindered lithium ion transport. Decreasing the tap density, consequently, will

result in enlargement of both mass and volume size of the battery since more basemen and active material will be required [63, 64].

Tap density is also dependent on morphology of the LFP powders and their particle size distribution. For instance, agglomerations of spherical particles with wide particle size distribution shows a higher tap density [49].

1.4.3.2 Carbon nature and structure

Electrode performance and rate behavior in an electrochemical cell is not characterized by the amount of the deposited carbon on the LFP surface, but it also is strongly influenced by the structure of carbon, particularly sp2/sp3 and disordered/graphene ratio correlates with electronic conductivity. Graphitic portion of the deposited carbon, i.e. carbon with lower D/G ratio where D stands for disordered or diamond carbon and G stands for graphene, is much more desirable due to providing higher electrical conductivity[6, 49].

Carbon via different structures as carbon nanotubes, carbon black and graphene has been investigated. Each types of carbon provides different properties. Conventional carbon additives such as carbon black possess relatively low electronic conductivities when compared with more crystalline forms of carbon. Carbon nanotube (CNT) possesses a high electrical conductivity and network structure. In comparison with carbon black and CNT, graphene offers improved interfacial contact and shows superior electrical conductivity due to the flexible structure and its high surface area[55]. Graphene has an extremely high surface/mass ratio where the sp2 bonded carbon atoms are arranged in a hexagonal 2D lattice [65]. Hence graphene is an exceptionably suitable candidate for application in lithium ion battery cathodes as an electron-conducting additive.

Graphite consists of several 2D sheets of graphene that are coupled in parallel with van der waals interactions. More importantly, the anisotropic behavior of graphite provides a pathway for electrons to current in directions parallel with the graphene layers. Having said that, electrons thus have a pathway to transfer easily to the outer circuit of the battery cell provided uniform coating of all the cathode powders.

1.4.3.3 Morphology and distribution

Provided a proper coating process is applied, each primary particle is coated with a layer of conductive carbon where electrons can pass along the surface so that the electronic transport length in an electrode is shortened. This coated layer can reduce the interface resistance.

Coating morphology could be classified in three categories: core-shell, ultra-thin and rough coating that the schematic could be observed Figure 1.6.

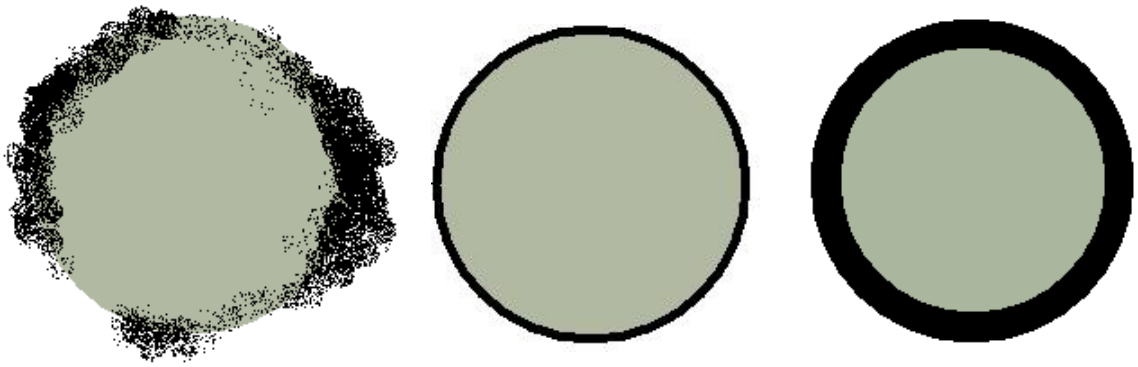

(a) Rough Coating (b) Ultra-fine Coating (c) Core-Shell Coating

Figure 1.6: Morphology of the surface coating layer

Coating layer in rough coating is inhomogeneous meaning that some areas are thickly coated while some areas remain uncoated or coated with a thin layer. This kind of coating is suitable for HF scavenger and surface modification[58].

Core-shell coating involves homogeneous and thick layer of coating material (shell) around each particle of the active material (core). This type of coating benefits from satisfactory electrochemical performance of the core as well as stability of the sell. However, mismatch between core material shell materials triggers mechanical stress. Having such a mechanical stress causes fatigue of both core and shell materials in each charging/discharging cycle, and it results

in some cracks in the shell, which is not desired. Also, in terms of carbon coating, high thickness of the coated layer inhibits the transportation of the Li^+ ions.

In order to compensate weaknesses of the two previous models in term of electronic conductivity, researchers developed thin coating techniques, which meet advantages of the core-shell model while it is suitable for electrical and ionic conductivity [58].

1.4.3.4 Carbon precursor

Structure of carbon depends on the carbon precursor and carbon generation/deposition process conditions [62, 66]. If carbon precursor doesn't have sufficient time and temperature to decompose, H/C ratio of the deposited carbon will be undesirably high and it will have negative effect on the electrochemical performance. Moreover, D/G ratio depends on the pyrolysis temperature and the type of carbon precursor. In general, optimum D/G ratio will be achieved at an elevated enough temperature. However, the process has to respect the max temperature constrains such as LFP sintering temperature, i.e. around 750 °C, and/or its melting point (at 930 °C).So, carbon precursors that can get decomposed at a temperature lower than 750 °C are desired.

Generally, carbon precursors are classified into two groups: 1) pure solid carbon such as graphene[54, 55] ; 2) various gases and liquids containing hetero-elements such as organic materials, polymers and hydrocarbons[26, 34, 67].

A pure solid carbon could be coated by thermal or ion beam treatments. As an example, graphene appears to be one of the best electron conducting additives due to its high electron conductivity and large specific surface area. In this case, graphene oxide (GO) is the most common material used as the precursor. Mostly, GO mixed with LFP precursors and conventional synthesis methods are used for producing graphene containing cathode material. Synthesis process involves heating the mixture at 750 °C in a reducing Ar/H_2 atmosphere. As a result, synthesis of LFP and GO reduction takes place simultaneously[55]. Several graphene composite structures can be obtained, such as active cathode material particles anchored on graphene, mixed with graphene, and wrapped or encapsulated in graphene[55, 68]. However, it is still unclear which of these structures offer better cathode electrochemical properties.

Pyrolyzing a gas, liquid or solid phase precursor on the surface of the LFP powders is the most effective way of carbon deposition. Such a pyrolysis process is applicable during or after synthesis of LFP materials. Sucrose and glucose [69] are the most used ones; whereas, Chen et al (2012) found that glucose is a better candidate and shows higher initial discharge capacity [70]. Carboxylic acids are also a common carbon precursor. For instance, citric acid in sol-gel synthesis method is widely used, and decent C-LFP is produced from.

Generally, the carbon coating process is either in-situ [37] or ex-situ based on the carbon precursor and on the LFP synthesis process.

1.4.3.4.1 In-situ C-coating of LFP powders

In in-situ coating, carbon can be added by one of the component of an active material precursor (iron citrate, lithium carbonate, etc.) [71, 72] in the form of a polymer [73, 74] or carbon molecules such as sucrose, glucose, graphite and carbon black.

Shin et al (2006) used graphite, carbon black and acetylene black as carbon precursor in the coating process to investigated the effect of different carbon precursors on the electrochemical properties [54]. They reported that coated samples with graphite demonstrated the highest electrical conductivity and the best performance.

Cheng et al (2013) synthesized C/$LiFePO_4$ with the low cost Fe_2O_3 as the iron precursor and β-lactose in 2 steps: $LiFePO_4(OH)$ was firstly prepared and then β-lactose was added. Utilization of lactose was to make a reduction atmosphere for $LiFePO_4(OH)$ while it was the carbon precursor. This method combines advantages of both hydrothermal and solid-state synthesis methods[75].

Commonly, in-situ coating process includes three steps:

- Synthesizing active nanoparticles;
- Mixing as-prepared material with carbon precursor;
- Sintering and carbonization of the mixture at an elevated temperature (500 to 700 °C).

However, this method cannot be a promising method because there is no control on the coating process in term of adjustment of operating conditions. Mostly, $LiFePO_4$ particles are not uniformly coated, and carbon is formed in both forms of graphite and amorphous.

1.4.3.4.2 Ex-situ C-coating of LFP powders

This method consists of adding carbon precursor after the active material is prepared. Carbon will be deposited on the particles surface by decomposition of the precursor, e.g. in a pyrolysis reaction, at an elevated temperature. For instance, the carbon precursor, e.g. a polymer or a hydrocarbon, can be added to the sample followed by mixture heat-up to an elevated temperature to carbonize the coated material; finally, a thin layer of carbon will be deposited on the particles.

Zhao et al (2009) compared two coating processes of in-situ with polyvinyl alcohol (PVA) and ex-situ with CVD of benzene solution [73]. They showed that CVD of the aromatic matters at high temperature causes carbon graphitization, so this sample exhibited better discharge capacity (155.4 and 135.8 mAh/g at 0.1 C and 1 C, respectively) in comparison with the applied in-situ method. Belharouk et al (2005) employed propylene as the carbon precursor to deposit carbon on the surface of the particles by pyrolysis at an elevated temperature. Compared to an in-situ coating method where LFP was mixed with resorcinol-formaldehyde, they got a thin and much uniform coating layer with lower area specific impedance [16].

Generally, ex-situ coating has some dominant advantages: high purified LFP, better control on the coating process by manipulating reaction conditions, and enhancement of the carbon structure [76].

1.5 Chemical vapor deposition

Chemical vapor deposition (CVD) is defined as a process of decomposition and/ or chemical reaction of gaseous reactants on or in the vicinity of a heated substrate surface in an activated medium such as high temperature or plasma environment that leads to the formation of a layer of solid material on the surface [77, 78].

CVD technology is suitable for preparation of bulk materials, composites, films and coatings due to the several advantages such as:

- Capability to produce highly pure and dense material;
- Produces uniform film with good conformal coverage;
- Controllable rate of deposition, structure, surface morphology and orientation by adjusting process conditions;

- Flexibility of using wide range of chemical precursors;
- Reasonable process cost.

Previously, CVD was employed in production of high purity refractory metals like Ti and Ni as well as manufacturing of the electronic semiconductors. Recently, it has found importance in aerospace, science and engineering. Particularly, it has tremendous applications in surface modification and coating.

Based on the chemical activation method, CVD process is classified to thermal-activated (TACVD), plasma enhanced (PECVD), photo-initiated (PICVD), metalorganic (MOCVD), flame assisted (FAVD), electrochemical vapor deposition (EVD) and chemical vapor infiltration (CVI). In the conventional TACVD, thermal energy is used to activate the chemical reaction.

Generally, there are two reaction mechanisms in a chemical vapor deposition reactor: homogenous gas-phase and heterogeneous surface reactions. As a CVD example, given thermal decomposition of a hydrocarbon is employed for carbon deposition, following reaction mechanisms occur[77, 79]:

Homogeneous gas-phase: such reactions include: (1) dehydrogenation reaction for both aliphatic and aromatic hydrocarbons and (2) cracking reaction (scission of C-C bond). In the first step, gaseous reactant decomposes and radicals are formed. The radicals are then immediately recombined and produce intermediate products as non-saturated species (aliphatic). If the temperature is higher than the decomposition temperature of these intermediate products, they will undergo chemical reaction and produce gaseous by-products and solid powder so that the by-product gases vent out of the reactor. When temperature is below the decomposition temperature of the intermediate phase, these intermediates diffuse to the boundary layer to reach the heated surface of the substrate to undergo heterogeneous surface reactions.

Heterogeneous surface reaction: Upon diffusion of the intermediates to the heated surface of the LFP powders, gas-solid reactions (carbon nucleation and growth process) occur. Solid carbon will be deposited on the particles surface and gas by-products desorbed and leave the reaction chamber.

CHAPTER 2 PROBLEM IDENTIFICATION AND OBJECTIVES

Li ion rechargeable batteries have a lot of applications in commercial and automotive industries. One of the most popular applications that have attracted a keen interest of research from academia and industry is to employ such batteries as energy source of the required propulsion in electric vehicles (EV) and hybrid electric vehicles (HEV).

Such batteries in EVs and HEVs must have some critical characteristics such as:

- Provision of the demanding energy capacity;
- Safe utilization;
- Reasonably economical.

As discussed in earlier sections, cathode of rechargeable batteries contributes to 70 % of total cost of a battery cell. Therefore, to lower the cost of a battery, fabrication of the cathode takes the majority of research and development strategies. Among many different candidate materials for the cathode, LFP is one of the best choices of cathode materials due to advantages such as its precursors availability, low synthesis cost, high energy density and highly safe operation in a battery cell.

However, with respect to the desired specifications, LFP suffers from low conductivity and low ion conductivity.

Ionic conductivity is related to the diffusion of Li ions within the cathode network. Therefor, by reducing the particle size to 50 to 400 nm, we can overcome this weakness. Having smaller particle size is not desirable since it affects on the stability of the material, so it will increase the reduction/oxidation reaction rate.

Enhancement of the electrical conductivity, on the other hand, is achievable by carbon coating on the surface of LFP powders that are building material of the cathode electrode. Coated carbon also helps a rechargeable battery afford longer cycle life.

Despite the advantageous carbon coating strategy, there have been challenges such as costly process, excess deposited carbon (dead weight), non-uniform carbon layer and undesired type of the coated carbon. Micrographs of coated particles show that the carbon deposits from the common approaches are not uniformly distributed on the surface of LFP powders resulting in

appearance of lump layers of carbon. The presence of lump carbon layers on the surface is believed to be the cause of lower energy density and lower process ability of the produced C-LFP powders [49].

Alternatively, a CVD coating process with a gas-phase carbon precursor, through which a more uniform layer of coated carbon on the surface of LFP powders is accomplished and it facilitates better control over the thickness and type of the coated carbon is believed to be a solution to overcome or enhance both limitations involved in the traditional C-LFP production processes.

A gas-phase precursor brings three important advantages: 1) there is no need to an upstream vaporization step which is very energy intensive; 2) the gaseous precursor can easily diffuse and directly reach surface of the LFP powders; 3) there is considerably a much less trace of contaminants such as sulphur and phosphor that can be present in solid or liquid carbon precursors, e.g. biomass and petroleum oils.

Efficient gas-solid contact between the gaseous precursor and LFP powders is still a very impotent parameter that must be taken into consideration, in particular, when LFP powders are synthesized in nano size that form secondary cohesive agglomerates.

Based on the mentioned problems, the main objective of this research was:

Gas-phase carbon coating of LFP nanoparticles via CVD process in a fluidized-bed system.

The two specific objectives that were investigated in this research are:

1. To evaluate and optimize the CVD operating conditions, e.g. type of precursor, temperature, reaction time and particle size of LFP, in a fluidized bed system;
2. To develop a new pulse-assisted fluidized bed reactor to overcome inter particular forces between fine LFP powders at elevated temperatures.

In a fluidized bed CVD reactor, by virtue of having a high mass transfer and heat transfer rate between solid particles and the gas, which lead to uniform temperature distribution and uniform gas-solid contact, it is very likely that a uniform layer of coating is achieved. In a fluidized bed CVD system, we can have a control on the quality and thickness of the coated layer by altering concentration of carbon precursor, temperature, gas residence time and reaction time. In addition, we can decrease or eliminate agglomeration of LFP powders.

Given the fact that LFP powders were in the range of submicron size, i.e. they were very cohesive, we developed a pulse-assisted fluidized bed CVD process, and managed to overcome inter particular forces between the fine powders at ambient conditions and also during chemical vapor deposition process at elevated temperature.

CHAPTER 3 EXPERIMENTAL PROCEDURES

According to objectives of this research, carbon coating of LFP powders was investigated via a high temperature chemical vapor deposition process. During the CVD reaction, as discussed in introduction section, a gas-phase carbon precursor undergoes homogeneous gas reactions in the gas-phase followed by heterogeneous reactions between diffused gases and the heated surface of LFP powders. As a result, solid carbon, which is generated from decomposition of the gas, will be deposited on the surface of LFP powders as a solid coated layer.

To proceed with investigation on this CVD process, several experimental parameters had to be set such as:

- Selection of LFP powders;
- Selection of carbon precursor;
- Experimental setup;
- Characterization techniques.

3.1 Selection of LFP powders

LFP powders of P1, P2 and P3 synthesized by three different methods were supplied from different sources at the beginning of the research. P1, P2 and P3 represented materials synthesized by solid-state, hydrothermal and melt casting methods respectively. As discussed earlier, LFP powders must have been in nano size to enhance the ionic conductivity. Therefore, P1 powders were rejected because their lowest primary size was larger than 10 μm (Figure 3.1). Also, neuron activation analysis (NAA) revealed that P1 powders contained undesired elements of Mn, Na, Al, Si and S.

This project was in fact part of a large project to do with development of a new melt casting process where P3 powders are produced. Since this process was not optimized at the initiation of this project, P3 samples with different characteristics and very low quantities were available. Therefore, it was decided to continue the research with P2 samples that were prepared at University of Montreal with relatively enough quantity, and with a more consistent composition over the duration of the project.

P2 samples contained primary particles of a diameter below 100 nm (Figure 3.1). However, the as-received samples contained powders with a secondary size distribution of 5 to 800 µm. It was because the primary powders stick together due to severe presence of interparticle forces after a drying step following the hydrothermal process. To run the experiments, we had to sieve the P2 samples to the desired size distribution.

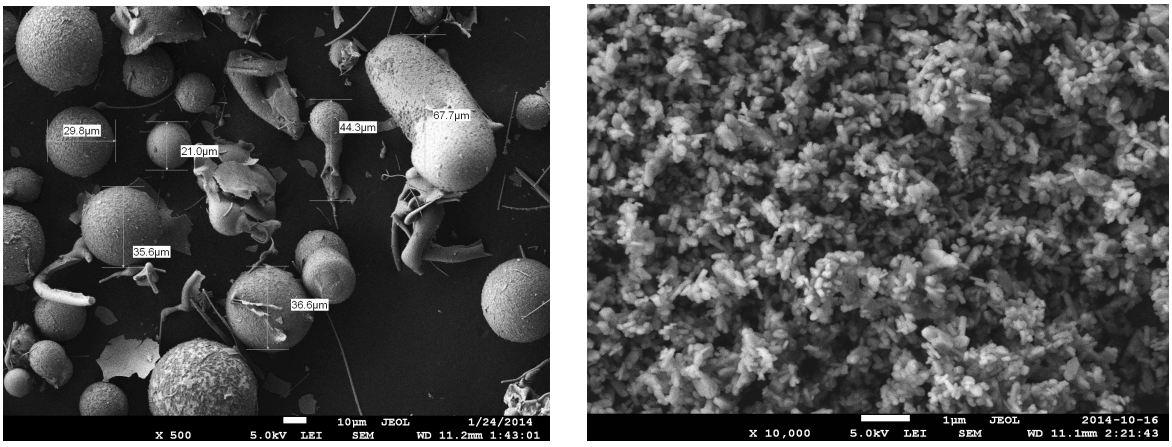

(a) (b)

Figure 3.1: SEM images of fresh LFP powders; (a) P1 and (b) P2

3.2 Selection of carbon precursor

Our high temperature CVD process, in fact, is a pyrolysis process where a hydrocarbon undergoes thermal decomposition in the absence of oxygen. In other words, pyrolytic carbon is deposited on the surface of LFP powders.

An ideal carbon precusor should produce high enough mass of graphite carbon at lower temprature at the lowest cost. Coating a layer of carbon on the surface of LFP powders depends on both rate of carbon production inside the reactor and rate of carbon deposition. Therefore, selection of an appropriate carbon precursor with a potential of generating maximum amount of graphite carbon is very crucial. Certainly, cost of carbon precursor and absence of contaminants are another factors that must be taken into considrration as well. FactSage thermodynamic software, developed at Ecole Polytechnique de Monyreal, was employed to study decompoisition of different precursors such as methane, glycerol, acethylene and propylene. The carbon

precursors were evaluated based on carbon production in the bed of LFP powders at equilibrium state.

3.2.1 Methane

Methane (CH_4) is the most readily available hydrocarbon that was considered. However, our initial pyrolysis tests revealed that methane started to decompose at temperatures above 900°C and a conversion above 50% was obtained when temperature was higher than 1000°C. Given the fact that melting point of LFP powders is around 930°C, it can vary depending on composition of LFP, and its sintering temperature is around 750°C, pyrolysis of methane was found an inappropriate process for carbon production.

Our experimental observation was in opposite to thermodynamic evaluation (Figure 3.2) when equilibrium ratio (ER in Equation 3) was zero. In other words, 80% of methane was supposed to convert to carbon at 700°C provided equilibrium state was reached. Therefore, it looks like that our experimental condition was kinetically controlled and it was far from equilibrium. It was mainly due to short residence time of methane in our experiments.

$$ER = \frac{\textit{Actual moles of oxygen to burn 1 mole of carbon}}{\textit{stoichiometric moles of oxygen required to fully burn i mole of carbon}} \qquad \text{Equation 3}$$

It was decided to investigate whether it was possible to partially burn methane with a very low ER so that large enough mass of carbon was produced at a temperature much lower than sintering temperature of LFP. Such a partial oxidation of methane was evaluated with FactSage and results are presented in Figure 3.2 for temperatures of 300, 500 and 700°C where ER varied from zero to 0.1. Methane, hydrogen, carbon monoxide, carbon dioxide and graphite carbon were the main products that existed at equilibrium. It is noteworthy that diamond carbon does not exist at equilibrium.

Assuming that equilibrium state is reached, according to the graphs in Figure 3.2, even though increase of ER favors carbon production at temperatures of 300 and 500°C, it is still much less than the mass generated at 700 °C. On the other hand, generation of carbon decreases at equilibrium by an increase of ER.

Therefore, we concluded that methane was not an appropriate carbon precursor for production of C-LFP.

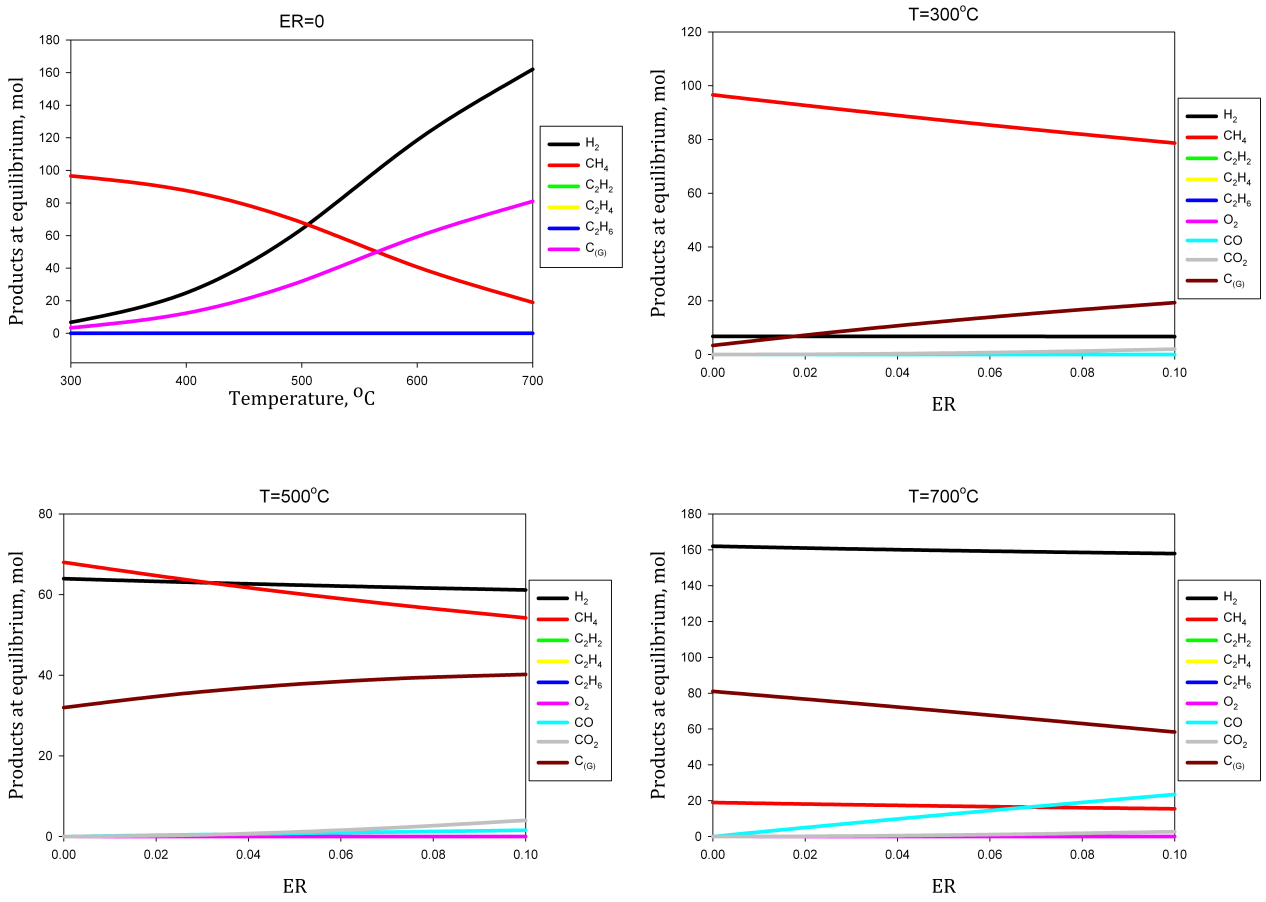

Figure 3.2: Equilibrium analysis to estimate evolution of carbon from partial oxidation of 100 moles of methane

3.2.2 Glycerol

Glycerol was selected as a reperesetative of oxygenated organics with general formula of $C_nH_mO_k$, for instance, sugars and biomass. Figure 3.3 llustrates evolution of products at equilibrium upon pyrolysis of glycerol ($C_3H_8O_3$) at temperatures from 300 to 1000 °C. Hydrogen and carbon monoxide were the main gases at equilibrium and generation of carbon tended to be zero at temperatures above 700°C. In fact, since glycerol is an oxygenated organic compound, some steam is generated, but it converts to hydrocarbons and carbon at high temperatures through the endothermic stearm reforming reactions (Equation 4 and Equation 5):

$$C_nH_m + nH_2O \rightarrow nCO + \left(\frac{m}{2} + n\right)H_2\,, \qquad \Delta H > 0$$ Equation 4

$$C + H_2O \rightarrow CO + H_2, \qquad \Delta H > 0$$ Equation 5

The exothermic water-gas shift reaction (Equation 6) is not influential at temperatures above 700 °C that explains why carbon monoxide production exceeds carbon dioxide production. The inactive exothermic Boudouard reaction (Equation 7) at such high temperatures also explains another reason of carbon disappearance (reverse of Equation 7).

$$CO + H_2O \leftrightarrow CO_2 + H_2, \qquad \Delta H < 0$$ Equation 6

$$2CO \leftrightarrow CO_2 + C, \qquad \Delta H < 0$$ Equation 7

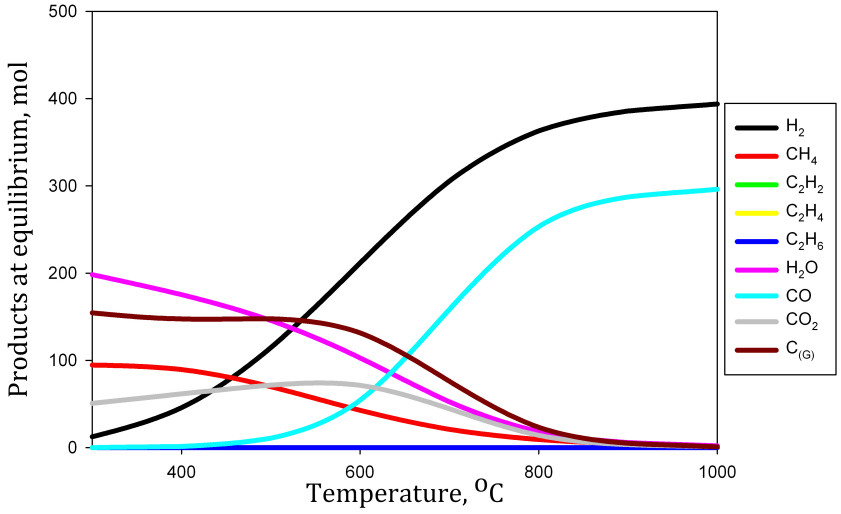

Figure 3.3: Equilibrium analysis to estimate evolution of carbon from pyrolysis of 100 moles of glycerol

According to thermodynamic analysis described above and Figure 3.3, we thought that we should pyrolyze glycerol at a temperature below 500 °C. However, after an experimental test at 400 °C, we observed that LFP powders were oxidized and their color was red. This could be explained by detrimental presence of steam (Figure 3.3) that reacted with iron content of LFP powders and resulted in generation of non-conductive Fe_2O_3. Therefore, we concluded that glycerol could not be an appropriate precursor of carbon for C-LFP production.

3.2.3 Acethylene and Propylene

Thermodynamic analysis of pyrolyis of acethylene (Figure 3.4) and propylene (Figure 3.5) revealed that hydrogen and carbon are the main products at equilibrium at temperatures above 300 °C, so they both were found appropriate carbon precursors for C-LFP production. However, as depicted in Figure 3.5 pyrolysis of propylene tends to generate much more graphite carbon, particularly, at temperatures above 600 °C.

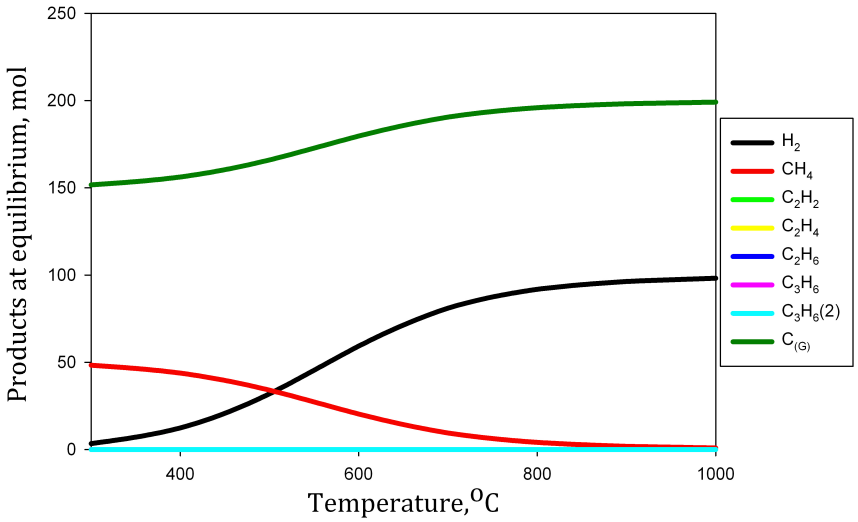

Figure 3.4: Equilibrium analysis to estimate evolution of carbon from pyrolysis of 100 moles of acetylene

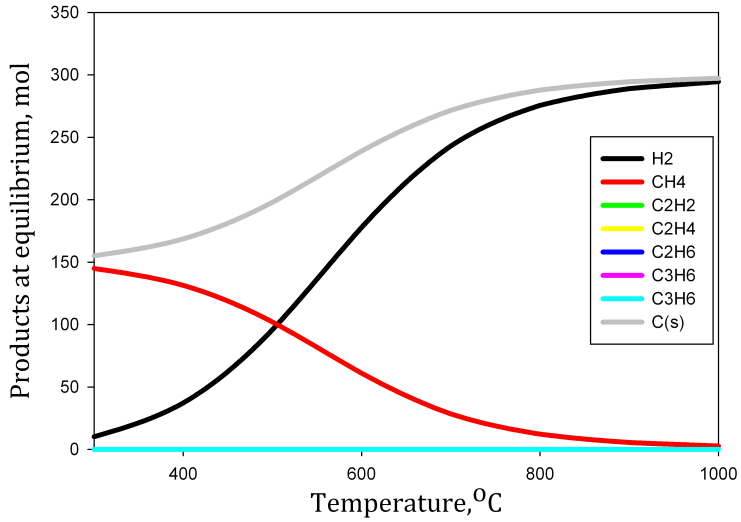

Figure 3.5: Equilibrium analysis to estimate evolution of carbon from pyrolysis of 100 moles of propylene

Figure 3.6 reveals comparative evolution of graphitic carbon versus temperature to better evaluate the precursors in term of production of graphitic carbon. Whereas glycerol, acetylene and propylene have the potential to generate graphite carbon below sintering temperature of LFP powders, propyelene was selected as the most favorable carbon precursor for C-LFP production.

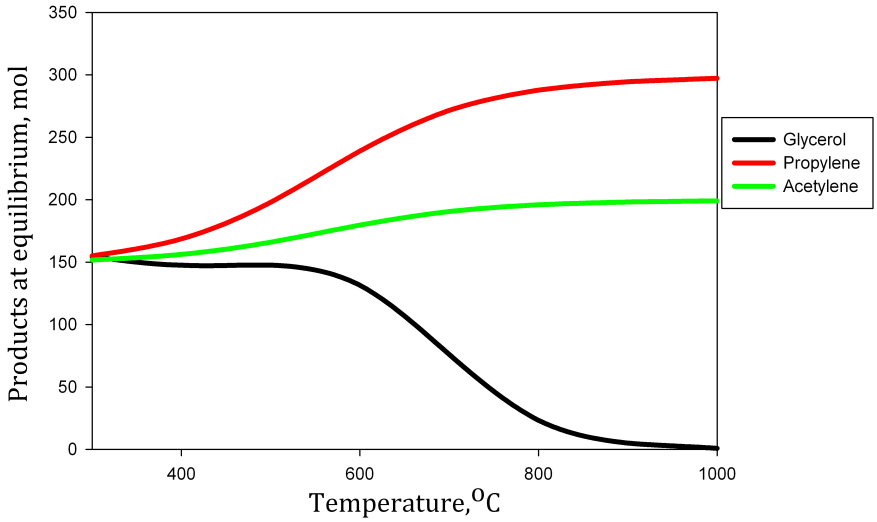

Figure 3.6: Comparison of graphitic carbon production from different precursors at equilibrium; input precursors; 100 moles

To proceed with the CVD investigation, tests were carried out with two mixtures of propylene:

- Mixture of nitrogen and 3 mol% propylene for the sake of safety concerns in an industrial scale;
- Mixture of nitrogen and 50 mol% propylene. As it will be discussed, provided safety concerns are satisfactorily met, much shorter reaction times were thought to be necessary with such a concentrated mixture as well as higher probability of contact between propylene molecules with surface of LFP powders.

3.3 Fluidized bed CVD reactor

Fluidized bed reactors offer prominent advantages concerning carbon coating of LFP powders in a CVD process. By virtue of having a high mass transfer and heat transfer between solid particles and the gas, it is possible to reach a uniform temperature distribution, and a uniform layer of coating. We can control quality and thickness of the coated layer in a fluidized bed CVD, for instance, by altering concentration of carbon precursor, reaction time, gas residence time and temperature. In addition, we can decrease or eliminate the particles agglomeration. It is noteworthy that since a gaseous carbon precursor is employed in the fluidized bed reactor, despite the precursors that inherently have undesired elements, the probability of presence of contaminants in the final C-LFP product is accordingly minimized.

The induction heating fluidized bed reactor (IHFBR) setup [1] that was designed and developed at Ecole Polytechnic de Montreal was utilized to carry out the CVD tests. However, several modifications were applied in order for such reaction tests. In fact, the original IHFBR employs a lift tube mechanism to feed a solid feedstock in-situ from its bottom to the reaction zone in less than a second. However, the lift tube was not required for carbon coating of LFP powders because the feedstock, carbon precursor, was propylene, and LFP had to be kept on top of a gas distributor to be fluidized. Accordingly, installation of the eight internal platinum rods, i.e. heating elements of the induction heating mechanism, on the distributor was very challenging as it required a delicate and costly machine job.

On the other hand, our initial CVD tests at 700 °C while employing the platinum rods revealed that due to small size distribution of LFP powders, i.e. less than 250 μm, the platinum rods generated a severe wall effect against mixing of LFP bed; this resulted in much hotter surface of the rods passing sintering temperature of LFP powders. Thus, the LFP bed was clogged and a

poor carbon coating occurred on the surface of LFP powders. It has been shown that provided the solid particles are well mixed in the induction heating zone with the internal rods as the heating elements, temperature gradient between surface of the rods and the bed is less than 10 °C [80]. Having said that, surface of the platinum rods experienced a temperature higher than sintering temperature of LFP powders because the bed was not well mixed, and consequently, thermocouple temperature reading was not a true representative of the whole bed thermal condition. Thus, the induction heating power supply kept applying more power on the rods.

Therefore, the platinum rods of the IHFBR were removed and the alumina tube of the reactor was replaced with a stainless-steel 316 tube that was suitable for reaction tests below 800 °C. The stainless-steel tube was insulated with a blanket of fiberfrax®. The new configuration of the IHFBR, now being called fluidized bed CVD (FB-CVD) reactor, is illustrated in Figure 3.7.

Rather than heating the internal conductive rods, the induction heating power supply heats up the stainless-steel body of the FB-CVD reactor directly. This method of heating is still very different from external heating methods, e.g. by a tubular furnace. While heating by an external tubular furnace, a considerable amount of heat generated on its heating elements is lost, heat transfer is slow and includes convection heating to the outer surface of reactor, conduction heating within the thickness of the reactor and convection heating from internal surface of the reactor to the bed [1]. Such mechanism may result in internal wall of the reactor with a temperature much hotter than sintering temperature of the LFP bed. Whereas, the FB-CVD not only benefits from fast heating rate of the induction heating mechanism, but also the generated heat is directly transferred from internal surface of the reactor to the bed.

A mass flow controller adjusted flow rate of the fluidizing gas, which was nitrogen during heat-up and propylene during reaction. Using a LabView program, inlet flow rate set point was adjusted to maintain the required gas velocity in the bed. The bed mass was selected so that the bubbling bed height was almost twice the bed diameter.

For each experimental run, the LFP bed was purged with pure nitrogen while the reactor was being heated by induction at a rate of 20 °C/min. Nitrogen flow was to avoid oxidation of the LFP powders and the modest heating rate was to prevent sintering of the LFP powders in contact with wall of the reactor.

Once the bed reached the desired temperature, the nitrogen gas was switched to propylene line. A MKS multi gas FTIR was employed to detect reactor outlet gases: CH_4, C_2H_4, C_2H_6, C_2H_2, C_6H_6 and unconverted C_3H_6.

At the initial 2 to 3 minutes of the tests, some trace amounts of CO_2 and water were also detected in FTIR that could indicate a primary reduction of iron content of the LFP powders (more investigation is required). In order to estimate molar production of the solid carbon by mass balance calculations, a standard tracer (with known flow rate and pressure) was injected to the reactor outlet.

At the end of the coating sequence, the inlet gas was switched to nitrogen and the reactor was cooled down. Once the bed reached near ambient temperature, a cyclonic solid collection system was employed to discharge and collect the coated LFP powders.

Before running a new test, the inlet gas was switched to air and the reactor was heated to the coating reaction temperature following a 5 minutes isothermal condition to burn off the remaining carbon that could have been deposited on the reactor wall.

3.4 Pulse-assisted fluidized bed CVD reactor

As discussed earlier, the as-received P2 LFP samples had a secondary size distribution of 5 to 800 μm. These samples were sieved into several cuts. Initial primary tests were applied on samples with a size distribution of 125 to 250 μm. This size cut had a fluidization behavior similar to Geldart's group B powders.

However, it was desired to run the experiments with LFP powders of a size below 45 μm in order to be as close to their primary size of 50 to 400 nm. However, interparticle forces were severely present in between such LFP powders, so they were very sticky, and we could not fluidize them in the FB-CVD reactor.

We sought for several troubleshooting methods to overcome this issue. Accidentally, it was realized that by putting a finger on the reactor outlet followed by its pull-over, the cohesive LFP bed tended to expand. *Successive repetition of this action led to discover that putting a limit on the reactor outlet flow with an appropriate On/Off frequency, helps overcome the interparticle forces, and consequently, fluidize the cohesive LFB bed.* In fact, upon close action of the valve, the gas phase is pressurized inside the reactor. Subsequently, when the valve opens the

pressurized gas tends to leave the reactor rapidly with a velocity larger than terminal velocity of the agglomerated LFP particles eager to entrain them. A particular advantage of pressurizing the propylene in the LFB is that higher pressure thermodynamically favors production of carbon.

Therefore, a solenoid valve (SV2 in Figure 3.7) was placed in the reactor outlet, and the LabView program was modified to adjust On/Off timing of the solenoid valve, and to automatically control its operation.

Two pressure transducers were employed to optimize frequency of this newly found pulsation technique, and to find the minimum fluidization velocity and gas hold up to do with a given frequency. Even though the solenoid valve SV2 functioned very efficiently, LFP powders used to accommodate inside the valve causing its malfunction. Therefore, it was decided to stop the valve SV2 and put another solenoid valve SV1 between the mass flow controller and the reactor distributor (Figure 3.7).

The solenoid valve SV1 also functioned very well and helped fluidize the cohesive bed of LFP powders. However, its pulsation mechanism was rather different from the solenoid valve SV2. Having the upstream pressure of the gas line at 10 psig, upon open action of the SV1 following its close action, it throws a pressurized gas at ambient temperature towards the gas distributor so that the kinetic energy of the gas gets on the distributor is much higher than in the absence of the SV1 resulting in overcoming the interparticle forces between the cohesive LFP powders. More research is on way to elaborate mechanism of the pulsation.

To characterize fluidization quality supported by the solenoid valve SV1 and to avoid influence of the reactor wall effect, a Plexiglas tube of 3.8 cm diameter and 20 cm long with a gas distributor of 2 microns stainless-steel disk was employed.

Pressure inside the reactor and pressure drop across the bed were measured with two differential pressure transducers. Also, pressure drop after the valve was measured to ensure there was still a flow of the gas into the bed when the valve was closed. In the meantime, frequency of pulsation varied between 3.6 and 4.4 Hz.

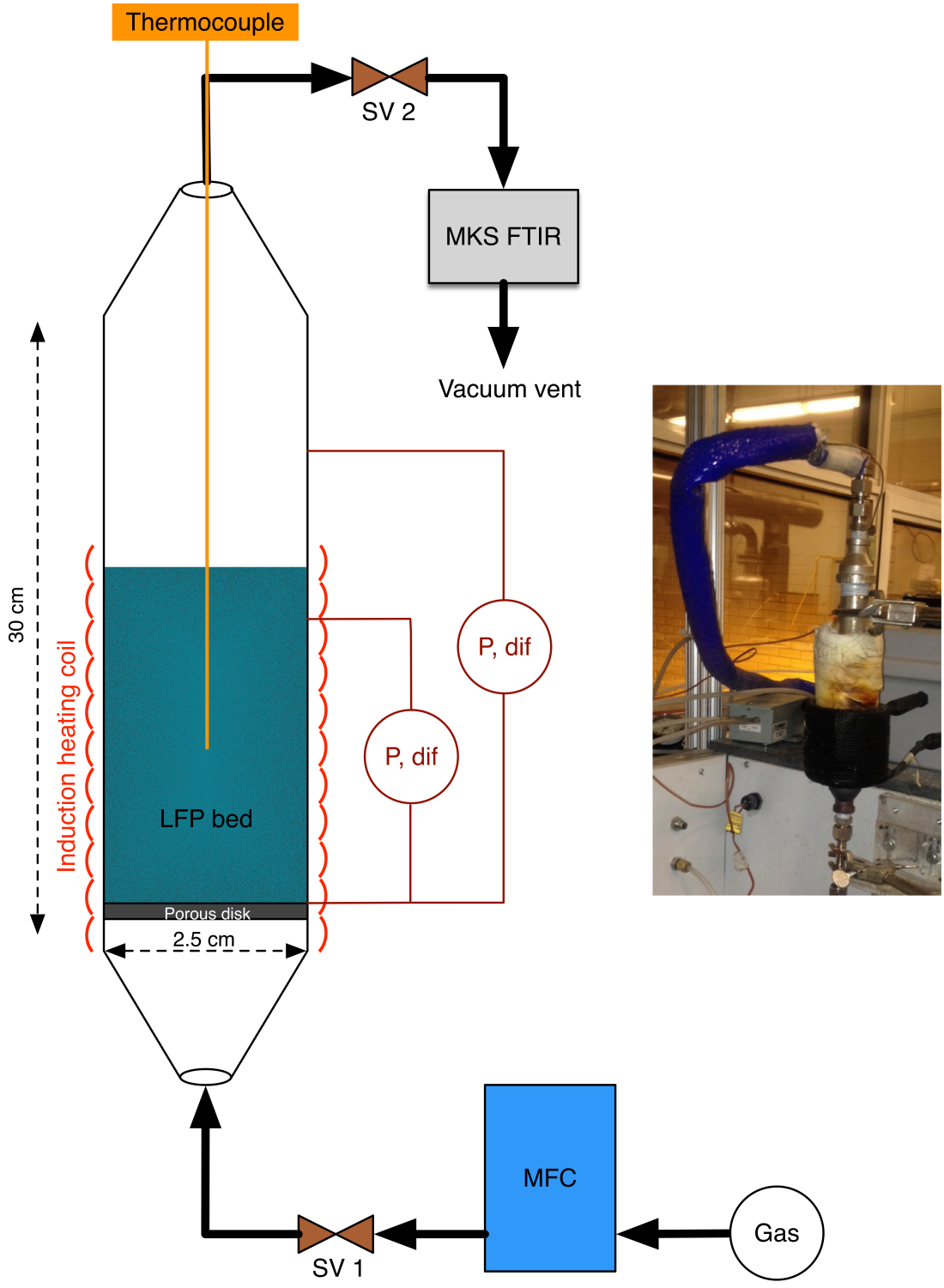

Figure 3.7: Pulse-assisted fluidized bed CVD apparatus

3.5 Characterization techniques

LFP and C-LFP phase purity was analyzed by x-ray diffraction (XRD) using Cu Kα radiation (λ=1.54056 Å). Amount of carbon deposited on the LFP particles were determined by LECO elemental analyzer. The size distribution of primary particles, agglomerates size distribution and morphology of the particles were determined with scanning electron microscopy (SEM). To measure morphology and thickness of the coated layer, we used transmission electron microscopy (TEM). XPS analysis was employed to determine how carbon bonded with LFP by the CVD process. Raman spectroscopy was utilized to derive the sp3/sp2 ratio and sp3 content of the samples.

To measure electrical conductivity of the samples accurately, we used 4-point method. Two rods with high electrical conductivity were placed at the top and bottom of a cylinder to keep the particles in between while electrical current was applied through the rods into the sample (Figure 3.8).

The diagram on Figure 3.9 overviews the main steps of the applied methodologies in this research.

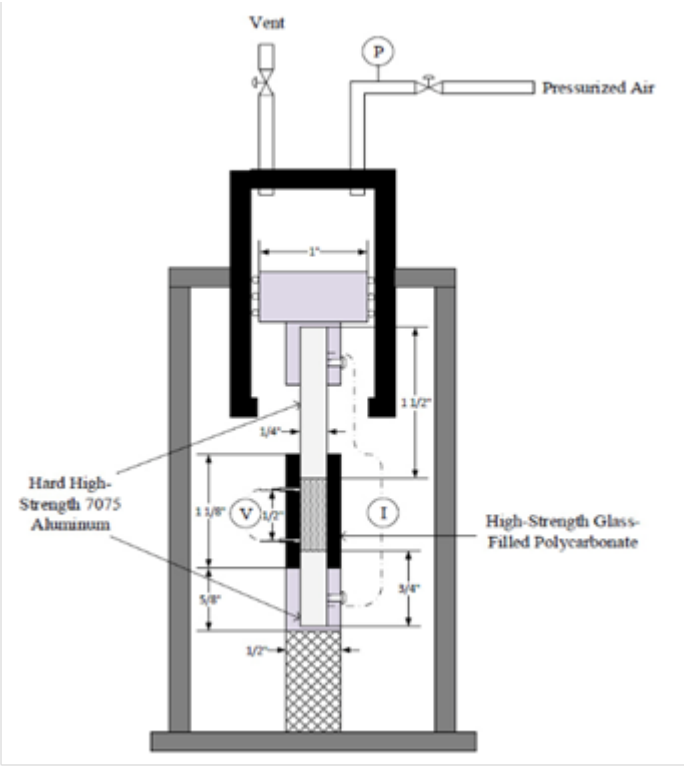

Figure 3.8: Schematic of the device designed and used as conductivity meter

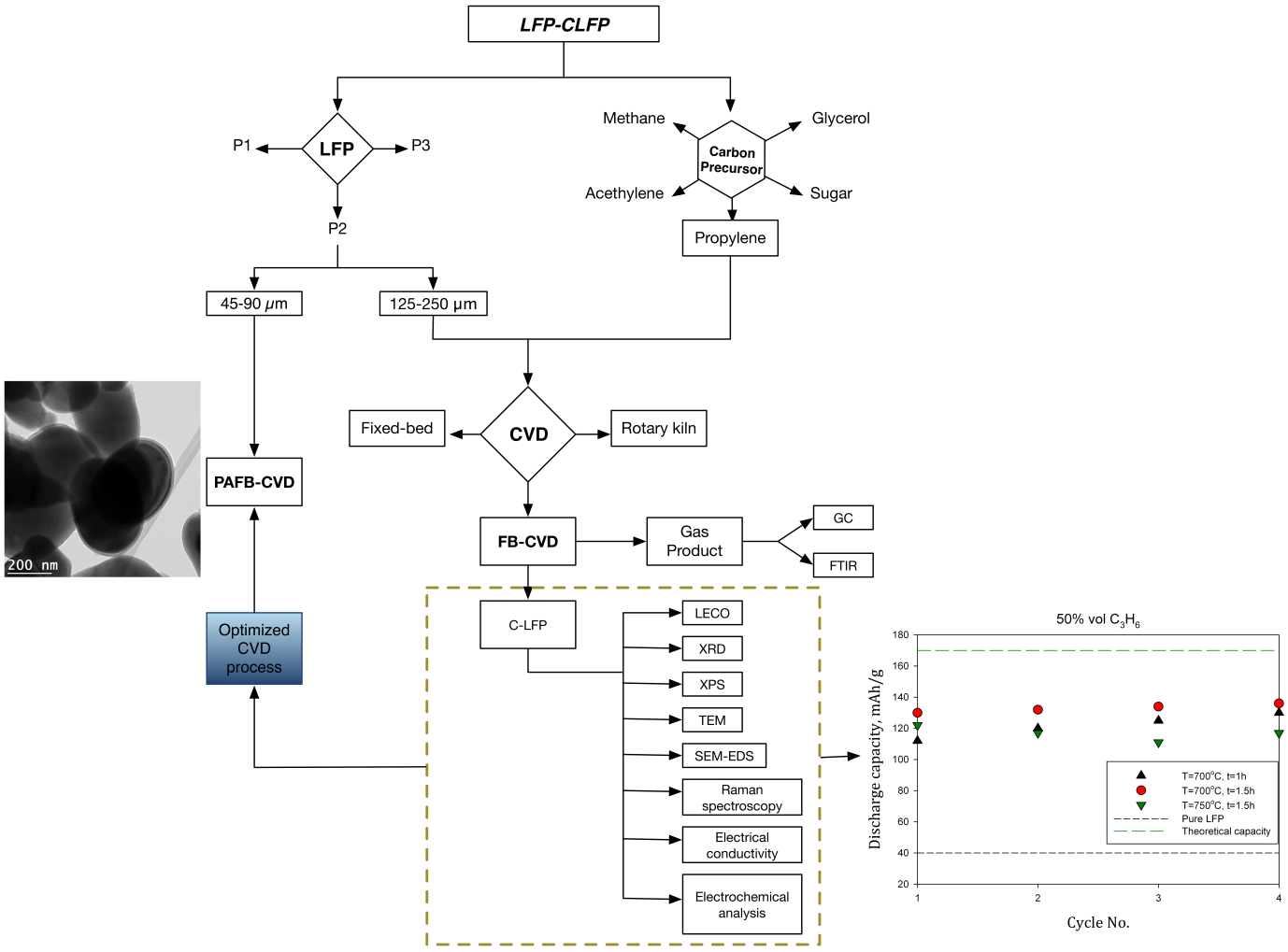

Figure 3.9: An overview of the applied experimental methodologies

CHAPTER 4 RESULTS AND DISCUSSION: FB-CVD

The objective of this chapter is to develop an optimized CVD process for carbon coating of LFP powders in such a way that improves performance of LIBs. To resolve the low electrical conductivity of LFP powders as cathode materials, carbon coating proved to be among the best solutions. Although more amount of carbon results in higher electrical conductivity, there is an optimum range for the amount of carbon (i.e. 1 to 5%wt) to maximize performance of the battery. This is because of two main reasons: firstly, the thickness of carbon more than 3 to 5 nm has barrier effect on Li ion diffusion, and secondly, increasing the amount of carbon reduces the percentage of Li in cathode, which consequently decreases energy density of the battery. In addition to the amount carbon, the form of carbon (i.e. graphene or disordered) and uniformity of coating are the other complicating factors on the performance of the cathode. Moreover, the final product quality depends on quality of gas-solid contact, which is influenced by reactor type and particles size distribution. Therefore, it is extremely difficult to set an optimum condition without considering a precursor and reactor type. Hence, we tried to meet the objective through two steps: firstly selecting an ideal precursor, and secondly optimizing CVD parameters for this precursor. As discussed earlier, propylene was selected as the carbon precursor of this research. To avoid effect of interparticle forces that is severely present in between very find secondary LFP powders, Geldart's group A of secondary LFP powders were initially investigated.

4.1 Optimizing CVD parameters for carbon coating of LFP

To optimize the CVD process, following parameters were considered:

- Type of reactor (i.e. fixed bed and fluidized bed)
- Reaction time
- Gas velocity in fluidized bed (associated with gas residence time)
- Propylene concentration
- Temperature
- Catalytic effect of LFP

To investigate effects of these parameters, practical ranges of the parameters were considered and presented in Table 4.1. These ranges were selected based on some primary screening tests. Before

studying the effects of the parameters on quality of the products, a brief description about mechanism of propylene decomposition is presented as follows.

Table 4.1: Design of experiments

	Test#	LFP mass, g	Propylene, mol%	Temperature, °C	Time, h	Gas velocity, cm/s
Fixed bed	1	6	3	700	3	1
	2				9	
	3				15	
FB-CVD	4	6	3	700	3	1.5
	5					4.8
	6					9.7
	7					14.5
	8				9	1.5
	9					4.8
	10					9.7
	11					14.5
	12				15	1.5
	13					4.8
	14					9.7
	15					14.5
FB-CVD	16	6	3	750	3	9.7
	17				15	
	18				9	14.5
	19					
FB-CVD	20	6	50	700	0.5	9.7
	21				1	
	22				1.5	
FB-CVD	23	6	50	750	0.5	9.7
	24				1	
	25				1.5	
FB-CVD: mass of LFP and Sand	26	4	3	700	3	9.7
	27	Sand				

4.1.2 Pathways of carbon deposition during propylene decomposition

Carbon deposition from propylene pyrolysis includes homogeneous and heterogeneous reactions such as chemical reaction in the gas-phase, chemisorption and desorption including sequential and competing reactions. For instance, as shown in Figure 4.1 several hydrocarbons and radicals of C_2H_x, C_4H_y and C_6H_z in the form of chain and cyclohydrocarbons, are generated during propylene pyrolysis so that each of them is a potential source of pyrocarbon (C_∞). Therefore, the sources of the deposited carbon on the surface of LFP powders could be either directly from the pyrocarbon due to cracking of propylene or from the pyrocarbons due to further cracking of the generated radicals.

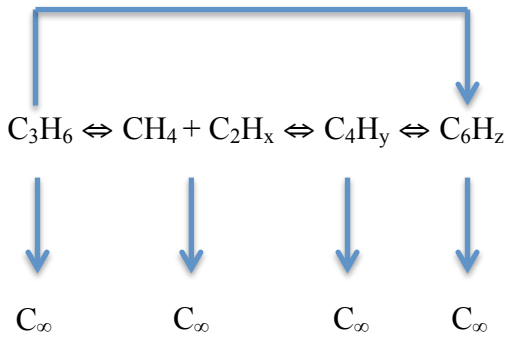

Figure 4.1: Pathways of pyrocarbon production during propylene pyrolysis

4.1.3 Effect of reactor type

Experiments No. 1 to 3 were carried out in a fixed bed reactor condition to study the effect of configuration of reactor (i.e. gas-solid contact) on uniformity of coating. In addition, since non-assisted fluidization of nano-particles (i.e. Geldart's group C particles) show similar characteristics as fixed beds, these tests could show a meaningful insight about the challenges for optimizing the CVD process when using Geldart's group C particles in a fluidized bed reactor.

In general, in fixed bed reactors, solid mixing and gas-solid contact are poor in comparison to fluidized bed reactors. Consequently, the results showed that the coating was extremely non-uniform in such a way that the particles close to the distributor were coated while particles at top

region of the bed stayed uncoated. Another source of non-uniformity of coating comes from the fact that temperature profile in the bed was not uniform. In other words, particles close to the wall had more coating layer than the ones in the core, due to the fact that the reactor was heated through its wall. Furthermore, a severe sintering of C-LFP particles were observed using the CVD process through the fixed bed reactor as presented in Figure 4.2. These sintering defects are consequences of non-uniform temperature profile in the bed and more importantly long idle time of particles in the fixed bed that caused the softened particles to tend to agglomerate.

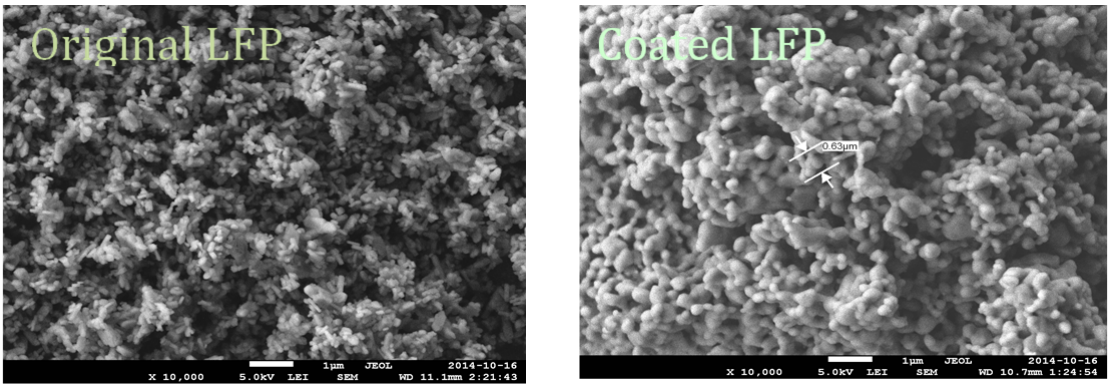

(a) (b)

Figure 4.2: SEM image of (a) fresh LFP and (b) C-LFP produced by fixed bed reactor at 700°C

Considering poor quality of products, it is concluded that a fixed bed is not an appropriate reactor for the CVD process. In addition, one can conclude that using Geldart's group C particles in a non-assisted fluidized bed is not an accurate approach to optimize the CVD process. This is because the hydrodynamics (i.e. quality of solid mixing and gas-solid contact) will have a significant role in the quality of final products. Therefore, to address the objective of this chapter, LFP particles with a size distribution of 125-250 μm, which belong to Geldart's group A classification and have a decent fluidization quality, were employed in the experiments of this chapter.

4.1.4 Effect of CVD operating conditions on kinetics of carbon deposition

Experiments No. 4 to 15 were designed to study the effects of reaction time and gas velocity on carbon coating by the developed FB-CVD setup.

Figure 4.3a shows variation of the carbon content derived from LECO analysis for these experiments using the 3mol% propylene mixture. It clearly shows that mass fraction of the coated carbon increases by increasing the reaction time. However, the rate of this increase depends on the gas velocity and reaction time itself. At low gas velocities, i.e. 1.5 and 4.8 cm/s, the carbon content increased proportional to elongation of reaction time. However, at higher gas velocities, i.e. 9.7 and 14.5 cm/s, mass of deposited carbon at reaction times shorter than 9 hours increased as opposed to longer reaction times. This could be due to attrition of deposited carbon layer over C-LFP particles. TEM images (Figure 4.4) of C-LFP, which was produced in these conditions, confirm the hypothesis. Particularly, Figure 4.4a explains how the deposited carbon was peeled off due to the attrition.

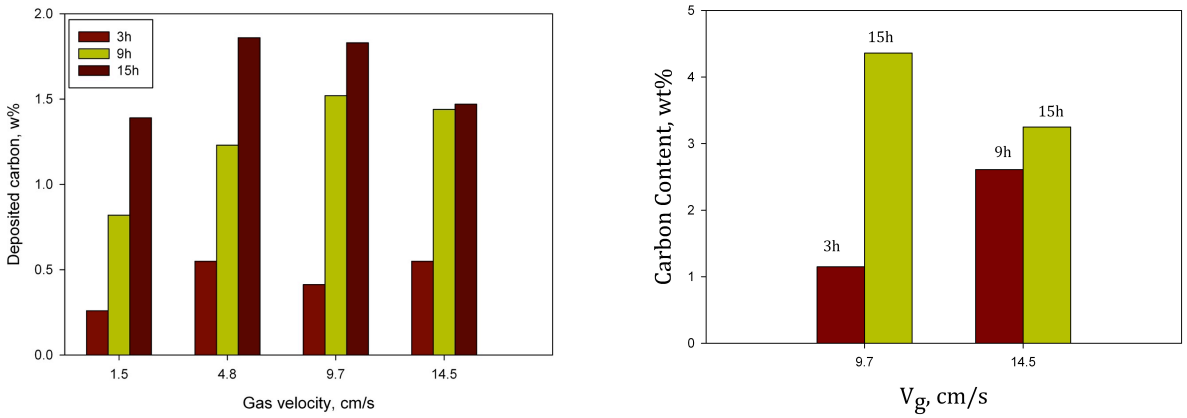

Figure 4.3: Variation of carbon content of C-LFP, derived from 3% Propylene, based on reaction time and gas velocity at (a) 700 °C and (b) 750 °C

The other factor of interest from experiments No. 4 to 15 concerns effect of gas velocity. In general, gas velocity can influence the carbon deposition process by effecting three main parameters, namely, gas residence time, gas-solid contact quality and mass transfer coefficient from gas to solid. An increase in the gas velocity decreases the former parameter, which undermine the carbon deposition, while increases the two later parameters, which strength the carbon deposition.

Figure 4.3a reveals that increasing the gas velocity increases the carbon content. However, there is an optimum gas velocity where carbon content reaches its highest amount, and increasing the gas velocity beyond this point has a reverse effect. This can be described by the fact that at low gas velocities, the effects of increase in gas-solid contact quality and mass transfer coefficient overcomes the effect of reduction in gas residence time in proceeding the carbon deposition. However, after a certain point further increase in the gas velocity makes the decrease in gas residence time becomes dominant and undermines the carbon deposition.

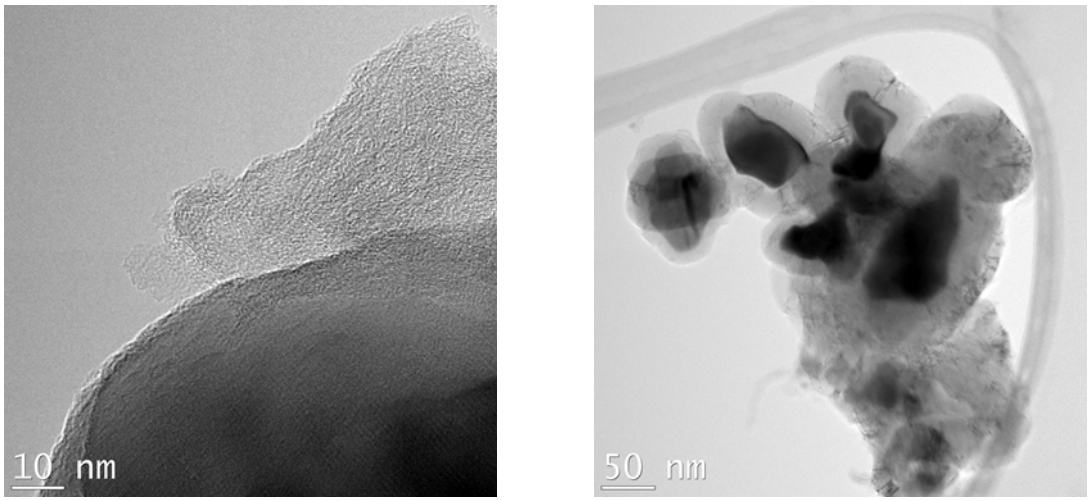

(a) (b)

Figure 4.4: TEM images of produced C-LFP by 3% propylene with gas velocity of (a) Vg=14cm/s and (b) Vg=9.7 cm/s at 700°C

The main reason to use such a low concentration propylene mixture (i.e. 3%) was related to study the effect of precursor concertation and some safety concern about using combustible gas in the lab. However, the amount of deposited carbon was not considerable even after 15 hours of reaction time. To overcome this problem, the reaction temperature was increased to 750 °C, just below the sintering temperature of LFP particles, during the experiments No. 16 to 19.

Figure 4.3b presents the carbon content of results for these experiments. Regarding the trend and variation of the amount of deposited carbon based on reaction time and gas velocity, one can make similar discussion as the one of 700 °C.

A comparison between the results of the experiments (i.e. between

Figure 4.3a and b) shows that the amount of deposited carbon was increased by about two times when the reaction temperature was increased from 700 to 750 °C. Therefore, in term of amount of deposited carbon, the products of the CVD process using 3% propylene at 750°C were in line with the optimum amount that has been reported in the literatures, i.e. 1 to 5%. However, to reach the lower limit of the optimum range, it is required to operate the reaction for at least 3 hours. Moreover, as mentioned before, beside the carbon content there are several other parameters that should be optimized for producing a successful cathode material. For instance, particle size should stay almost unchanged for having reasonable Li ion diffusivity. This means that the sintering of LFP particles should be avoided during the CVD process. However, SEM images of produced C-LFP at 750 °C, i.e. experiment No. 19, reveals that the particles were severely sintered, Figure 4.5 in micro scale. This is mainly because of relatively long reaction time rather than idle time since the gas velocity was set at 14.7 cm/s during this experiment. Considering these observations, a mixture with higher propylene percentage, i.e. 50 mol%), was used as the carbon precursor afterwards.

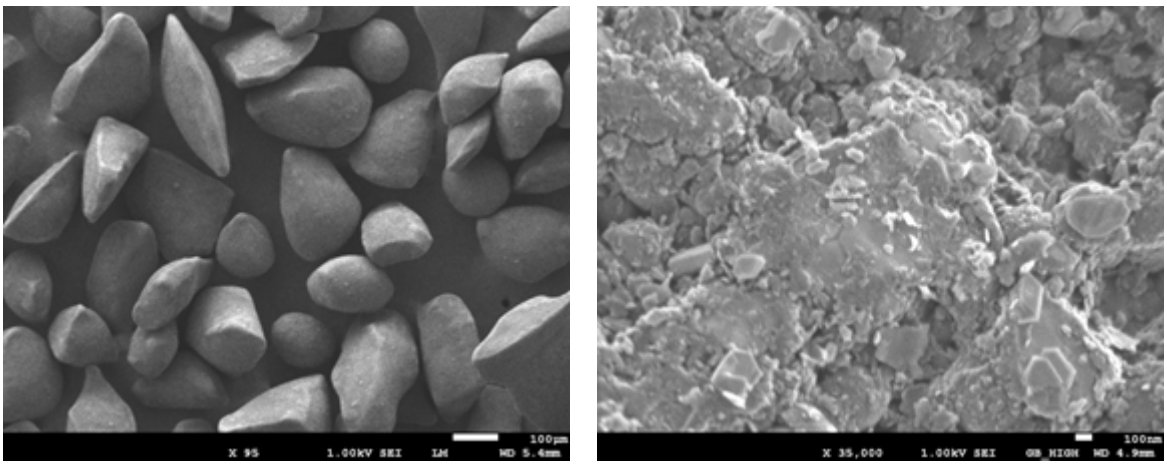

(a) (b)

Figure 4.5: SEM image of C-LFP produced by 3% propylene with gas velocity of 14.7 cm/s at 750°C at micro and nano scales

Figure 4.6 shows variation of the carbon content, measured by LECO, based on the temperature and reaction time of the CVD process using the 50 mol% propylene mixture at gas velocity of 9.7 cm/s from experiments No. 20 to 25. These experiments were carried out at much lower reaction time, i.e. 0.5, 1 and 1.5 hours, in comparison with one of 3 mol% propylene. However, the amount of deposited carbon was in line with the optimum range, particularly after only 1 hour of reaction time even at 700°C. This is mainly due to increase in availability of the precursor and subsequently increase in the precursor-LFP contact when using a mixture with higher propylene concentration. Thus, gas concentration can influence on the cost of the process. Also, the time duration of the CVD process is an important factor because the chance of forming carbon clusters and sintering of LFP particles are increased in a longer reaction, which is not favorable. Figure 4.6 shows that the amount of deposited carbon on LFP particles increases at elevated temperatures. However, this increase is not as much as the one of 3 mol% propylene. In addition, by increasing the time of the coating process, more amount of carbon will be deposited on the surface of the particles.

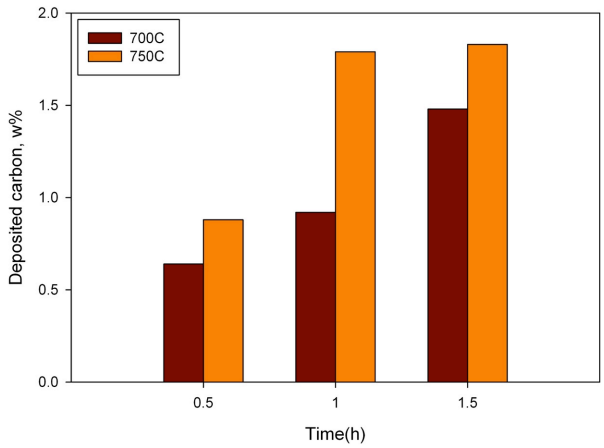

Figure 4.6: Carbon content of C-LFP produced by 50% propylene at 700 and 750°C for different reaction times

Moreover, according to the TEM images of different samples coated at 700 °C and 750 °C, we realized that since at 750 °C some particles might be sintered, carbon is not deposited uniformly onto surface of individual particles. In Figure 4.7, Correspondingly, some clusters of carbon

between LFP particles occurred at 750 °C are noteworthy with respect to quality of coating at 700 °C.

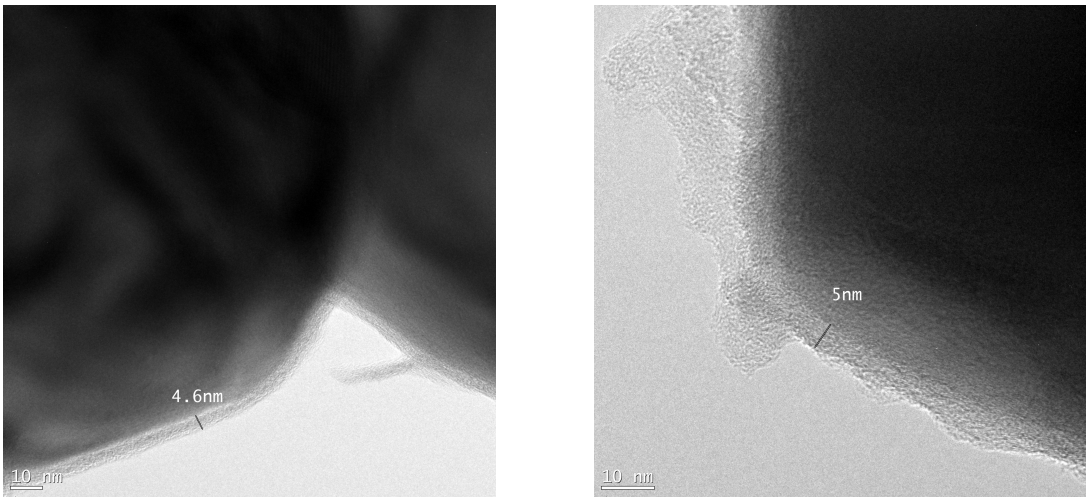

(a) (b)

Figure 4.7: TEM images from coated LFP samples obtained from 50 % propylene during 90 min: morphology of the particles and layer of coated carbon (a) 700 °C and (b) at 750°C

4.1.5 Conversion of propylene under CVD conditions

Evolution of product gases was recorded by a MKS multi gas FTIR during pyrolysis reactions of propylene with initial concentration of 3 mol% at 700°C. Gases such as CH_4, C_2H_4, C_2H_2, C_3H_6 and C_6H_6 were the main detectable gases. Interestingly, evolution of benzene was significantly higher that other gases that were produced during pyrolysis. However, conversion of propylene was significantly low under applied CVD conditions; i.e. less than 15%. As depicted in Figure 4.8 from a 15 h test, at higher gas velocities, corresponding to shorter gas residence time, there was not time for pyrolysis reactions to progress; for instance, a conversion of 1% was obtained for a gas velocity of 14.5 cm/s (Table 4.2). The effect of gas velocity on the conversion of propylene at 700°C is presented in Table 4.2. An increase in the gas velocity decreased propylene conversion due to reduction of the gas residence time.

Concentration of product gases from FTIR in the reactor outlet was taken to estimate rate of carbon production. Unfortunately, estimated total gas yields were more than 100% that resulted in negative values for estimated rate of carbon deposition (Table 4.2). This is mainly due to very

low conversion of propylene and also due to low rate of carbon production, that could be in the order of magnitude of micro-gram/min rather than g /min, so that accuracy of FTIR data acquisition was not high enough. Oscillation of conversion data in a range of ± 3% confirms this hypothesis.

Table 4.2: Conversion of propylene versus gas velocity

Effect of mass balance: T= 700°C, Time= 15h			
Vg, cm/s	C_3H_6 conv., %	Carbon, g/min	Total gas yield (mass basis), %
14.5	0.95	-2.16	104.98
9.7	1.88	-1.73	103.02
4.8	3.19	-1.26	102.9
1.5	12.76	2.17	94.99

We realized that LFP powders had catalytic effect on conversion of propylene during pyrolysis reactions. For instance, FTIR data of Figure 4.8 illustrates that at all tested gas velocities, Initial conversion of propylene was relatively high, but it tended to decline during the reaction and reached a plateau after a period of 3 h.

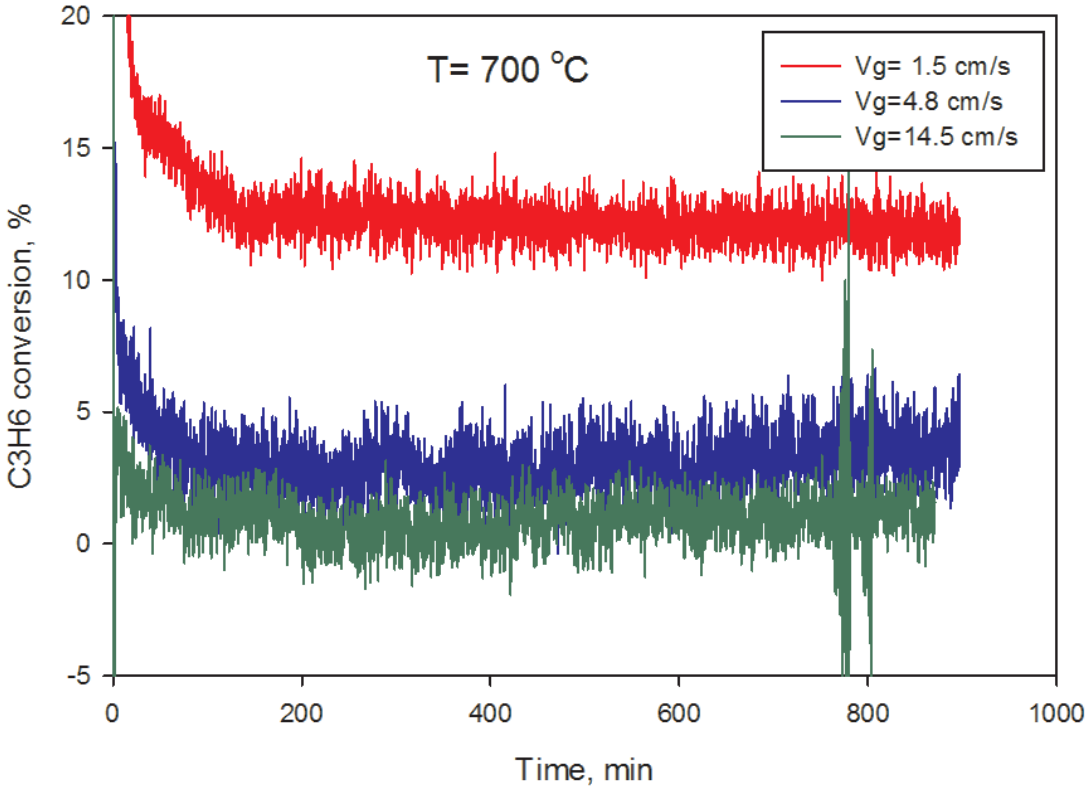

Figure 4.8: FTIR data on conversion of 3% propylene mixture at 700°C

In order for further investigation, propylene pyrolysis was applied at three different fluidized beds of 6 g sand, 4 and 6 g LFP for a given gas velocity of 9.7 cm/s at 700°C (i.e. experiments number 14, 26 and 27). As presented in Table 4.3, conversion of propylene in the bed of inert material, i.e. sand, was lower than the one of the LFP even with lower mass. For example, propylene conversion for the bed of 6 g sand was 0.75 % while this was 1.28 % for the bed of 4 g LFP powders. Correspondingly, Larger mass of LFP in the fluidized bed resulted in higher propylene conversion. Considering these observation, one can conclude catalytic effect of the LFP particles on the conversion of propylene.

Catalytic effect of LFP powders can be attributed to presence of iron on their surface. The decline of propylene conversion in Figure 4.8 explains that during deposition of carbon on the surface of LFP powders, iron is being hidden and it is not available on the surface after a while to help

cracking the propylene molecules. The plateau trend of propylene conversion in Figure 4.8 indicates that propylene cracking occurred thermally in the absence of iron as opposed to catalytic cracking.

Table 4.3 Catalytic effect of LFP powders on propylene conversion

Effect of mass balance: T= 700°C, Vg= 9.7 cm/s			
Bed	C_3H_6 conv., %	Carbon, g/min	Total gas yield (mass basis), %
Sand- 6g	0.75	-2.17	105.01
LFP-4g	1.28	-1.76	104.45
LFP-6g	1.91	-1.59	104.08

The other way to evaluate the catalytic effect of LFP on propylene cracking is to compare the mass of deposited carbon on the beds of LFP and sand. The bed of sand contained only 0.018 wt% carbon versus 0.418 wt% of the bed of LFP. This confirm the catalytic effect of the LFP particles for hydrocarbon cracking, due to the presence of iron in the molecular structure. Additionally, iron has a catalytic role for graphitic carbon fabrication, which explains the layered structure of graphite on the LFP particles in the TEM images (e.g. Figure 4.7).

Even though conversion of propylene was quite low in one pass through the fluidized bed, we propose to design a circulating fluidized bed reactor where unconverted propylene and the product gases can return to the bed until desired layer of carbon is coated on the surface of LFP powders. Such a design would help reduce OPEX of the process dramatically as less amount of propylene might be consumed and shorter reaction time would be required.

4.2 Characterization of the produced C-LFP by FB-CVD

Beside the carbon content, there are several critical parameters in the coating of LFP particles that can influence performance of final products as cathode material for LIB applications. Some examples of these parameters are impurity and change in crystallinity which introduced during the coating process, morphology of deposited carbon, how carbon is binding to the surface of

LFP particles, electrical conductivity of C-LFP and type of carbon (i.e. graphite or disordered). In this section, we will evaluate the mentioned parameters respectively as follows.

4.2.1 Impurity and change in crystallinity

To evaluate impurity and any change in the crystallinity on the surface of produced C-LFP particles, the X-ray diffraction (XRD) was utilized. Figure 4.9 shows XRD patterns of LFP olivine before and after the carbon coating process that were obtained from a philips X'Pert PRO MRD diffractometer at room temperature. The measurement was recorded under Bragg-Bretano geometry at 2θ steps of 0.02° and 2 sec/step counting time. According to XRD data, there was no evidence of post-reaction impurity after coating at 700 °C for 30 minutes because similar peaks associated with fresh LFP and C-LFP eluted; that is, no reduction of iron occurred.

Elaboration of XRD signals, however, revealed that the peak of Li_3PO_4 (refined cell: a = 6.01890, b = 6.12, and c = 4.2966 Å), which is considered as an impurity in the LFP structure, eluted from both LFP and C-LFP samples. In other words, the as-received LFP sample did not have the idea specifications. Presence of such an impurity has detrimental effect on electrochemical properties of C-LFP powders.

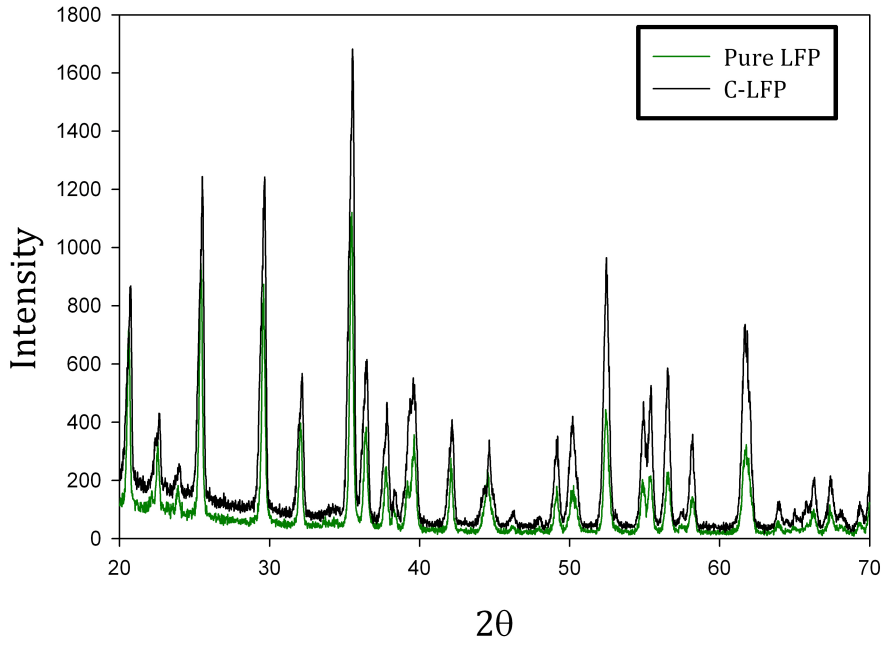

Figure 4.9: XRD patterns of uncoated LFP and C- LFP obtained at 700 °C during 30 min

Additionally, the widths of the dominant peaks in both coated and pure LFP were almost the same. In fact, according to Scherrer's low, the size of the crystallite could be estimated as below:

$$dc = \frac{k\lambda}{\beta \cos\theta} \qquad \text{Equation 8}$$

where dc is the crystallite size, λ is the wavelength by which XRD was performed (1.54 A°), β is the peak width, and k is the scherrer constant. The k is a dimensionless shape factor that varies with actual shape of the crystallite. Therefore, it was concluded that the FB-CVD process had no effect on crystallinity of the LFP powders. The only difference between the patterns of the fresh and coated LFP was the intensity of the dominated peaks which was normal.

Fe_2P is a probable product of LFP exhibition to the reductant agent. The associated peaks of Fe_2P are expected at 2θ = 40 and 44. Having said that, there was no evidence of presence of Fe_2P. It should be noted that XRD cannot detect the impurities or nano-sized clusters with concentrations lower than 1% [26], so maybe some Fe_2P with a very low and undetectable concentration was formed. Generally, Fe_2P is desired at very low concentrations.

4.2.2 Morphology of deposited carbon

To study morphology of the produced C-LFP powders, SEM and TEM analyses were considered. The micromorphology of the LFP particles accompanying the shape of the deposited layers of carbon are reported in Figure 4.10 and Figure 4.11.

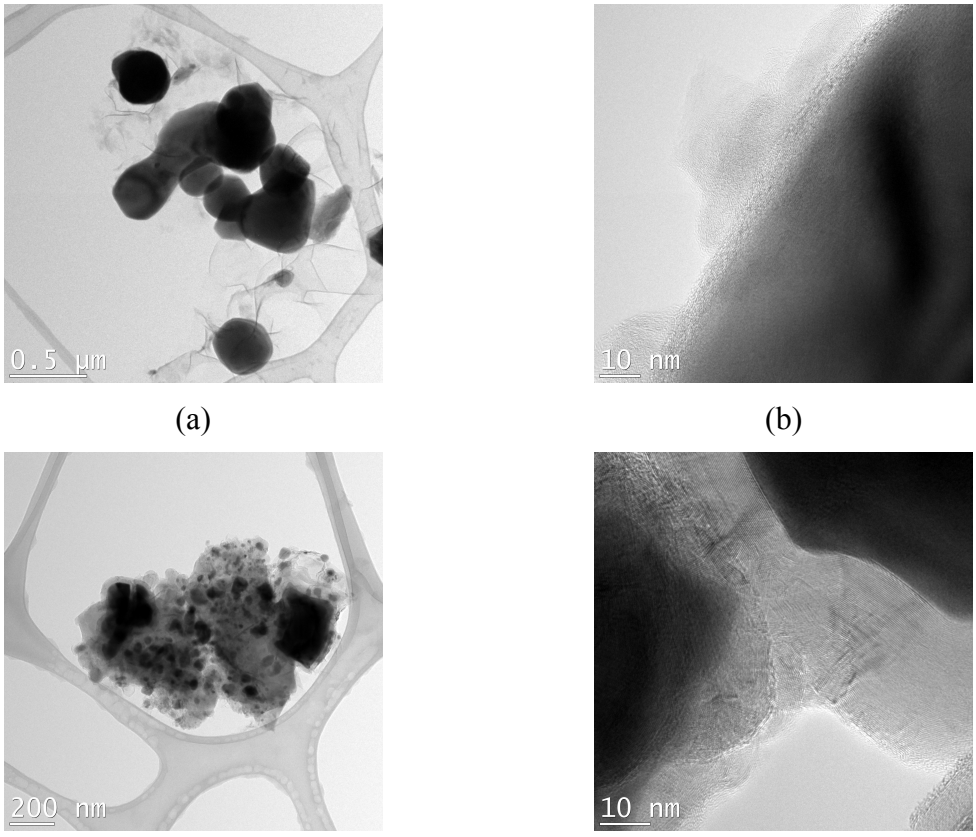

Figure 4.10: TEM images of the produced C-LFP by 3% propylene for 15 h reaction time at (a)-(b) 700°C and (c)-(d) 750°C

Figure 4.10 shows the quality of coating in terms of deposited layer thickness (b and d) and shape of the clusters of C-LFP (a and c). Comparing the images of the C-LFP (Figure 4.10 a-c), C-LFP particles were not sintered at 700°C, while the coating process at higher temperature of 750°C caused sintering, and consequently enlarged secondary particle sizes.

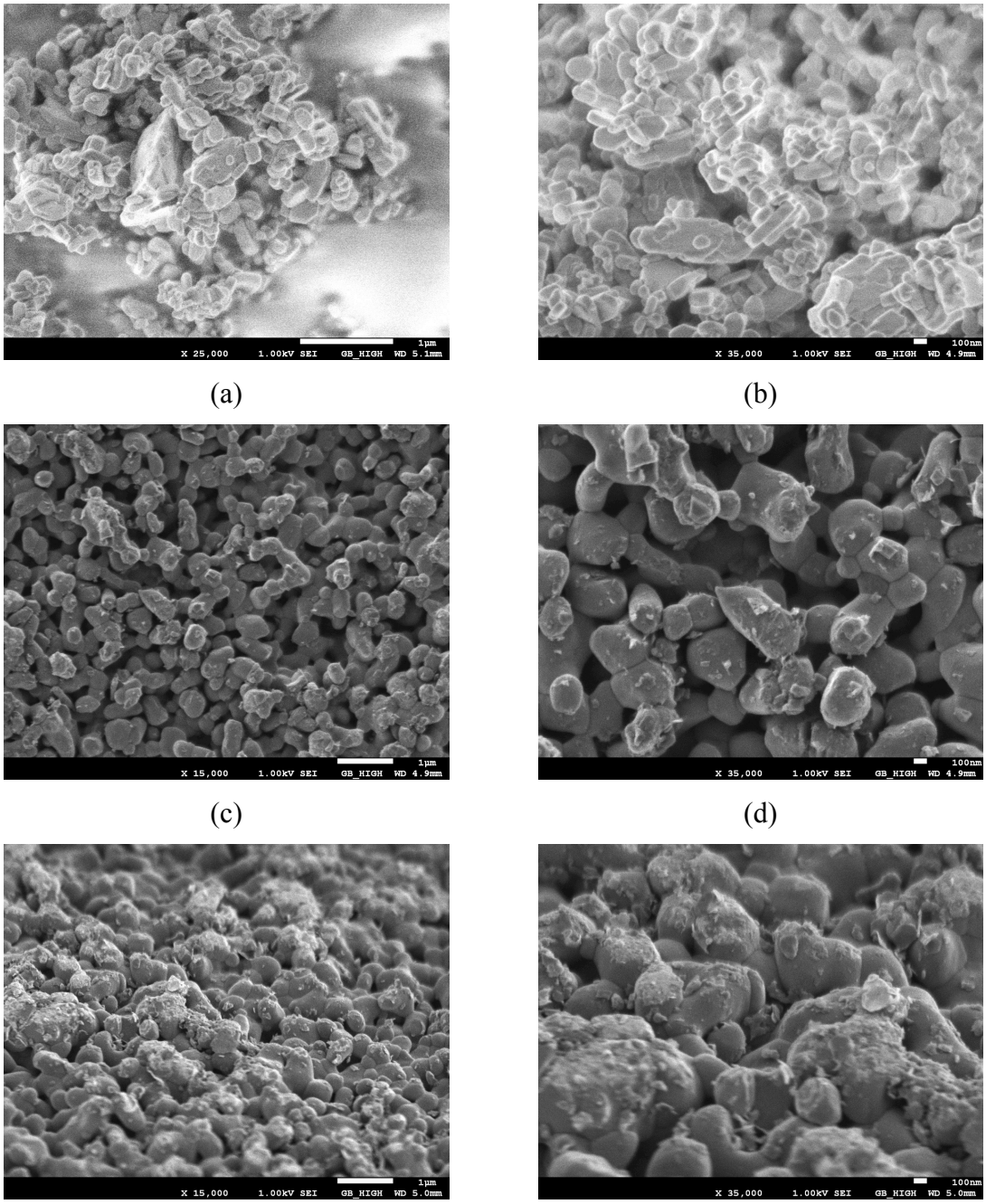

Figure 4.11: SEM images of (a)-(b) pure LFP, the produced C-LFP by 50% propylene with 1.5h reaction time at (c)-(d) 700°C and (e)-(f) 750°C

Figure 4.11 shows SEM images of pure LFP and the produced C-LFP. Figure 4.11a and b corresponds to the pure LFP powders indicating particle size and morphology of the sample.

However, since electrical conductivity of pure LFP is very low (i.e. 10^{-9} S/cm), the associated SEM image quality was not as decent as the one of the C-LFP (i.e. Figure 4.11c-f). Difference in quality of the images of coated and uncoated materials is related to the charge effect. During SEM analysis, specimen is irradiated with electron beam. In case of non-conducting material, static electron charges accumulate on the specimen surface and charging effect arisen. Figure 4.12a and b illustrate this effect on LFP particles. One way to eliminate charge effect is to coat the material with a conductive layer. Therefore, we could comprehend from SEM analysis that carbon covered all the surface of the particles since the C-LFP's images (i.e. Figure 4.11c-f) did not impress any charge effect.

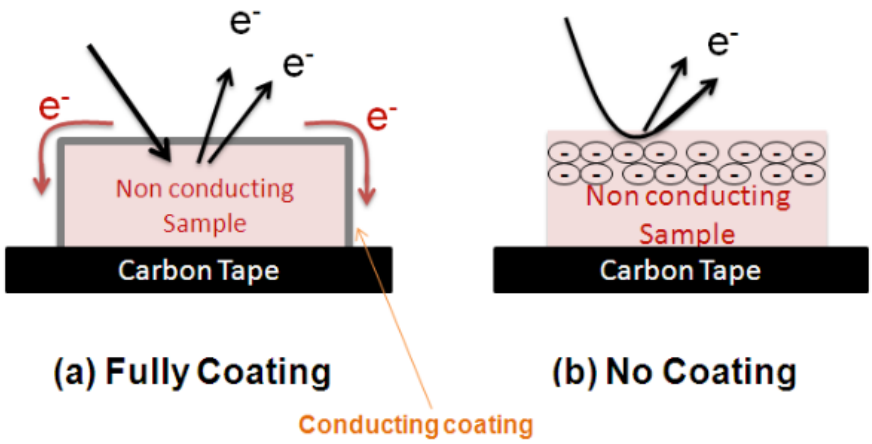

Figure 4.12 Schematic illustration of secondary electron emission during SEM analysis of specimen coated with (a) conductive material and (b) non-conductive material [81]

According to the SEM images of C-LFP powders (Figure 4.11c-f), carbon coating had no effect on the mean particle size of the powders treated at 700 °C. On the other hand, the applied CVD process at higher temperature of 750 °C resulted in sintering, and consequently coherency of the primary particles that led to growth of the secondary particle sizes. Moreover, it can be observed that carbon was accumulated on some areas, which diminished quality of C-LFP. Negative impact of excess amount of carbon on the electrochemical properties of the C-LFP powders will be discussed in the following sections.

Besides having to run at much shorter reaction times, SEM images also confirm that propylene with a higher concentration was preferable as carbon uniformity on the C-LFP powders was more

satisfactory. In addition, although propylene conversion at 700 °C was less than that at 750 °C, quality of coated layer of carbon was superior at this temperature.

4.2.3 Carbon binding

XPS analysis was utilized to determine how carbon bonded to LFP on C-LFP powders as in comparison with fresh LFP. Table 4.4 and Table 4.5 present survey and high resolution scans of the fresh LFP and two C-LFP samples produced at 700 and 750 °C during 30 minute CVD tests. Also, XPS spectra of the pure LFP and C-LFP are presented in Figure 4.13 and Figure 4.14. Since the average analysis depth in XPS is 5 nm, we selected C-LFP samples with the lowest mass of carbon.

Table 4.4 Identification and quantification of elements from survey scan

Name	**B.E.**	**SF**	**At.%**		
			Pure LFP	C-LFP T=700C	C-LFP T=750C
P2p	133.2	0.390	12.2	8.3	9.1
C1s	285.0	0.250	11.6	35.8	30.3
O1s	531.0	0.660	67.8	51.1	55.1
Fe2p3/2	710.9	2.000	8.4	4.7	5.5

Table 4.5 Identification of the chemical bonding from high-resolution scan

Name	**B.E.**	**Identification**	**Relative atomic%**		
			Pure LFP	C-LFP (T=700°C)	C-LFP (T=750°C)
P2p3/2	133.6	$-PO_4$	10.9	7.6	8.1
C1s	284.7	C=C	-	20.4	20.5
	285.0	C-C	7	-	-
	286.5	C-O	2.4	8	3.8
	288.0	C=O	0.8	3.6	2.2
	289.3	O-C=O	1.2	-	-
	289.9	$R-CO_3$	-	3.3	1.7
	291.4	$\pi \rightarrow \pi^*$ of C=C	-	0.8	0.3
O1s	531.6	$-PO_4$, C-O, C=O	67.3	48.1	56.3
	533.9	C-O	-	2.9	-
Fe2p3/2	710.9	$Fe^{2+}(LiFePO_4)$	7.9	3.8	5.5
	714.7		2.6	1.4	1.7

Lithium cannot be detected in XPS spectra since it has only one Li1s peak whose binding energy overlaps with binding energy of Fe3p that has a much larger intensity.

According to XPS data, carbon did not bind to Li or Fe in the C-LFP samples. Direct bonding of carbon to Li or Fe should yield a C1s component at a binding energy lower than that of sp2, in the range of BE = 281 to 284 eV, which was not observed.

Carbon could be bonded to the PO_4 group via binding with the P or one of the O atoms. If carbon bonded directly to P, a C1s component would be expected in a binding energy range from 284.5 to 285 eV; however, it was not distinguished from the sp2 carbon. If carbon bonded to the PO_4 grounp via binding to the oxygen atom as C-O-P, then a C1s component would be expected at a binding energy around 286.5 eV. Such a bond was present in all three samples, i.e. uncoated LFP and C-LFP, but this is normal observation to do with hydrocarbon contamination of samples having been exposed to air.

No significant differences were observed between the Fe2p3/2, O1s and P2p peaks of fresh LFP and C-LFP samples.

The major difference between fresh LFP and C-LFP samples was associated with presence of a C1s bond at binding energy of 289.9 eV on the C-LFP samples, as opposed to fresh LFP, that apparently corresponded to presence of carbonates. Also, at binding energy of 291.4eV, carbon deposited partially on C-LFP samples that belonged to sp2 carbon group.

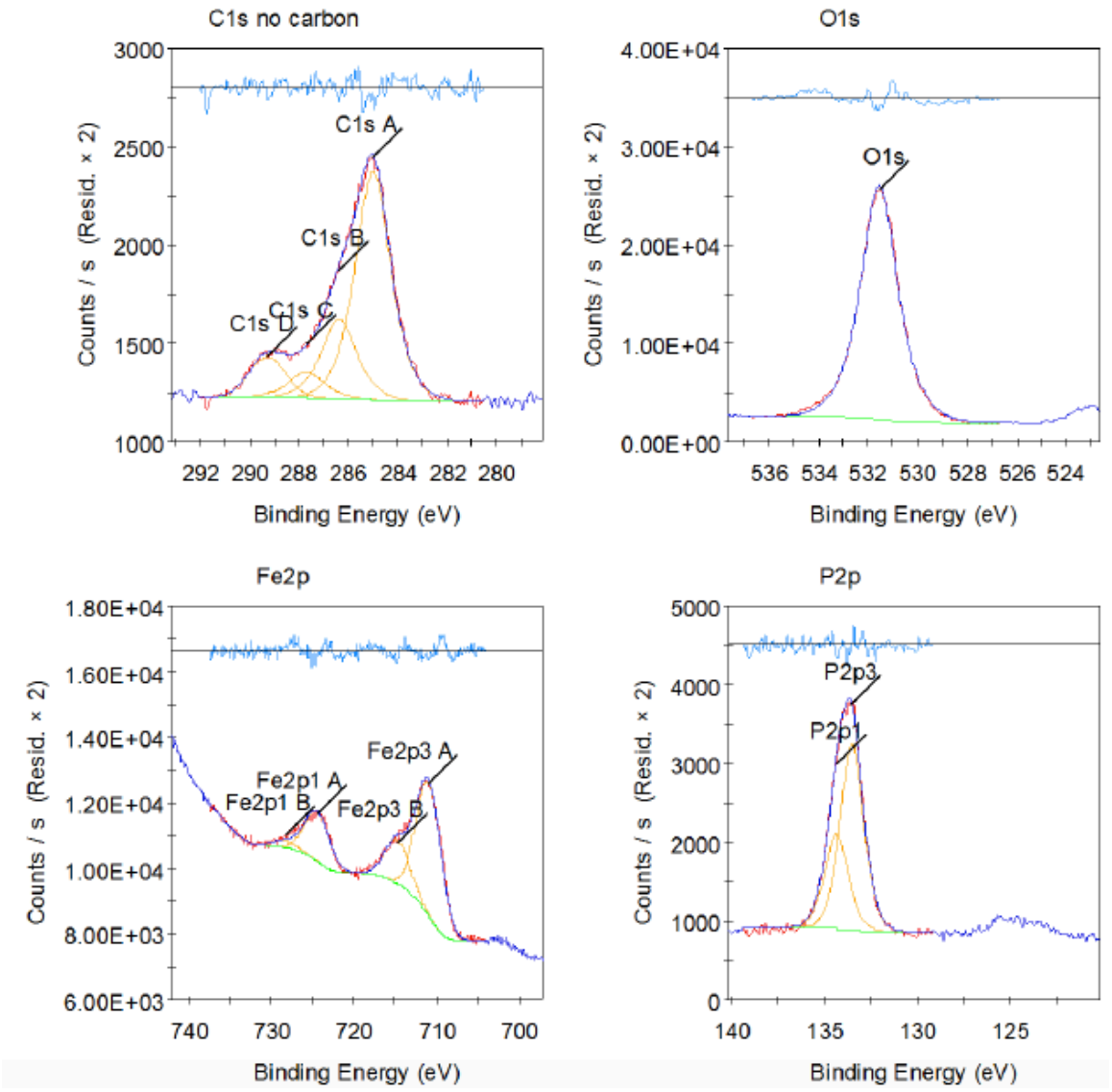

Figure 4.13: XPS spectra of the pure LFP sample

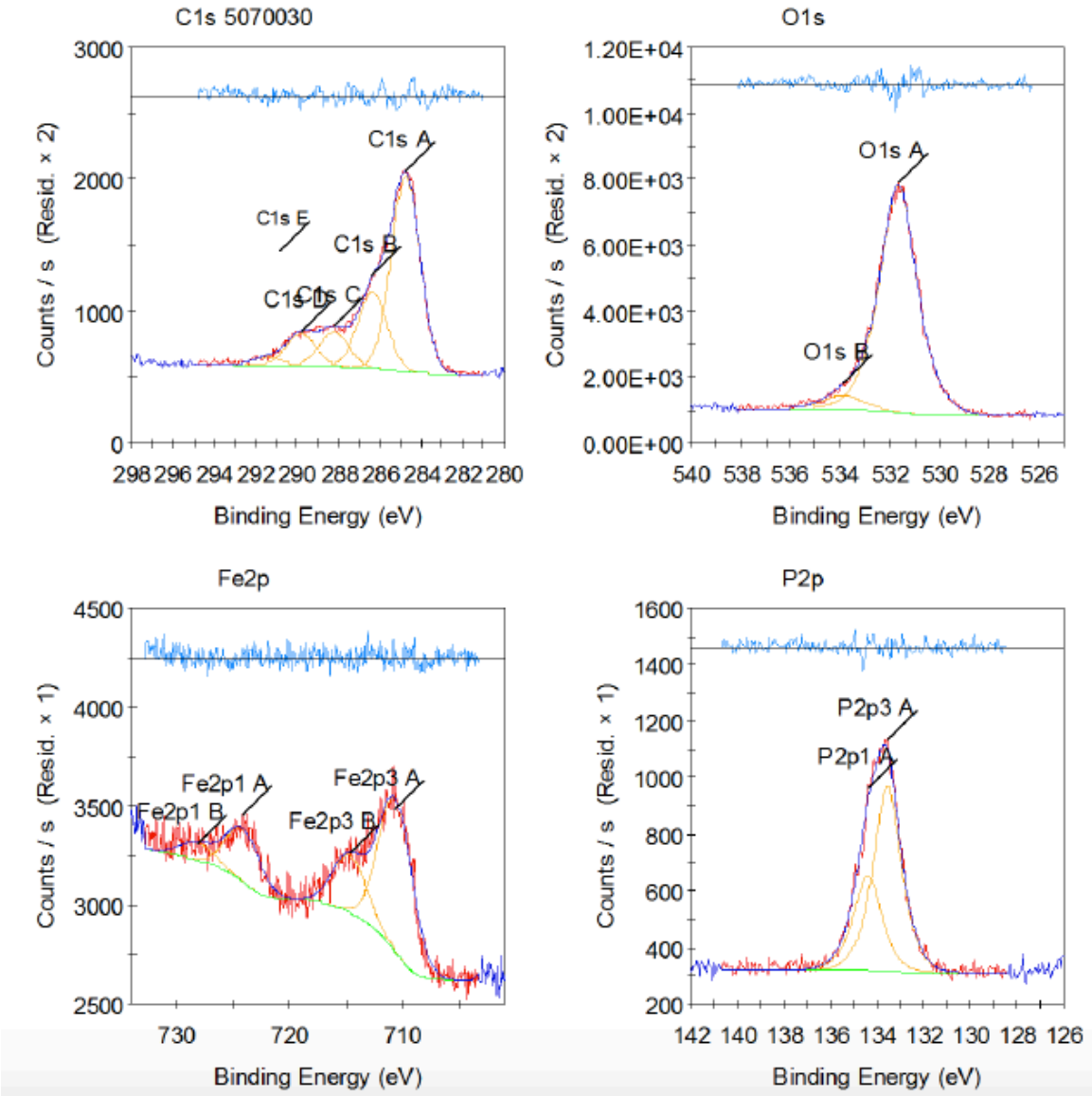

Figure 4.14: XPS spectra of the C-LFP at 700°C with 50% propylene for 30 min

4.2.4 Electrical conductivity

In order to measure electrical conductivity of the samples accurately, we used a four-point method. Electrical conductivity is calculated by Equation 9:

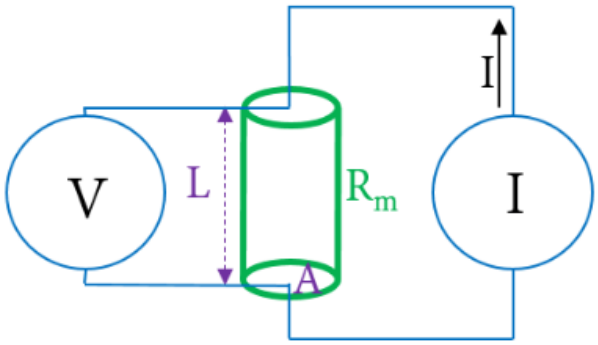

$$\sigma = \frac{L}{A} \times \frac{I}{V}$$ Equation 9

In which σ is electrical conductivity (S/cm).

To measure the resistance, a certain current (I) is supplied through the object and the voltage drop is recorded through a voltmeter. Based on the ohm's law, the corresponding resistance is calculated by Equation 10:

$$R_m = V/I$$ Equation 10

Shape and dimension of the resistance effect on the conductivity. Therefore, particles were poured inside a cylinder, which should be made from an electrical insulator material. In this case, we used glass-filled polycarbonate, which also had high mechanical strength to avoid deformation from high pressure. After particles were poured into the device, pressure was applied to the sample by a pressurized air to eliminate the void fraction between the particles and make a compressed network of the material. Then, the voltage drop obtained from altering electrical current at each pressure level was recorded, and conductivity was measured from Equation 10.

Electrical conductivity of some of the C-LFP samples versus mass fraction of the deposited carbon is presented in Table 4.6. Given the fact that electrical conductivity of pure LFP powders was about 10^{-9} S/cm, the C-LFP powders have become dramatically about 100 million times more conductive.

Table 4.6: Electrical conductivity of some of the produced C-LFP

Test Number #	Carbon content, %	Electrical conductivity, S/cm
10	1.52	0.454
11	1.44	0.291
13	1.86	0.456
14	1.83	0.532
15	1.47	0.516
20	0.64	0.055
21	0.92	0.069
22	1.48	0.126
23	0.88	0.065
24	1.79	0.152
25	1.82	0.118

4.2.5 Form of carbon (graphite or disordered)

It is known that graphitic carbon has electrical conductivity, so the more carbon deposited is of the graphitic type, the more electrically conductive C-LFP powders is expected.

Raman spectroscopy is a conventional technic to explore surface properties of the LFP and C-LFP [26, 34, 55]. The device is based on interaction of the external electromagnetic field produced by a monochromatic light (laser) with the electron cloud of the material.

The penetration depth of Raman for carbon is maximum 30 nm which is at least 1 order of magnitude larger than thickness of the coated layer deposited on LFP particles. In the cases of thin layer of carbon, a weak band at 940 cm^{-1} associated with the LFP could be observed.

The Raman spectra of the C-LFP are dominated by two D and G bands of amorphous carbon corresponding to the disordered and graphitic carbon, respectively.

Figure 4.15 illustrates Raman plots of two promising C-LFP samples from CVD tests with 3 and 50 mol% propylene. All the spectra were fit using two Gaussian line shapes. The D and G modes

are observed at 1350 cm^{-1} and 1600 cm^{-1}, respectively. The intensity ratio of D and G bands (I_D/I_G) were employed to study the nature of the carbon.

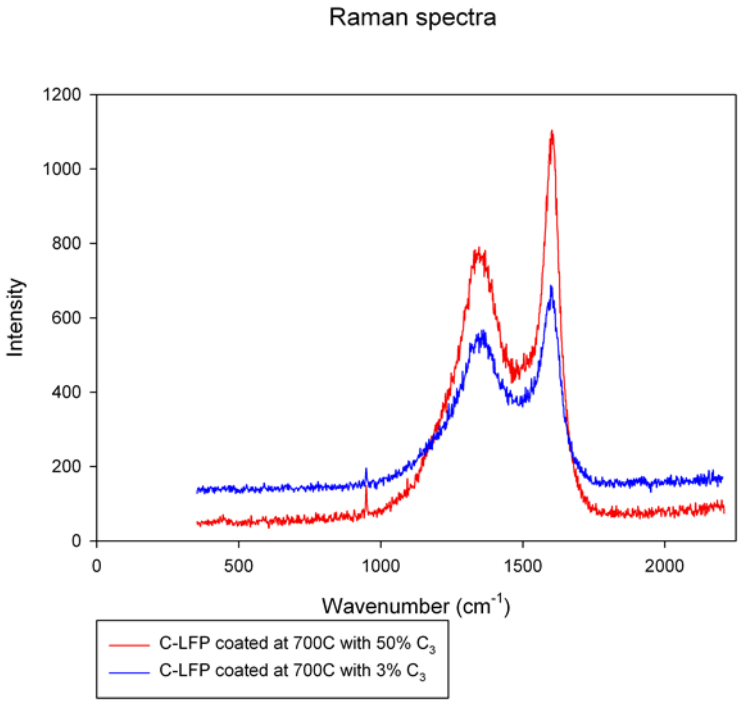

Figure 4.15: Raman spectrum of a C-LFP sample

According to Raman spectra, the C-LFP samples included only hydrogenated carbon. A hydrogen free carbon shows a peak at 600 cm^{-1}, which was not detected in the spectra of

Figure 4.15. This observation is common in carbon coating via CVD process [82]. Intensity and width of each peak is indication of the amount and crystallinity of the material, respectively. Correspondingly,

Figure 4.15 explains that quality of carbon of C-LFP by 50 mol% propylene was superior than the one of 3 mol% propylene; it is because sharpness and intensity of the related G band was higher. In addition, the I_D/I_G in the former samples was less than the latter ones, which was an evidence of more graphitic carbon.

4.3 Performance of produced C-LFP as cathode

Based on characterization of the produced C-LFP samples, some of the promising ones were selected for evaluation of their performance as cathode in a battery cell. To do so, electrochemical analysis of selected C-LFP samples were carried out to determine their performance as cathode material of a LIB. To prepare a battery cell, a slurry consists of 85% C-LFP, 9% of carbon black and 6% of PVDF as the binder was deposited on a carbon coated aluminum foil as the cathode. Carbon coating of the aluminum foil, as the current collector, is for reducing the resistance between the electrode material and current collector, which improves the rate performance of a battery [57]. The anode was a Li foil and the electrolyte was made of 1M $LiPF_6$ in EC:DEC (Ethylene carbonate: Diethyl carbonate) mass ratio of (1:2) for the cell. All the measurements were done in a coin cell configuration. Capacity tests were performed at room temperature at C/10 rate, meaning that each charge or discharge took 10 hours, between 2.2 and 4.0 volts versus Li^+/Li for 4 cycles.

The results are presented in Figure 4.16. Considering the fact that the discharge capacity of uncoated LFP powders was 40 $mAh.g^{-1}$ while its theoretical (maximum) capacity is 170 $mAh.g^{-1}$, the discharge capacity of our generated C-LFP powders significantly improved, i.e. in a range of 115 to 138 $mAh.g^{-1}$.

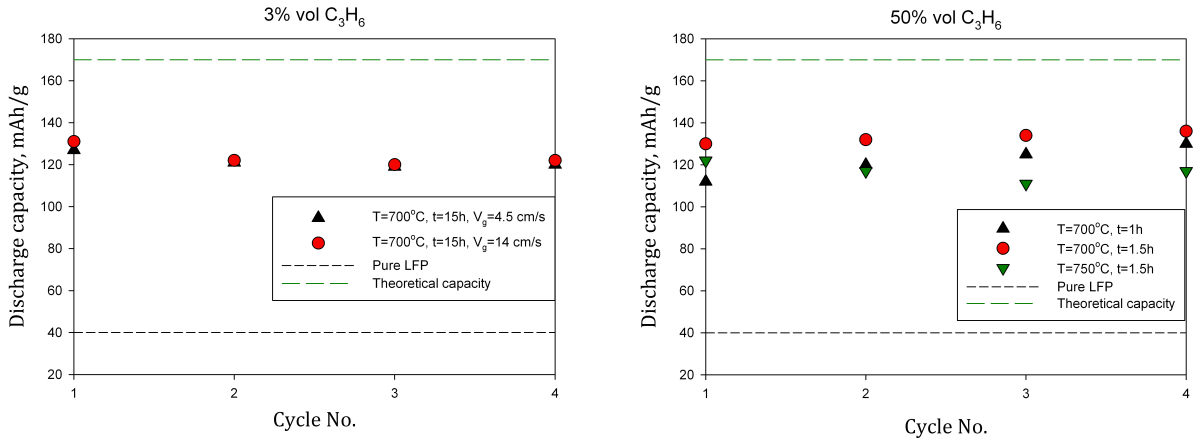

(a) (b)

Figure 4.16: Discharge capacity evolution versus cycle number for the C-LFP that were produced by the (a) 3% and (b) 50% propylene as precursor

Figure 4.16 reveals the rate capability of different promising C-LFP material at various cycles and process conditions. Interestingly, in the first cycles, the irreversible loss in capacity is observed for samples coated by the 3% mixture. Capacity degradation may be caused by:

(a) Loss of active material due to the cracking or dissolution into the electrolyte;
(b) Solid-electrolyte interface (SEI) formation which results in increment of the cell impedance; and
(c) Physical degradation of electrode structure [13, 76].

Generally, SEI formation plays the main role in capacity fade of a battery. SEI formation usually occurs over thousands of cycles. However, in case of our results, this could be as a result of peeling the deposited carbon off the LFP surface since carbon was not satisfactorily coated on the surface of this LFP powders, i.e. based on the observation of peeled carbon in TEM images. In addition, the slow Li-ion diffusion and poor electrical contact between cathode particles and conductor originated from large particles and thick carbon coated layer on the particles surface could be the other reasons for the early capacity fading of the samples from 3 mol% propylene [54].

The results indicate that performance and efficiency of the cathode material is affected by the coating process conditions, specially carbon structure and content. Long process time in low gas concentration resulted in formation of more disordered carbon and diminishing of the rate capability. Generally, the C-LFP which produced at 700 °C by the 50 mol% propylene mixture showed better discharge capacity compared to the one of the 3 mol% propylene mixture (Figure 4.16). That should be attributed to better uniformity and type, i.e. more graphite carbon, of the deposited carbon.

As illustrated in Figure 4.16, all the coated materials except C-LFP coated at 750°C, became activated after initial cycles. This could be attributed to the presence of some impurities which were probably existed in the fresh LFP powders supported by XRD data. In general, these impurities are produced upon LFP oxidation, such as α-Fe_2O_3 and $FePO_4$, in LFP material that is electrochemically inactive in initial charge process. During subsequence discharge process and lithiation, they become active and cause improvement in the total discharge capacity. For the samples coated at 750 °C, due to the high conversion level of propylene and providing a reductive atmosphere, presence of these impurities is less likely. There is a similar logic behind

activation of the coated sample produced from 3 mol% propylene where long reaction time and high gas conversion reduced the LFP. Production of water detected by FTIR at the beginning of the reaction is an indication such a reduction reaction.

The discharge capacity of our C-LFP powders was also compared to C-LFP powders that were obtained by lactose pyrolysis at University of Montreal. The difference does not necessarily explain that their carbon precursor or coating process were more efficient, because their coating process was carried out right after the LFP powders were synthesized. This prevents their samples being expose to environment such as humidity and air which reduces their impurities [83] as opposed to our uncoated LFP samples. For instance, as discussed earlier, Li_3PO_4 was detected on XRD plot of the as-received LFP powders that indicated oxidation of LFP occurred before applying any CVD test. It should be noted that Li_3PO_4 affects detrimentally on the capacity and electrochemical performance of the LFP cathode particles [84].

Another important parameter in evaluating performance of a battery is Coulombic efficiency (CE) which is defined as follows:

CE= (charge delivered during discharge)/ (charge stored during previous recharge)

CE is the indicator of the battery calendar life, battery aging. The materials with higher CE have longer lifetime and better performance. Normally CE increases with time and further cycling due to thickening and stabilization of SEI.

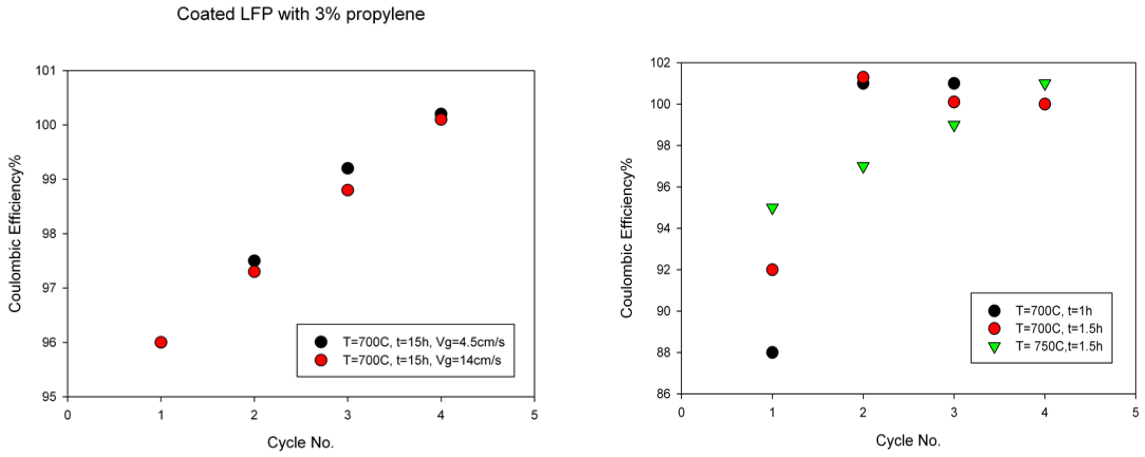

(a) (b)

Figure 4.17: Columbic efficiency evolution versus cycle number for the C-LFP that were produced by the (a) 3% and (b) 50% propylene as precursor

Figure 4.17 shows the CE evolution for the C-LFP produced from 3 and 50 mol% propylene. Except the first cycles, this figure shows acceptable coulombic efficiency (almost 100%) for the samples, which is probably due to the activation of the conductive carbon coated on the particles surface. Sometimes, CE exceeds the unity as in the case of C-LFP coated by 50% propylene. This phenomenon is caused by the impact of Li atoms that are stored and overhang in the negative electrode and extends past the positive electrode. However, results of the CE in 4 cycle is not informative and more cycles have to be performed [85].

The other important parameter in evaluating the performance of a battery is related to the accessible voltage during the charge and discharge steps. The charge/discharge profile, i.e. galvanostatic curve of the two promising C-LFP samples is illustrated in Figure 4.18 in such a way that the black and red curves represent the C-LFP which were produced by the 3 and 50 mol% propylene, respectively. The flatness of the profile at 3.4-3.5 V is attributed to the nature of LFP-$FePO_4$ oxidation/reduction potential. The high-polarized profile of the black curve is an indication of the high electrode resistance emanated from large particle agglomerations and non-uniform carbon coated powders. However, the red curve has more flat voltage at 3.5V and higher initial capacity of 135 $mAh.g^{-1}$, though this sample also suffers from large particle size of LFP powders, 125 to 250 μm.

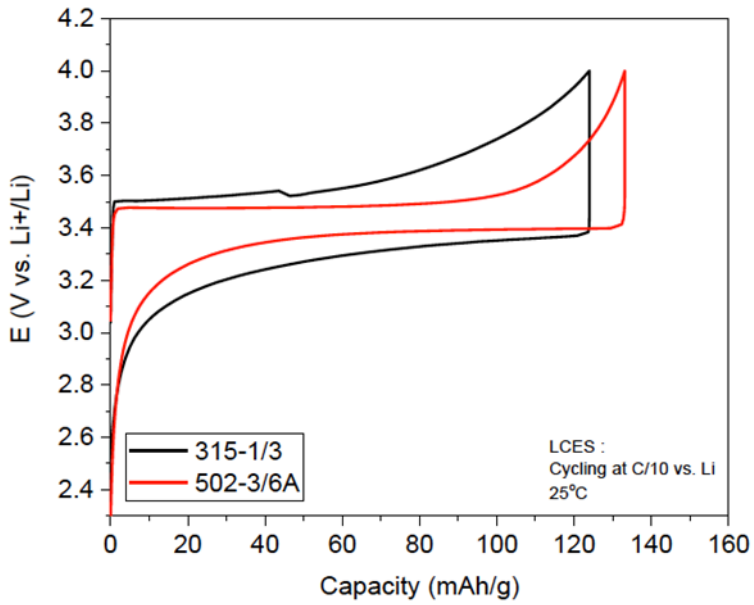

Figure 4.18: Charge-discharge profile for the C-LFP samples at 0.1C rate

High polarization especially at the end of the charge/discharge cycle is a sign of high resistance of the material and slow reaction kinetic coefficient [54, 73]. As discussed formerly, long coating process duration caused particle sintering that led to grown agglomerations. Thus, negative effect of these agglomerations is manifested in galvanostatic voltage. Moreover, the results obtained for the galvanostatic analysis is related to the first cycle. Usually the first cycle shows higher polarization than the consequent cycles. During the preparation process of the cell, electrode particles are pressed that leads to formation of some agglomerates. After the first cycle, these agglomerates break and the resistance will be reduced. Moreover, the low voltage plateau of the coated material is associated with some impurities resulted by the LFP oxidation.

Considering performance of the produced C-LFP as cathode, one can conclude that the applied FB-CVD process is a promising technic for gas-phase carbon coating of the LFP powders. In comparison with performance of other C-LFP which were reported in literature, the one of ours was noticeable. However, quality of the produced C-LFP required more improved. This can be done through two main streams: firstly, using a better quality fresh LFP particles which have no impurity, and secondly, using finer LFP particle size since some of the performance issues were related to the size of particles. To do the later, we should overcome the problems related to fluidization of the cohesive particles which is the topic of next chapter.

CHAPTER 5 RESULTS AND DISCUSSION: PAFB-CVD

As discussed in the previous chapter, C-LFP powders produced fresh LFP of secondary size distribution of 125 to 250 μm, despite the very promising electrochemical enhancements, suffered from their relatively large particle size. Therefore, a new motivation started to coat LFP powders with smaller secondary size distributions.

Therefore, a novel pulsation technique was commissioned to apply the FB-CVD to the very cohesive LFP powders. At the first step, a hydrodynamic study was carried out at ambient temperature to verify impact of the pulsation technique to reach full fluidization status across the bed, and to optimize its operation in term of pulsation frequency and minimum fluidization velocity. Hydrodynamic study was carried out employing a transparent tube equipped with differential pressure transducers.

5.1 Fluidization of cohesive LFP powders in absence of pulsation assistance

In the first step, we tried to fluidize particles with the conventional aerating fluidization. The bed consisted of 29 grams of LFP powders with secondary size distribution of 45 to 75 μm.

The fluidization experiments were conducted in the range of 0 to 4.3 cm/s of gas velocity at ambient conditions. Since such LFP powders were very cohesive, it was expected to observe a poor fluidization.

Figure 5.1 shows that an air pocket lifted the LFP bed at a low air velocity, i.e. 0.37 cm/s, until it burst, and channels were formed across the bed at high air velocities, i.e. 4.39 cm/s.

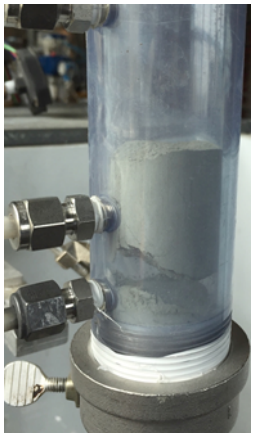

(a)

(b)

Figure 5.1: Bed snapshot at gas velocity of (a) 0.37 cm/s and (b) 4.39 cm/s for LFP particles with the size range of 45 to 90 μm

To better understand fluidization behavior of the LFP particles, the bed pressure drop versus gas velocity, in increasing and decreasing trends, was measured and presented in Figure 5.2. Under steady flow conditions, gas carried over a great portion of the bed. The initial part in the fluidization trend in Figure 5.2 illustrates this phenomenon. The cohesive forces cause change in the behavior of the bed at the onset of fluidization. Small diameter and plastic material of the column were also affecting factors to increase the cohesiveness of the bed and lift the whole bed to the top of the column. By increasing gas velocity, the bed was partially collapsed and the bed pressure drop decreased. At low gas velocities, no considerable movement was observed in the bed, while some cracks were generated and it mostly behaved like a fixed-bed regime. This bears out that drag force of the gas did not have enough energy to overcome prominent amount of inter particle forces presented within the bed.

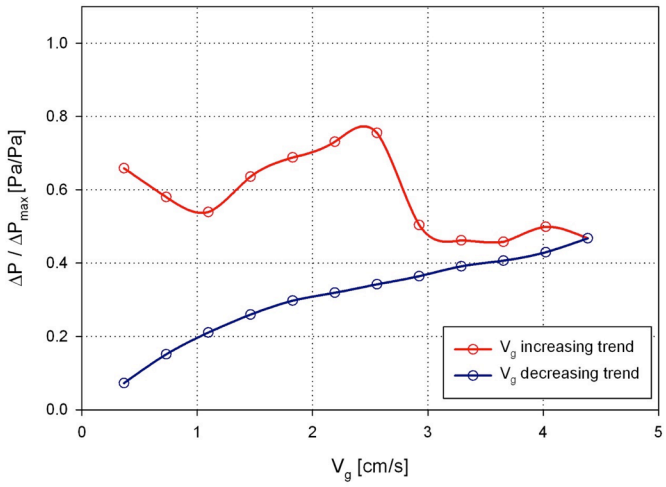

Figure 5.2: Bed pressure drop variation based on gas velocity for LFP particles with the size range of 45 to 90 μm

By increasing gas velocity over the time, the air pocket was again formed and at a certain point, this pocket completely vanished and the solid bed was collapsed due to the formation of some cracks inside the bed. At higher gas velocities, these cracks became bigger, wider and merged together and made some channels inside the bed. Thus, the gas bypassed through these channels and partially fluidized the bed so that mostly fine agglomerates were at the surface of the bed.

As a result, the pressure drop was low and the regime inside the bed was mostly like a fixed bed. The hysteresis seen here can be attributed to the non-homogeneous initial packing of the particles inside the bed [86].

It can be found that the bed pressure drop continuously diminished by decreasing the gas velocity and the reduction trend was smooth that indicated more homogeneous bed structure. It can be explained by this fact that by reducing gas velocity, inter particle forces found an opportunity to rise. When cohesive forces became stronger, the fluidized particles tended to form bigger agglomerates and became de-fluidized.

It is worth mentioning that this type of material showed fluidization behavior of ABF and it is was not possible to reach complete and smooth fluidization of the bed with conventional method of fluidization. Thus, there should be an assistant to fluidize this type of material.

5.2 Pulse-assisted fluidization of cohesive LFP powders

5.2.1 Bed pressure profile

The evolution of the total bed pressure drop versus increasing gas velocity is plotted in Figure 5.3a. This plot was to determine the minimum fluidization velocity at different pulsation frequencies. ΔP_{max} is the pressure associated with the weight of the solid bed. At the point that $\Delta P = \Delta P_{max}$, full fluidization is achieved.

The results confirm our observation that by applying a flow of gas with low velocity, due to the high adhesion of the particles inside the bed, an air pocket appeared and lifted the bed up. Consequently, since the pulsed gas did not have enough energy to break the gas pocket, pressure drop was high. It means that at low gas flow rates, gas pulsation did not impress any considerable effect.

By increasing the gas velocity, the air pocket was broken due to the big jets coming out from the distributer and the bed was collapsed, so did the pressure drop.

According to Figure 5.3a, minimum fluidization velocity depends on the gas pulsation frequency. Generally, U_{mf} increased via an increase of pulsation frequency. We obtained the lowest U_{mf} at frequency of 3.8 Hz, which was almost the same minimum fluidization velocity at 3.6 Hz. This result is explained by the fact that closing the valve for a longer time causes the gas to get pressurized more behind the solenoid valve. Consequently, stronger and longer jets are introduced into the bed from the gas distributor.

Figure 5.3b illustrates the total bed pressure drops versus superficial gas velocity with a decreasing trend. It is observed that by decreasing flow of the gas, due to the bed hysteresis, wall effect and consequently larger apparent size of powders, interparticle forces appeared and quality of fluidization deteriorated. Therefore, it is crucial to take decline of gas velocity into consideration during an operation.

Figure 5.4 depicts a snapshot of the LFP bed that was fully fluidized with assistance of the pulsation technique.

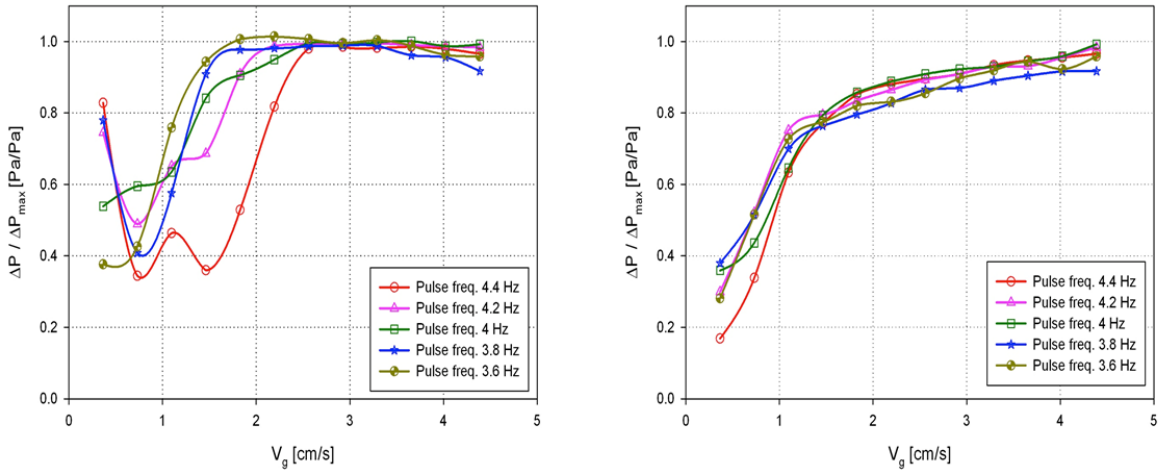

(a) (b)

Figure 5.3: Pulse-assisted fluidization curve with (a) increasing gas velocity and (b) decreasing gas velocity

Figure 5.4: Snapshot of pulse-assisted fluidized bed

5.2.2 Standard deviation analysis

Figure 5.5 describes variation of standard deviation of pressure drop versus the gas velocity. To perform all these tests, solenoid valve started to run before injecting any gas into the reactor and all these data were recorded under inlet gas pulsation. Normally, standard deviation of pressure

drop is an indication of the bubbles inside the bed; it means that bigger standard deviation is representative of the bigger bubbles formation inside the bed.

With respect to graphs in Figure 5.5, standard deviations reached a maximum point when gas velocity started to increase. Such maximum points indicated the biggest bubble formed inside the bed. By decreasing frequency of the gas, this maximum point was achieved at lower gas velocities; there was no maximum point at the lowest pulsation frequency.

After a maximum point, standard deviation dropped down. More bubbles were formed and larger bubbles burst to smaller ones. Subsequently, the standard deviation stayed at almost the same level at higher gas velocities which means that the bubble size didn't change after reaching a minimum fluidization velocity. The results from standard deviation analysis are consistent with the results from pressure drop analysis, which revealed that minimum fluidization velocity was less in lower gas pulsation frequencies.

It can be derived that at higher pulse frequencies since the gas is not that much pressurized and the jets are weaker and shorter, the bubbles are small in the bubbling regime.

Decreasing trend of standard deviation upon decrease of gas velocity (Figure 5.5b) explains appearance of interparticle forces similar to observation in Figure 5.4b.

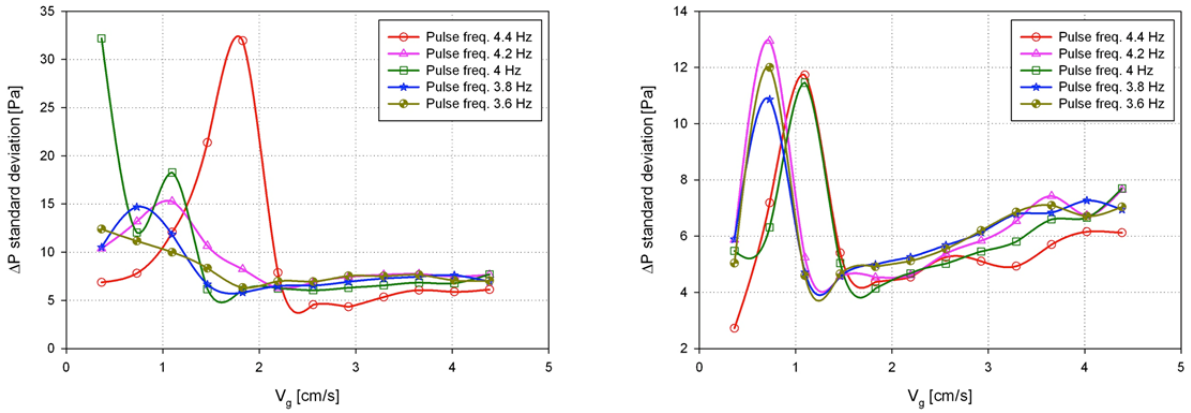

Figure 5.5: Standard deviation of pressure drop dependency to superficial gas velocity in pulse-assisted fluidization for (a) increasing gas velocity and (b) decreasing gas velocity

5.3 Carbon coating of fine LFP powders with PAFB-CVD

As confirmed in pervious section, the developed pulse-assisted fluidized bed overcame adequately the difficulties regarding fluidization of the Geldart's group C particles. Therefore, in this section, we employed this novel setup, namely as PAFB-CVD, for carbon coating of the LFP particles with the available smallest particle size, i.e. 45 to 90 μm by the CVD process. These LFP particles were from the same source of the LFP particles which were used in the previous chapter.

Figure 5.6 portrays SEM images of these LFP particles. Figure 5.6a reveals some information about their particle shapes and size distribution, while Figure 5.6b elaborates each individual secondary particle that was porous and made of agglomerated primary submicron LFP particles. This improves the deposition reaction by providing more active sides in two ways: firstly, reduction in the particle size provides more surface for the reaction, and secondly, gas can penetrate into the porous particles easier since the particle size is smaller.

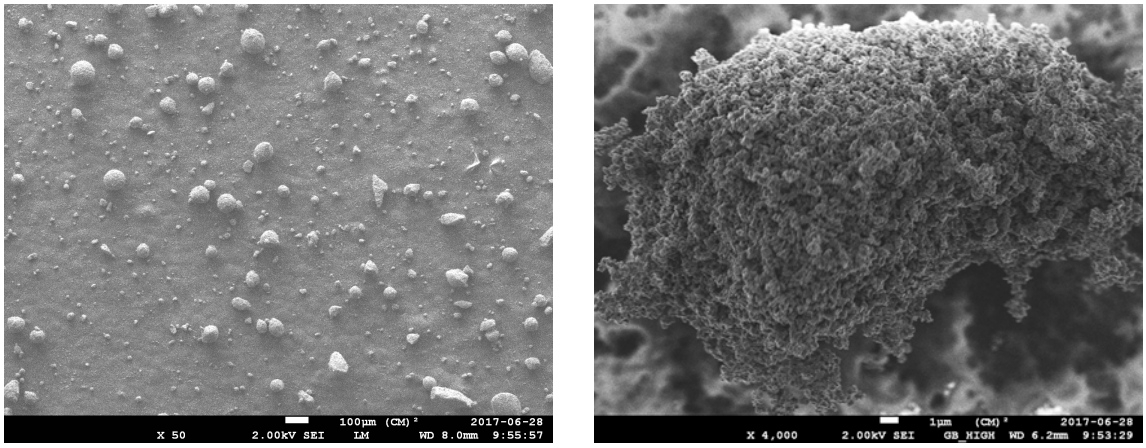

(a) (b)

Figure 5.6: SEM images of the pure fine LFP particles

The 50 % propylene mixture was employed as carbon precursor since it was proved to produce a better quality of deposited carbon in previous chapter.

We used 3 grams of LFP particles in each test due to a limitation regarding the amount of available LFP particles in the range size of 45 to 90 μm. Several samples were prepared for the

current studies. From pervious chapter, 700 °C was obtained as the optimum reaction temperature. Thus, at the first step of the current study, the reaction temperature was set at 700 °C; however, we performed the reaction at three other temperatures of 600, 650 and 750 °C to investigate the effect of temperature on the CVD process using the developed PAFB-CVD reactor. The design of experiments is presented in Table 5.1.

Table 5.1: Design of experiments

Test #	LFP mass, g	Propylene, mole%	Temperature, °C	Time, min	Gas velocity, cm/s
28	3	50	700	60	2
29				30	
30				20	
31				10	
32				5	
33			600	60	
34			650		
35			750		

5.3.1 Evaluation of carbon coating by PAFB-CVD reactor

The quality of the produced C-LFP by the PAFB-CVD process was strikingly superior in comparison to the one of the previous work even based on observation. However, to better compare the products, the carbon content and electrical conductivity of these C-LFP particles were measured in the same manner as the pervious chapter, and presented in Table 5.2.

Table 5.2: Carbon content and electrical conductivity of the produced C-LFP with the PAIHFBR

Test #	Temperature,°C	Time, min	Carbon, w%	Electrical Conductivity, S/cm
28	700	60	7.32	3.9
29	700	30	1.98	2.9
30	700	20	1.36	2.0
31	700	10	0.82	1.2
32	700	5	0.60	0.7
33	600	60	0.59	0.2
34	650	60	1.34	1.4
35	750	60	11.30	14.1

Considering experiments No. 28 to 32, increasing the reaction time increased the amount of deposited carbon almost linearly from 5 to 30 min. However, the rate of deposition was significantly higher for the reaction time from 30 to 60 min. Considering experiments No. 28 and 33 to 35, increasing the reaction temperature resulted in larger mass of deposited carbon. Expectedly, the carbon mass increased with the temperature rapidly at a temperature higher than 650 °C.

Accordingly, electrical conductivity increased via larger mass of deposited carbon. As the aim of these series of experiments was to illustrate the effect of the LFP size, the results were compared with the results from the previous chapter. In general, increasing the reaction time and temperature resulted in higher mass of deposited carbon. Interestingly, carbon coating through the CVD process was successful even at low temperatures of 600 and 650 °C where the mass of deposited carbon could exceed the one of produced C-LFP from the coarse LFP particles at 750 °C discussed in the previous chapter.

Although based on the thermodynamic study carbon should be formed upon propylene decomposition at these temperatures, no carbon was detected onto coarse LFP samples as opposed to findings of this research. This phenomenon could be explained by this fact that reduction in particle size resulted in having more active sites for propylene cracking and carbon deposition.

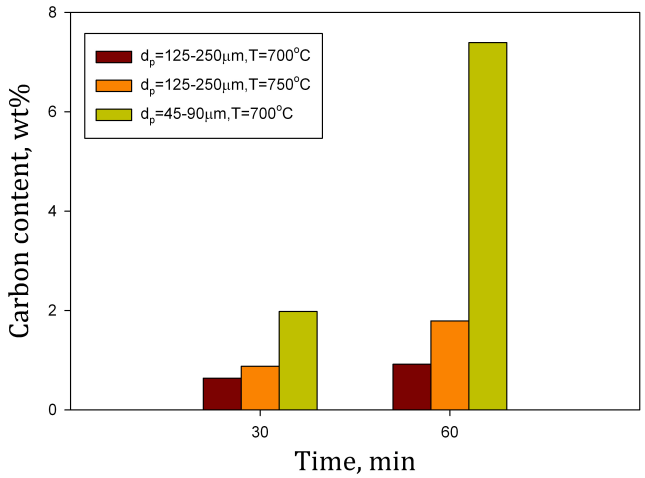

Figure 5.7: Carbon content of the produced C-LFP by different LFP particle size versus reaction time at 700 and 750°C

Figure 5.7 displays a comparative scheme of the carbon content of the fine LFP sample coated at 700 °C by PAFB-CVD while the coarse ones coated at 700 and 750°C by FB-CVD. Almost three times more carbon deposited on the fine samples. A main reason for this increase in the deposited carbon, beside the smaller LFP particle size, is related to the hydrodynamics within the developed PAFB-CVD. The novel reactor enabled us to work with a low gas velocity, i.e. 2 cm/s for our experiments, which corresponded to higher gas residence time while providing satisfactory gas solid contact and enhanced mass transfer.

Figure 5.8 illustrates the electrical conductivity of C-LFP samples of different size distributions versus their carbon content. As mentioned, the electrical conductivity increased with increase in the carbon content of C-LFP. However, the electrical conductivity of the C-LFP with smaller particle size was about one order of magnitude higher than the one of the coarser C-LFP particles. This could be attributed to the fact that in the smaller LFP particles, the gas could easily penetrate into the pores of the LFP particles and led to a better coating of the primary LFP particles. We will get back to this when presenting the TEM images.

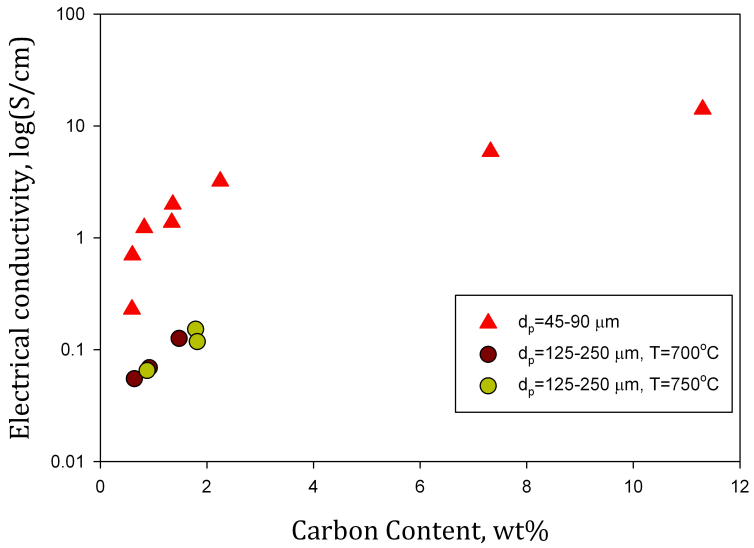

Figure 5.8: Electrical conductivity of the produced C-LFP particles based on their carbon content

The other important parameters in carbon coating of the LFP particles are related to morphology and uniformity of the coating. SEM image of one of the produced C-LFP samples at 700 °C (Figure 5.9) qualitatively confirms that carbon was uniformly deposited onto surface of all the particles. In addition, it reveals that the LFP particles were not sintered since size of the C-LFP particles was similar to that of the uncoated LFP particles.

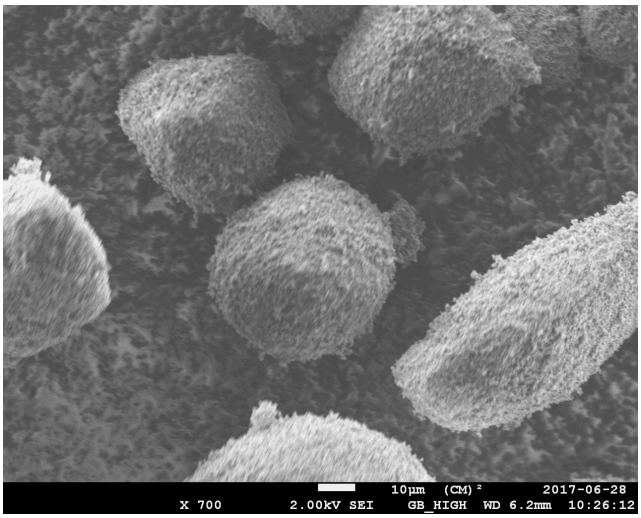

Figure 5.9: SEM images of the C-LFP material coated at 700°C

To better evaluate uniformity of coatings, Figure 5.10 presents TEM images of some of the produced C-LFP samples from the PAFB-CVD reactor. Figure 5.10a and b confirm the uniformity of coating on the primary LFP particles, while the SEM image was related to secondary particles. As previously mentioned, this was the main reason for having one order of magnitude higher electrical conductivity for the C-LFP with smaller particle size compared to the C-LFP with coarser particle size. Moreover, these figures prove that the particles were not sintered during the CVD process. Figure 5.10c and d clearly show the deposited carbon layer on one LFP particle obtained at 650 and 700 °C, respectively. Such outstanding results reveals how the deposited layer thickness was increased by increasing the reaction temperature for the same reaction time whereas the coated layer was uniform.

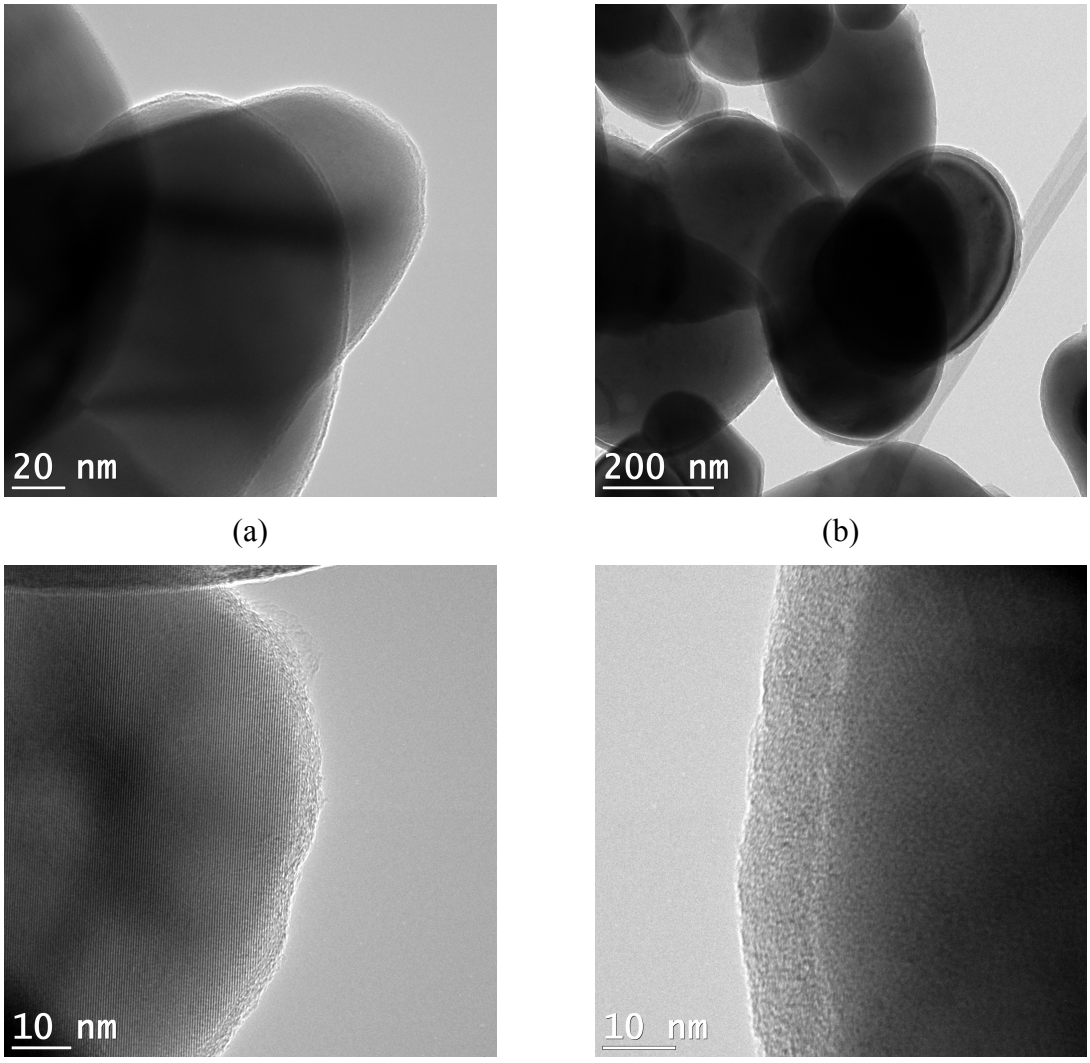

(a) (b)

(c) (d)

Figure 5.10: TEM images of the C-LFP coated in PAFB-CVD reactor: (a) and (b) at 700°C in 20 min, (c) 650°C in 60 min, and (d) at 700°C in 60 min

Electrochemical performance of the fine C-LFP particles were evaluated in a similar manner as the previous chapter. Three samples based on their carbon content, i.e. the closest three to 1% carbon content, were selected as candidate samples for electrochemical tests. Table 5.3 presents the averaged charge/discharge capacity of these three samples for the first 15 cycles. Considering the fact that these LFP particles were stored for a longer period, they would likely have more impurities due to oxidation which consequently undermine the performance results like discharge

capacity. However, their performance was strikingly better than the performance of the samples of the pervious chapter.

Table 5.3: Averaged charge/discharge capacity of the selected C-LFP over first 15 cycles

Test#	Charge capacity, mAh/g	Discharge capacity, mAh/g	Columbic efficiency, %
30	135.2±1	131.1±1	96.92
31	141.6 ±1	139.9±1	98.79
34	138.1±1	134.5±1	97.39

Based on the discussions, one can conclude that the developed gas-phase CVD process is a satisfactory method to coat carbon on fine LFP particles for battery applications. Moreover, coating the smaller secondary LFP particle size will improve its performance as cathode materials. Furthermore, the PAFB-CVD reactor is an adequate setup to conduct the CVD process on the cohesive LFP particles.

CHAPTER 6 CONCLUSION AND RECOMMENDATIONS

6.1 Conclusion

As a process alternative to conventional processes of carbon coating onto surface of LFP powders, a new gas-phase carbon coating process including a novel fluidized bed chemical vapor deposition reactor (FB-CVD) taking advantage of inducting heating mechanism was developed. The FB-CVD is flexible to coat Geldart's group A and C powders. In case of the cohesive Geldart's group C powders, a solenoid valve in the reactor outlet is employed to supply gas pulsations to overcome interparticle forces in between the LFP powders.

Taking propylene as the best precursor after screening of several carbon precursors, the CVD operating conditions such as temperature, reaction time, gas concentration and gas residence time were optimized with respect to uniformity and thickness of coated layer of carbon, amount of graphite carbon and electrochemical properties of produced C-LFP powders of Geldart's group A. In fact, the developed FB-CVD process led to the uniform, ultrathin and full coating layer of graphitic carbon on each primary particle of LFP. More importantly, an extraordinary electrical conductivity, 10^{10} times more than conductivity of uncoated LFP, and significant enhancement of discharge capacity were obtained.

The optimized CVD operating conditions were employed to coat carbon onto surface of cohesive LFP powders, Geldart's group C powders, with a pulse-assisted FB-CVD reactor setup. Comparison of results from FB and PAFB tests disclosed that quality of coating in terms of uniformity and coverage on PAFB reactor, electrical conductivity as well as electrochemical properties of the produced C-LFP was noticeably enhanced. This could be explained by the fact that reducing particle size provides more LFP active sites on the LFP surface. Combination of particle size reduction with longer gas residence time resulted in a decent gas-solid contact and an improved mass transfer.

This study proved that fine cohesive LFP powders can be smoothly and entirely fluidized with assistance of gas pulsation with negligible elutriation of particles. This approach can be used for any kind of Geldart's group C powders and even particles with specific type of morphology, without adding any device and excess effort, hence it can be utilized in a wide range of applications.

The last but not the least, the newly developed PAFB-CVD setup requires shorter reaction time and slower gas velocity that are key advantage of the technic; thus, directly reducing cost of the process.

6.2 Recommendations

1. This research was carried out with LFP samples that were synthesized by a hydrothermal method. A challenge was the time-lag between production of LFP powders and production of C-LFP. It is strongly recommended to minimize such a time-lag to avoid any environmental post-synthesis influences such as oxidation that would have finally detrimental effect on performance of C-LFP powders.

2. To reach as close as possible the ideal discharge capacity of 170 mA.h/g of LFP powders, the type, mass and distribution of coated carbon must be optimized and trace of impurities must be removed. Therefore, further investigations would be beneficial such as:
   - Applying a reduction pre-treatment on LFP powders before running a CVD test;
   - Heat-up rate with or without carbon precursor;
   - Smaller particle size: secondary agglomerates with less than 20 μm;
   - LFP raw material with no impurity and performing EC analysis for such a material;
   - Testing LFP powders synthesized by other methods such as melt casting;

3. Even though conversion of propylene was quite low in one pass through the fluidized bed, we propose to design a circulating fluidized bed reactor where unconverted propylene and the product gases can return to the bed until desired layer of carbon is coated on the surface of LFP powders. Such a design would help reduce OPEX of the process dramatically as less amount of propylene might be consumed and shorter reaction time would be required.

4. Pulsation mechanism must be studied in detail to better understand influential parameters involved in overcoming the interparticle forces in order to optimize the pulsation operation for a given LFP material.

BIBLIOGRAPHY

1. Latifi, M. and J. Chaouki, *A novel induction heating fluidized bed reactor: Its design and applications in high temperature screening tests with solid feedstocks and prediction of defluidization state.* AIChE Journal, 2015. **61**(5): p. 1507-1523.

2. Mizushima, K., et al., *LixCoO2 (0< x<-1): A new cathode material for batteries of high energy density.* Materials Research Bulletin, 1980. **15**(6): p. 783-789.

3. Park, J.-K., *Principles and applications of lithium secondary batteries*. 2012: John Wiley & Sons.

4. Etacheri, V., et al., *Challenges in the development of advanced Li-ion batteries: a review.* Energy & Environmental Science, 2011. **4**(9): p. 3243-3262.

5. Toprakci, O., et al., *Fabrication and electrochemical characteristics of LiFePO 4 powders for lithium-ion batteries.* KONA Powder and Particle Journal, 2010. **28**(0): p. 50-73.

6. Li, H. and H. Zhou, *Enhancing the performances of Li-ion batteries by carbon-coating: present and future.* Chemical Communications, 2012. **48**(9): p. 1201-1217.

7. Goriparti, S., et al., *Review on recent progress of nanostructured anode materials for Li-ion batteries.* Journal of Power Sources, 2014. **257**: p. 421-443.

8. Whittingham, M.S., *Lithium batteries and cathode materials.* Chemical reviews, 2004. **104**(10): p. 4271-4302.

9. Julien, C.M., et al., *Comparative issues of cathode materials for Li-ion batteries.* Inorganics, 2014. **2**(1): p. 132-154.

10. Nitta, N., et al., *Li-ion battery materials: present and future.* Materials today, 2015. **18**(5): p. 252-264.

11. Fergus, J.W., *Recent developments in cathode materials for lithium ion batteries.* Journal of Power Sources, 2010. **195**(4): p. 939-954.

12. Zhang, Y., et al., *Advances in new cathode material LiFePO 4 for lithium-ion batteries.* Synthetic Metals, 2012. **162**(13): p. 1315-1326.

13. Zhang, W.-J., *Structure and performance of LiFePO 4 cathode materials: A review.* Journal of Power Sources, 2011. **196**(6): p. 2962-2970.

14. Padhi, A.K., K. Nanjundaswamy, and J.B. Goodenough, *Phospho-olivines as positive-electrode materials for rechargeable lithium batteries.* Journal of the electrochemical society, 1997. **144**(4): p. 1188-1194.

15. Herstedt, M., et al., *Surface chemistry of carbon-treated LiFePO4 particles for Li-ion battery cathodes studied by PES.* Electrochemical and Solid State Letters, 2003. **6**(9): p. A202-A206.

16. Belharouak, I., C. Johnson, and K. Amine, *Synthesis and electrochemical analysis of vapor-deposited carbon-coated LiFePO 4.* Electrochemistry Communications, 2005. **7**(10): p. 983-988.

17. Zaghib, K., et al., *Relationship between local structure and electrochemical performance of LiFePO4 in Li-ion batteries.* Ionics, 2008. **14**(4): p. 271-278.

18. Jugović, D. and D. Uskoković, *A review of recent developments in the synthesis procedures of lithium iron phosphate powders.* Journal of Power Sources, 2009. **190**(2): p. 538-544.

19. Julien, C., A. Mauger, and K. Zaghib, *Surface effects on electrochemical properties of nano-sized LiFePO4.* Journal of Materials Chemistry, 2011. **21**(27): p. 9955-9968.

20. Zhang, Y., et al., *One-step microwave synthesis and characterization of carbon-modified nanocrystalline LiFePO 4.* Electrochimica Acta, 2009. **54**(11): p. 3206-3210.

21. Higuchi, M., et al., *Synthesis of LiFePO 4 cathode material by microwave processing.* Journal of Power Sources, 2003. **119**: p. 258-261.

22. Wang, L., et al., *Preparation and characterization of nano-sized LiFePO 4 by low heating solid-state coordination method and microwave heating.* Electrochimica acta, 2007. **52**(24): p. 6778-6783.

23. Julien, C., et al., *Characterization of the carbon coating onto LiFePO4 particles used in lithium batteries.* Journal of Applied Physics, 2006. **100**(6): p. 063511.

24. Salah, A.A., *Reduction Fe3+ of Impurities in LiFePO4 from Pyrolysis of Organic Precursor Used for Carbon Deposition.* The Electrochemical Society, 2006. **153**(9): p. 10.

25. Salah, A.A., et al., *Nano-sized impurity phases in relation to the mode of preparation of LiFePO 4.* Materials Science and Engineering: B, 2006. **129**(1): p. 232-244.

26. Salah, A.A., et al., *Reduction Fe3+ of impurities in LiFePO4 from pyrolysis of organic precursor used for carbon deposition.* Journal of the Electrochemical Society, 2006. **153**(9): p. A1692-A1701.

27. Dokko, K., K. Shiraishi, and K. Kanamura, *Identification of surface impurities on LiFePO4 particles prepared by a hydrothermal process.* Journal of the Electrochemical Society, 2005. **152**(11): p. A2199-A2202.

28. Jin, B., et al., *Effect of different carbon conductive additives on electrochemical properties of LiFePO4-C/Li batteries.* Journal of Solid State Electrochemistry, 2008. **12**(12): p. 1549-1554.

29. King, D.M., et al., *Atomic layer deposition of TiO 2 films on particles in a fluidized bed reactor.* Powder Technology, 2008. **183**(3): p. 356-363.

30. Yu, D.Y.W., et al., *Impurities in LiFePO(4) and their influence on material characteristics.* Journal of the Electrochemical Society, 2008. **155**(7): p. A526-A530.

31. Hsu, K.-F., S.-Y. Tsay, and B.-J. Hwang, *Synthesis and characterization of nano-sized LiFePO 4 cathode materials prepared by a citric acid-based sol–gel route.* Journal of Materials Chemistry, 2004. **14**(17): p. 2690-2695.

32. Choi, D. and P.N. Kumta, *Surfactant based sol–gel approach to nanostructured LiFePO 4 for high rate Li-ion batteries.* Journal of Power Sources, 2007. **163**(2): p. 1064-1069.

33. Konarova, M. and I. Taniguchi, *Preparation of LiFePO 4/C composite powders by ultrasonic spray pyrolysis followed by heat treatment and their electrochemical properties.* Materials Research Bulletin, 2008. **43**(12): p. 3305-3317.

34. Xie, H.M., et al., *Optimized LiFePO4–Polyacene Cathode Material for Lithium-Ion Batteries.* Advanced Materials, 2006. **18**(19): p. 2609-2613.

35. Yang, M.-R., T.-H. Teng, and S.-H. Wu, *LiFePO 4/carbon cathode materials prepared by ultrasonic spray pyrolysis.* Journal of power Sources, 2006. **159**(1): p. 307-311.

36. Yang, M.-R., W.-H. Ke, and S.-H. Wu, *Preparation of LiFePO 4 powders by co-precipitation.* Journal of power sources, 2005. **146**(1): p. 539-543.

37. Wang, Y., Z. Liu, and S. Zhou, *An effective method for preparing uniform carbon coated nano-sized LiFePO 4 particles.* Electrochimica Acta, 2011. **58**: p. 359-363.

38. Daheron, B. and D.D. MacNeil, *Study of LiFePO4 synthesized using a molten method with varying stoichiometries.* Journal of Solid State Electrochemistry, 2011. **15**(6): p. 1217-1225.

39. Gauthier, M., et al., *Melt casting LiFePO4 I. Synthesis and characterization.* Journal of the Electrochemical Society, 2010. **157**(4): p. A453-A462.

40. MacNeil, D., et al., *Melt casting LiFePO4 II. Particle size reduction and electrochemical evaluation.* Journal of The Electrochemical Society, 2010. **157**(4): p. A463-A468.

41. Franger, S., et al., *Chemistry and electrochemistry of composite LiFePO 4 materials for secondary lithium batteries.* Journal of Physics and Chemistry of Solids, 2006. **67**(5): p. 1338-1342.

42. Xu, C., J. Lee, and A.S. Teja, *Continuous hydrothermal synthesis of lithium iron phosphate particles in subcritical and supercritical water.* The Journal of Supercritical Fluids, 2008. **44**(1): p. 92-97.

43. Yuan, L.-X., et al., *Development and challenges of LiFePO 4 cathode material for lithium-ion batteries.* Energy & Environmental Science, 2011. **4**(2): p. 269-284.

44. Morgan, D., A. Van der Ven, and G. Ceder, *Li conductivity in Li x MPO 4 (M= Mn, Fe, Co, Ni) olivine materials.* Electrochemical and solid-state letters, 2004. **7**(2): p. A30-A32.

45. Park, M., et al., *A review of conduction phenomena in Li-ion batteries.* Journal of Power Sources, 2010. **195**(24): p. 7904-7929.

46. Zaghib, K., et al., *Surface effects on the physical and electrochemical properties of thin LiFePO4 particles.* Chemistry of Materials, 2007. **20**(2): p. 462-469.

47. Song, M.-K., et al., *Nanostructured electrodes for lithium-ion and lithium-air batteries: the latest developments, challenges, and perspectives.* Materials Science and Engineering: R: Reports, 2011. **72**(11): p. 203-252.

48. Guo, Y.G., J.S. Hu, and L.J. Wan, *Nanostructured materials for electrochemical energy conversion and storage devices.* Advanced Materials, 2008. **20**(15): p. 2878-2887.

49. Wang, J. and X. Sun, *Understanding and recent development of carbon coating on LiFePO 4 cathode materials for lithium-ion batteries.* Energy & Environmental Science, 2012. **5**(1): p. 5163-5185.

50. Liu, H., et al., *Effects of heteroatoms on doped LiFePO4/C composites.* Journal of Solid State Electrochemistry, 2008. **12**(7-8): p. 1017-1020.

51. Liu, H., et al., *Doping effects of zinc on LiFePO 4 cathode material for lithium ion batteries.* Electrochemistry Communications, 2006. **8**(10): p. 1553-1557.

52. Chung, S.-Y., J.T. Bloking, and Y.-M. Chiang, *Electronically conductive phospho-olivines as lithium storage electrodes.* Nature materials, 2002. **1**(2): p. 123-128.

53. Yi, T.-F., et al., *Recent developments in the doping and surface modification of LiFePO4 as cathode material for power lithium ion battery.* Ionics, 2012. **18**(6): p. 529-539.

54. Shin, H.C., W.I. Cho, and H. Jang, *Electrochemical properties of carbon-coated LiFePO 4 cathode using graphite, carbon black, and acetylene black.* Electrochimica Acta, 2006. **52**(4): p. 1472-1476.

55. Hu, L.-H., et al., *Graphene-modified LiFePO4 cathode for lithium ion battery beyond theoretical capacity.* Nature communications, 2013. **4**: p. 1687.

56. Roberts, M.R., et al., *High throughput screening of the effect of carbon coating in LiFePO4 electrodes.* Journal of the Electrochemical Society, 2007. **154**(10): p. A921-A928.

57. Doeff, M.M., et al., *Optimization of carbon coatings on LiFePO 4.* Journal of power sources, 2006. **163**(1): p. 180-184.

58. Chen, Z., et al., *Role of surface coating on cathode materials for lithium-ion batteries.* Journal of Materials Chemistry, 2010. **20**(36): p. 7606-7612.

59. Ravet, N., et al., *Electrode materials with high surface conductivity*. 2005, Google Patents.

60. Liu, Y., et al., *A novel synthesis of Fe2P–LiFePO4 composites for Li-ion batteries.* Journal of applied electrochemistry, 2010. **40**(2): p. 419-425.

61. Li, C., et al., *Cathode materials modified by surface coating for lithium ion batteries.* Electrochimica Acta, 2006. **51**(19): p. 3872-3883.

62. Wang, J., et al., *Interaction of carbon coating on LiFePO4: A local visualization study of the influence of impurity phases.* Advanced Functional Materials, 2013. **23**(7): p. 806-814.

63. Dominko, R., et al., *Impact of the carbon coating thickness on the electrochemical performance of LiFePO4/C composites.* Journal of the Electrochemical Society, 2005. **152**(3): p. A607-A610.

64. Wang, Y., et al., *Nano active materials for lithium-ion batteries.* Nanoscale, 2010. **2**(8): p. 1294-1305.

65. Ozay, O., et al., *Hydrogen production from ammonia borane via hydrogel template synthesized Cu, Ni, Co composites.* international journal of hydrogen energy, 2011. **36**(14): p. 8209-8216.

66. Wilcox, J.D., et al., *Factors influencing the quality of carbon coatings on LiFePO4.* Journal of The Electrochemical Society, 2007. **154**(5): p. A389-A395.

67. Yang, M., et al., *Synthesis and properties of optimized LiFePO4/C by a CVD-assisted two-step coating method.* Journal of nanoparticle research, 2014. **16**(9): p. 2598.

68. Wang, L., et al., *A facile method of preparing mixed conducting LiFePO 4/graphene composites for lithium-ion batteries.* Solid State Ionics, 2010. **181**(37): p. 1685-1689.

69. Gao, F., Z. Tang, and J. Xue, *Preparation and characterization of nano-particle LiFePO 4 and LiFePO 4/C by spray-drying and post-annealing method.* Electrochimica acta, 2007. **53**(4): p. 1939-1944.

70. Silan, C., et al., *Novel hydrogel particles and their IPN films as drug delivery systems with antibacterial properties.* Colloids and Surfaces B: Biointerfaces, 2012. **89**: p. 248-253.

71. Gaberscek, M., et al., *Porous, carbon-decorated LiFePO 4 prepared by sol–gel method based on citric acid.* Solid State Ionics, 2005. **176**(19): p. 1801-1805.

72. Dong, Y., et al., *Optimized carbon-coated LiFePO 4 cathode material for lithium-ion batteries.* Materials Chemistry and Physics, 2009. **115**(1): p. 245-250.

73. Zhao, B., et al., *Morphology and electrical properties of carbon coated LiFePO 4 cathode materials.* Journal of Power Sources, 2009. **189**(1): p. 462-466.

74. Wang, L., et al., *A soft chemistry synthesis routine for LiFePO 4–C using a novel carbon source.* Journal of Alloys and Compounds, 2008. **456**(1): p. 461-465.

75. Cheng, L., et al., *Low cost synthesis of LiFePO 4/C cathode materials with Fe 2 O 3.* Journal of Power Sources, 2013. **242**: p. 656-661.

76. Molenda, M., et al., *Carbon nanocoatings for C/LiFePO 4 composite cathode.* Solid State Ionics, 2013. **251**: p. 47-50.

77. Choy, K., *Chemical vapour deposition of coatings.* Progress in materials science, 2003. **48**(2): p. 57-170.

78. Vahlas, C., et al., *Principles and applications of CVD powder technology.* Materials Science and Engineering: R: Reports, 2006. **53**(1): p. 1-72.

79. Becker, A. and K. Hüttinger, *Chemistry and kinetics of chemical vapor deposition of pyrocarbon—III pyrocarbon deposition from propylene and benzene in the low temperature regime.* Carbon, 1998. **36**(3): p. 201-211.

80. Latifi, M., F. Berruti, and C. Briens, *A novel fluidized and induction heated microreactor for catalyst testing.* AIChE Journal, 2014. **60**(9): p. 3107-3122.

81. http://iitkgp.vlab.co.in.

82. Tamor, M. and W. Vassell, *Raman ''fingerprinting''of amorphous carbon films.* Journal of Applied Physics, 1994. **76**(6): p. 3823-3830.

83. Martin, J.F., et al., *Air exposure effect on LiFePO4.* Electrochemical and Solid-State Letters, 2008. **11**(1): p. A12-A16.

84. Xia, X., Z. Wang, and L. Chen, *Regeneration and characterization of air-oxidized LiFePO 4.* Electrochemistry Communications, 2008. **10**(10): p. 1442-1444.

85. Gyenes, B., et al., *Understanding anomalous behavior in coulombic efficiency measurements on Li-ion batteries.* Journal of The Electrochemical Society, 2015. **162**(3): p. A278-A283.

86. Ali, S.S. and M. Asif, *Fluidization of nano-powders: Effect of flow pulsation.* Powder technology, 2012. **225**: p. 86-92.

87. Dewettinck, K. and A. Huyghebaert, *Fluidized bed coating in food technology.* Trends in Food Science & Technology, 1999. **10**(4): p. 163-168.

88. Armand, M. and J.-M. Tarascon, *Building better batteries.* Nature, 2008. **451**(7179): p. 652-657.

89. Chen, X., et al., *Nanomaterials for renewable energy production and storage.* Chemical Society Reviews, 2012. **41**(23): p. 7909-7937.

90. van Ommen, J.R., J.M. Valverde, and R. Pfeffer, *Fluidization of nanopowders: a review.* Journal of nanoparticle research, 2012. **14**(3): p. 1-29.

91. Shabanian, J., R. Jafari, and J. Chaouki, *Fluidization of ultrafine powders.* International Review of Chemical Engineering, 2012. **4**(1): p. 16-50.

92. Geldart, D., *Types of gas fluidization.* Powder technology, 1973. **7**(5): p. 285-292.

93. Tsutsumi, A., et al., *A novel fluidized-bed coating of fine particles by rapid expansion of supercritical fluid solutions.* Powder technology, 1995. **85**(3): p. 275-278.

94. Fan, L. and C. Zhu, *Principles of Gas-Solid Flows, Cambridge Series in Chemical Engineering*. 1998, Cambridge University Press, United Kingdom.

95. Shabanian, J. and J. Chaouki, *Hydrodynamics of a gas–solid fluidized bed with thermally induced interparticle forces.* Chemical Engineering Journal, 2015. **259**: p. 135-152.

96. Hakim, L.F., J. Blackson, and A.W. Weimer, *Modification of interparticle forces for nanoparticles using atomic layer deposition.* Chemical Engineering Science, 2007. **62**(22): p. 6199-6211.

97. Yao, W., et al., *Fluidization and agglomerate structure of SiO 2 nanoparticles.* Powder Technology, 2002. **124**(1): p. 152-159.

98. Valverde, J.M. and A. Castellanos, *Effect of vibration on agglomerate particulate fluidization.* AIChE journal, 2006. **52**(5): p. 1705-1714.

99. Zhu, C., et al., *Sound assisted fluidization of nanoparticle agglomerates.* Powder Technology, 2004. **141**(1): p. 119-123.

100. Barletta, D. and M. Poletto, *Aggregation phenomena in fluidization of cohesive powders assisted by mechanical vibrations.* Powder technology, 2012. **225**: p. 93-100.

101. Madhiyanon, T., A. Phila, and S. Soponronnarit, *Models of fluidized bed drying for thin-layer chopped coconut.* Applied Thermal Engineering, 2009. **29**(14): p. 2849-2854.

102. Pfeffer, R., J.A. Quevedo, and J. Flesch, *Fluidized bed systems and methods including micro-jet flow*. 2013, Google Patents.

103. Yu, Q., et al., *Enhanced fluidization of nanoparticles in an oscillating magnetic field.* AIChE Journal, 2005. **51**(7): p. 1971-1979.

104. Matsuda, S., et al., *Modeling for size reduction of agglomerates in nanoparticle fluidization.* AIChE journal, 2004. **50**(11): p. 2763-2771.

105. Akhavan, A., et al., *Enhanced fluidization of nanoparticles with gas phase pulsation assistance.* Powder Technology, 2015. **284**: p. 521-529.

106. Köksal, M. and H. Vural, *Bubble size control in a two-dimensional fluidized bed using a moving double plate distributor.* Powder technology, 1998. **95**(3): p. 205-213.

107. Coppens, M.-O. and J. Van Ommen, *Structuring chaotic fluidized beds.* Chemical Engineering Journal, 2003. **96**(1): p. 117-124.

108. Hadi, B., J.R. van Ommen, and M.-O. Coppens, *Enhanced particle mixing in pulsed fluidized beds and the effect of internals.* Industrial & Engineering Chemistry Research, 2011. **51**(4): p. 1713-1720.

109. Xu, C. and J. Zhu, *Parametric study of fine particle fluidization under mechanical vibration.* Powder Technology, 2006. **161**(2): p. 135-144.

110. Nakamura, H. and S. Watano, *Fundamental particle fluidization behavior and handling of nano-particles in a rotating fluidized bed.* Powder Technology, 2008. **183**(3): p. 324-332.

111. Li, Z., et al., *Investigation on the drying kinetics in a pulsed fluidized bed.* Journal of chemical engineering of Japan, 2004. **37**(9): p. 1179-1182.

112. Akhavan, A., et al., *Improved drying in a pulsation-assisted fluidized bed.* Industrial & Engineering Chemistry Research, 2008. **48**(1): p. 302-309.

113. Oh, S.W., et al., *Double carbon coating of LiFePO4 as high rate electrode for rechargeable lithium batteries.* Advanced materials, 2010. **22**(43): p. 4842-4845.

114. Chen, Z. and J. Dahn, *Reducing carbon in LiFePO4/C composite electrodes to maximize specific energy, volumetric energy, and tap density.* Journal of the Electrochemical Society, 2002. **149**(9): p. A1184-A1189.

115. Gheorghiu, S., J. Van Ommen, and M.-O. Coppens, *Power-law distribution of pressure fluctuations in multiphase flow.* Physical Review E, 2003. **67**(4): p. 041305.

APPENDIX A – FLUIDZATION OF NANOPARTICLES

In recent decades, coating of nano materials due to their wide applications in reaction engineering such as in pharmaceutical, food and fertilizers industry[87], electronics, magnetism, optics, biomedical, energy resources[88, 89], ceramic and catalyst science have attracted a lot of attention. The main reason of coating particles with another ultrafine material is alteration of the surface without any affecting the bulk properties. Therefor, the nanoparticles have to be well dispersed as the first step of coating progress.

Gas-solid fluidization consists of mixing and suspending the whole particles with an upward gas stream with such a velocity that drag and gravitational forces are in equilibrium.[90] Commonly, there are two dominant forces applied to the solid bed in fluidization: (1) Hydrodynamic forces including drag force (F_D) and Buoyant weight and (2) Inter particle forces (IPF)[91]

A.1 Interparticle forces

Figure 6.1 shows the schematic diagram prepared by Seville et al. that describe the magnitude of interparticular forces for particles in size range of 1-1000 micron. The three main forces between ultrafine particles as cohesive forces are Van der Waals, capillary or liquid bridging and electrostatic forces.

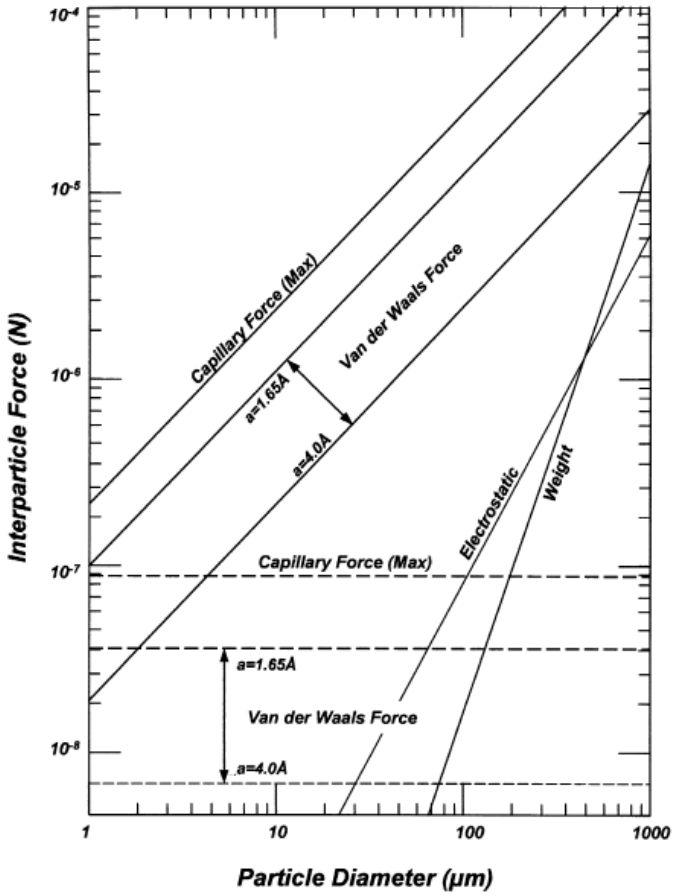

Figure 6.1: Comparison of the magnitude of inter particular forces

A.1.1. Liquid bridge force:

This force arises from the existence of moisture or any kind of liquid sourced from gas condensation adsorbed on the surface of the particles. This liquid forms a bridge between the particles and causes more attraction force that inhibit particles from movement.

$$\boldsymbol{F_l = 2\pi r^2 \gamma + \pi r^2 \Delta P} \qquad \text{Equation 1}$$

r is the particles radii, γ is the surface tension of the bridges and ΔP is the reduction in pressure within the bridge with respect to the surrounding pressure.

Sintering is another type of liquid bridging forces with a difference that the liquid formed on the particles surface by migration of the material to the region of contact to form a neck. It is a time-dependent process that size of the neck will increase with time according to the equation(6.2):

$$(\frac{x}{R})^2 = k\tau \qquad \text{Equation 2}$$

x is the radius of the neck at the time τ and k in the case of viscous sintering is derived from Frenkel equation as $k = 3\gamma/2R\mu$. Generally, the rate of the material migration is a function of temperature. In viscous sintering, migration is opposed by viscosity which is an Arrhenius function of temperature as the equation(6.3):

$$\mu = \mu_0 \exp(\frac{E}{RT}) \qquad \text{Equation 3}$$

It explains that sintering occurs faster at higher temperature and makes permanent necks between particles and causes defluidization.

A.1.2 Electrostatic force:

Charged particles in a gas-solid fluidized bed can affect the flow pattern of the bed. The electrostatic charge depends on the previous interaction with other types of material and could be described by Coulomb's law as:

$$F_e = \frac{1}{4\pi\epsilon}\frac{q_1 q_2}{s^2} \qquad \text{Equation 4}$$

Where q_1 and q_2 are charge of the particles, s is the distance between two particles and ϵ is the permittivity of the medium. The electrostatic force plays an important role between agglomerates.

A.1.3 Van der waals forces:

This term is taken to include dispersion forces arising between molecules in such fine materials. It does not consist of chemical binding between molecules such as hydrogen binding but refers to

dipole/dipole, non-polar/dipole and non-polar/non-polar forces exist in the bulk of material. The Van der Waals forces between particles with the diameter of d_p could be determined as:

$$\boldsymbol{F_{VdW} = \frac{d_p^3 A_H}{12(x + r_{asp})^2 (d_p + x + r_{asp})^2}} \quad \text{Equation 5}$$

which a is the surface separation and A_H is the Hamaker constant that determines the magnitude of Van der Waals force and has a specific amount for each material. As a result, Van der Waals force is affected by the nature of the material and its surface roughness. This equation could be simplified as:

$$\boldsymbol{F_{VdW} = \frac{d_p^3 A_H}{12x^2}} \quad \text{Equation 6}$$

in which particles are considered as spheres.

In the case of complete fluidization, due to the high rate of mass and heat transfer, good mixing and high contact of solid-solid and gas-solid, it is one of the best method of handling and processing of nano materials.

In a fluidized system, classical powders in the size range of 30-1000 micron (Group A and B) could be conventionally fluidized by the gas stream. However, for the ultra fine particles such as LFP with the particle size less than 30 micron, fluidization becomes more complex. According to Geldart's classification shown in Figure 6.1 [92], particles are divided into 4 main groups of A, B, D and C based on their size and difference in their density with fluidization medium. Particles with the size less than 30 microns (including nano-sized and cohesive particulates) belong to geldart's group C class[93].

The level of interparticular forces for particles group A, B and D is not considerable, However, the cohesive forces are dominant in group C particles fluidization. At ambient condition for dry particles, van der waals forces play the main role in most of the cases.

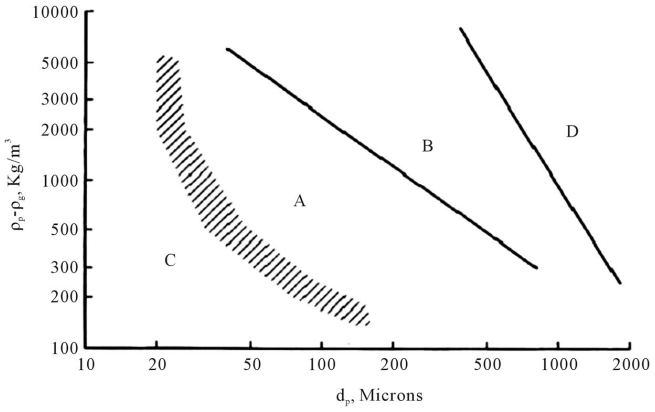

Figure 6.2: Geldart's particles classification

Due to the presence of interparticle bindings or sintering, primary particles belong to group C unite into assemblage structures (secondary particles) and the term of fluidization of these particles refers to agglomerates fluidization. Agglomerate and aggregate are two distinct terms to describe these assemblages although most of the time they are used interchangeably. The formed bound in agglomerates are not permanent and could be broken easily despite of the bounds in aggregates which are formed by solid-state neck and are stronger and need to be overcome by an extra assistant force. These agglomerate structures of primary particles combine during the fluidization and with high strength makes the bed defluidized since the gas doesn't have enough energy to overcome the cohesiveness of the agglomerates

Interparticle forces do not have any direct influence on the flow pattern in the bed, but they make some interactions between solid particles and fluid motion[94]. Plugging, channeling and agglomerating are the problems of the fluidization of group C powders that are shown in Figure 6.2 that cause difficulty for conventional aerating fluidization[95, 96].

Figure 6.3: Channeling, plugging and agglomerating

Although nano particle fluidization has a great potential for commercial production and operation, it is currently applied in limited applications due to the limitations related to the process cost and conditions.

Mostly, nano powders due to the presence of high level of interparticle forces are in forms of agglomerates. Accordingly, fluidization of these agglomerates is classified into Agglomerate particles fluidization (APF) and Agglomerate bubbling fluidization (ABF) which are introduced by Wang et al (2002)[97, 98]. Nano materials with density less than 100 kg/m3, belong to the APF classification and usually they can be fluidized with conventional fluidization. Tsutsumi et al. used a spouted fluidized bed to perform coating process of fine powders[93]. Homogenous fluidization, large bed expansion and low minimum fluidization velocity are fluidization characteristics of APF materials.

But for fine cohesive powders both in nano- and micron-size powders, which have density more than 100 kg/m^3 they belong to ABF group and there should be an external assistant power for fluidization due to their high minimum fluidization velocity[90, 91].

There are two methods to enhance group C particles fluidization; first one is to apply an assistant force to opposite dissuasive forces and the second one is to modify surface characteristics of the particles by coating or mixing with coarse particles with different shape and size.

Applying the external assistant forces helps to overcome interparticle forces by breaking cracks, channels and big agglomerates. There are several methods for assisting fluidization of particles group C. In this regard, people use sound waves[99], mechanical vibration[100]and stirring[101], micro jets[102], magnetic and centrifugal fields[103, 104] and gas pulsation[86, 105-108]. Structuring fluidized bed reactors with such assistant forces enhances conversion and selectivity of the reactor by manipulating bubble size and distribution.

Table 4 Examples of external-assisted fluidization technics

Assistant methods	**Limitations**	**Advantages**	**Schematic diagram**	**Ref.**
Mechanical vibration	Energy intensive	Decreasing minimum fluidization velocity (U_{mf})	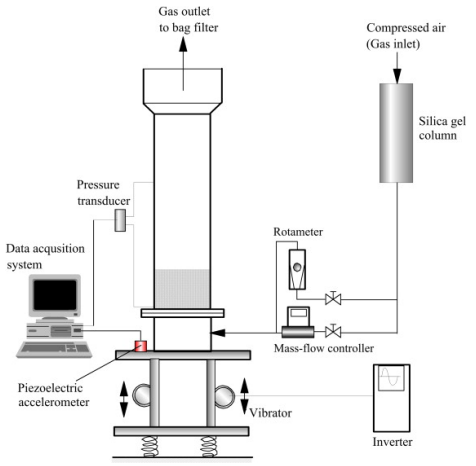	[109]
Mechanical stirring	Affects on hydrodynamic	Elimination of channeling and slugging	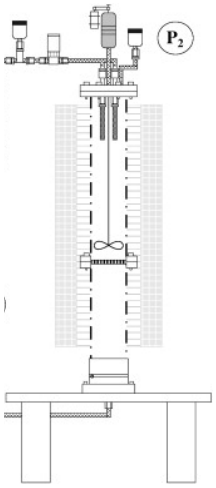	[90]

Microjets	Influence on hydrodynamic	Easy to scale-up	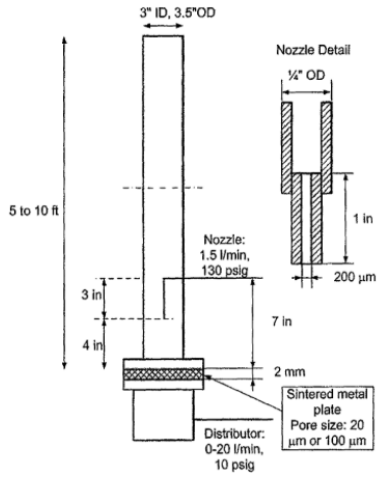	[102]
Sound wave	Energy intensive	Elimination of slugging and channeling	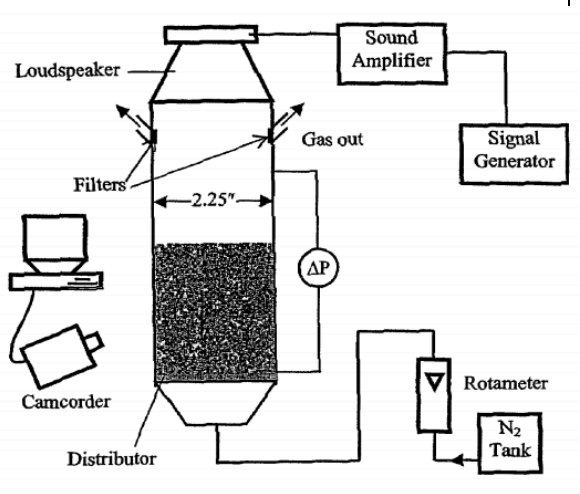	[99]
Centrifugal field	Attrition	Decreases in agglomerat size	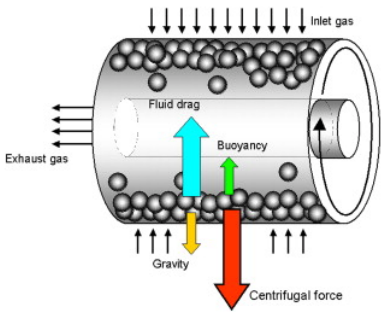	[110]

In this study, we tried to focus on fluidization of cohesive LFP powders assisted with gas pulsation. Gas pulsation includes varying periodically of the gas flow versus time. After the particles were sieved and put inside the reactor, although the particles were in the size range of

125-250 micron, they did not become fluidized. Initially, we test the fluidization quality in a transparent tube. Expectedly, LFP particles didn't become fluidized with the defined gas flow. The idea of gas-pulsation came from an initial test of gas stream existence through the bed by put/take up a finger at the outlet of the reactor. Thus, gas was pressurized inside the reactor and when it let to release, a considerable jumping movement of the solid bed was observed. By repeating the put/take up act, the bed fully mixed. As a result, we tried to make such a gas pulsation with controlled frequency by installing a solenoid valve in the outlet of the reactor.

Since this method is going to be used for process at high temperature for LFP particles, it was concerned that the hot gas damages the valve. We changed the position of the valve to the inlet of the reactor to make gas pulsation. The schematic between two valve position is shown in Figure 6.3 as could be observed, when the valve is located in the outlet, jets damped during on-time of the valve and pressurized gas behind the distributer forms bigger and stronger jets compare to the situation that valve is located before the distributer. Damping effect of the distributer on the gas will be discussed in the next section.

There are several other methods to generate the gas pulsation. The most common and simplest method is to use solenoid valves in the inlet of the reactor[105, 107]. Li et al. used butterfly valve and some other people used rotating or moving distributers to make pulsation[106, 108, 111]. The advantage of using gas pulsation compared to the other assistant technics is that there is no excess body added to the bed to influence the hydrodynamic like using micro jets. Pulsing could be applied to any constructed setup that already contains heat exchanger. We applied it to the systems that we have used them and it is a good economical benefit, so there is no need to change the configuration of the reactor to other types such as rotary reactors. Also, it is applicable to use in large scale however in some technics such as sound waves or vibration is not possible to scale up.

Two pathways to apply gas pulsing flow to the reactor are introduced in the literature; To the best of our knowledge, pulse fluidization has been studied in drying process of the wet particles in presence of liquid bridge forces. Hadi and Akhavan et al, used two flows of the gas; one primary constant flow and one secondary pulsing flow. Introducing the primary flow to the bed is to inhibit defluidization and decrease the bubble diameter, while the secondary pulsing flow is employed to enhance the quality of fluidization[108, 112].

The main purpose of this study is to apply this method of fluidization for olivine carbon coating via CVD process with respect to the hydrodynamic studies of fluidized bed.

Chemical vapor deposition (CVD), is defines as a process of decomposition and/ or chemical reaction of a gaseous reactants in an activated medium such as high temperature or plasma environment[77].

The most effective way of depositing carbon to these materials is pyrolysing gas, liquid- or solid phase precursors on the surface of the particles[23, 113, 114]. This can be performed during or after synthesis of materials. For instance, the carbon source such as a polymer or hydrocarbon is added the sample and they will be heated up to the elevated temperature to carbonize the coated material and eventually a thin layer of carbon will be deposited on the particles.

In the present investigation, we tried to overcome inter particular forces between fine particles at ambient conditions. We used pressure measurements to characterize the dynamic of the fluidization. Pressure measurement is a robust and inexpensive technic to validate fluidization regimes and bubble size. Bubble coalescence/breakup, bubble formation at the distributer and eruption at the surface of the bed, these are properties of the fluidization hydrodynamic which could be analyzed by the pressure fluctuations[115]. Also during chemical vapor deposition process at elevated temperature in fluidized bed reactor with assistance of gas pulsation. The quality of fluidization is discussed in terms of pressure drop and power spectral density analysis across the bed.